

# Impact of mass transfer on the orbital evolution of a white dwarf close to an intermediate-mass black hole

Yang Yang,<sup>1,2\*</sup> Jie Yang,<sup>3,4,5,6†</sup> Xian Chen,<sup>1,2‡</sup> and Zihan Zhang<sup>7,8§</sup>

<sup>1</sup>*Astronomy Department, School of Physics, Peking University, 100871 Beijing, China*

<sup>2</sup>*Kavli Institute for Astronomy and Astrophysics, Peking University, 100871 Beijing, China*

<sup>3</sup>*School of Physical Science and Technology, Lanzhou University, Lanzhou 730000, China*

<sup>4</sup>*Institute of Theoretical Physics & Research Center of Gravitation, Lanzhou University, Lanzhou 730000, China*

<sup>5</sup>*Key Laboratory of Quantum Theory and Applications of MoE, Lanzhou University, Lanzhou 730000, China*

<sup>6</sup>*Lanzhou Center for Theoretical Physics & Key Laboratory of Theoretical Physics of Gansu Province, Lanzhou University, Lanzhou 730000, China*

<sup>7</sup>*International Centre for Theoretical Physics Asia-Pacific, University of Chinese Academy of Sciences, 100190 Beijing, China*

<sup>8</sup>*Taiji Laboratory for Gravitational Wave Universe, University of Chinese Academy of Sciences, 100049 Beijing, China*

Accepted XXX. Received YYY; in original form ZZZ

## ABSTRACT

Extreme mass ratio inspiral (EMRI) systems composed of low-mass white dwarfs (WDs,  $0.1 - 0.3 M_{\odot}$ ) and intermediate-mass black holes (IMBHs,  $10^3 - 10^5 M_{\odot}$ ) are ideal objects for multi-messenger astronomy because they produce both gravitational wave (GW) and electromagnetic (EM) signals. Both relativistic effects and the mass transfer (MT) process are important for determining orbital dynamics, but the current model has not taken these ingredients fully into account. Here we use a perturbed Keplerian framework and the post-Newtonian (PN) formalism to model the relativistic orbit of a WD around a spinning IMBH. We pay special attention to the dynamical evolution during a narrow phase near the orbital pericenter where the WD fills the Roche lobe and starts MT. We find that gravitational radiation and MT have opposing effects on orbital evolution. When MT predominates, the orbital period and eccentricity could increase, sometimes enabling the WD to escape and avoid tidal disruption. Additionally, we estimate the time required for the GW phase to shift by one radian due to the MT process and identify cases where this phase shift will be detectable by future GW observations. The temporal expansion of the orbit during MT offers a potential explanation for the disappearance of quasi-periodic eruptions (QPEs) found in several X-ray transients, highlighting the importance of including both the relativistic and MT processes in the WD-IMBH model.

**Key words:** black hole physics – galaxies: active – X-rays: galaxies – gravitational waves

## 1 INTRODUCTION

An extreme-mass-ratio inspiral (EMRI) involves a massive black hole (MBH) and a compact object (CO), such as a white dwarf (WD), neutron star (NS), or stellar-mass black hole (BH), moving along a tightly bound orbit around the MBH (Hills & Bender 1995; Amaro-Seoane et al. 2007). EMRIs are important sources for future space-based gravitational wave (GW) detectors, such as the Laser Interferometer Space Antenna (LISA) (Barack & Cutler 2004; Gair 2009; Berry & Gair 2012; Gair et al. 2017; Amaro-Seoane et al. 2017). Their GW signals contain rich information about the formation and evolution of stars around MBHs (Amaro-Seoane et al. 2007; Amaro-Seoane 2018), and they also offer a unique opportunity to test general relativity in the strong-gravity regime (Barsanti et al. 2024; Speri 2024).

Among the various types of EMRIs, WDs inspiraling towards intermediate-mass black holes (IMBHs,  $10^3 - 10^5 M_{\odot}$ ) stand out as

a special type, not only because their formation channel was recognized relatively early (Hills & Bender 1995; Freitag 2001; Bogdanović et al. 2014), but also because the end products are luminous electromagnetic (EM) flares from the tidal disruption of the WDs by the IMBHs (Luminet & Pichon 1989; Ivanov, P. B. & Papaloizou, J. C. B. 2007; Zalamea et al. 2010). Such EM counterparts associated with GW signals could enable precise measurements of the geometry of the universe (Menou et al. 2008; Sesana et al. 2008).

King (2020) suggested that quasi-periodic eruptions (QPEs), a type of X-ray transient recently discovered (e.g. Miniutti et al. 2019; Giustini, Margherita et al. 2020; Arcodia et al. 2021; Chakraborty et al. 2021; Arcodia, R. et al. 2022; Miniutti, G. et al. 2023a,b; Arcodia, R. et al. 2024; Giustini, Margherita et al. 2024), are produced by WD-IMBH systems. Alternative models, such as star-disk collisions, also exist (Xian et al. 2021; Franchini, Alessia et al. 2023; Zhou et al. 2024a,c; Chakraborty et al. 2024). The sharpness of each burst and the average time between consecutive eruptions are well explained by the repeated partial disruption of the smaller compact object (or a main-sequence star) by the IMBH (King 2022; Chen et al. 2022; Zhao, Z. Y. et al. 2022; Krolik & Linial 2022; Wang et al. 2022; Lu & Quataert 2023; Linial & Sari 2023; Garain & Sarkar 2024).

However, not all the observational properties of QPEs have been

\* E-mail: yangyang24@stu.pku.edu.cn

† E-mail: yangjiev@lzu.edu.cn

‡ E-mail: xian.chen@pku.edu.cn

§ E-mail: zhangzihan242@mails.ucas.ac.cn

explained by the WD-IMBH interaction. First, in several QPEs, the time between consecutive eruptions alternates between long and short durations (Miniutti et al. 2019). While it has been suggested that this "long-short behavior" may result from variations in the amount of mass stripped from the WD (King 2022), a detailed model is still lacking. Second, in the case of GSN 069, QPEs disappeared for about two years before reappearing (Miniutti, G. et al. 2023b,a). This behavior is not predicted by the WD-IMBH model either. In contrast, the star-disk collision model has been developed to the point where it can successfully fit the light curves of QPEs (e.g. Franchini, Alessia et al. 2023; Zhou et al. 2024b; Miniutti, G. et al. 2025).

Several key physical processes are missing in the current WD-IMBH model, which hinders a direct comparison of the model predictions with the observed QPE light curves. (i) The effects of general relativity have not been fully accounted for. What has been included in the model (e.g. Zalamea et al. 2010; King 2020) is the secular decay of the orbital semimajor axis and eccentricity due to GW radiation, but the derivation of the formulae is based on the Keplerian orbit approximation (Peters 1964). Such a model fails to capture the relativistic precession of the orbital pericenter or the variation in the orientation of the orbital angular momentum due to frame dragging if the central IMBH is spinning. These effects could introduce new characteristic frequencies into the orbit of the WD, as well as change our viewing angle of the system. Hence, they may be important for explaining the occurrence times or luminosities of the eruptions. The relevance of these effects is corroborated by the high orbital eccentricities (i.e., small pericenter distances) inferred for the WD orbits in QPEs (Chen et al. 2022; King 2022, 2023). (ii) Mass transfer (MT) from the WD to the IMBH is inevitable and is suspected to be responsible for stabilizing the long-term evolution of the binary (King 2022). However, the detailed mechanism remains unclear. One recent study (Wang et al. 2022) attempts to use the orbital-averaged dynamical equations derived for stellar binaries (Sepinsky et al. 2007b) to model the secular evolution of a WD-IMBH binary. However, since MT in the WD-IMBH scenario occurs mainly at pericenter due to the aforementioned high eccentricity, the validity of the orbital average remains unverified.

This work is motivated by the incompleteness of the current WD-IMBH model and aims to improve the treatment of relativistic effects and the MT process. To resolve the relativistic effects during each orbital period, we will use the post-Newtonian (PN) method and the perturbed Kepler method. The PN method extends Newtonian gravity to include relativistic corrections, providing additional acceleration terms that can be incorporated into classical mechanics. In two-body motion, relativistic accelerations result in changes to orbital parameters defined by Newtonian gravity, such as the semi-major axis, eccentricity, and phase angle. These variations are efficiently modeled using the perturbed Kepler method, which yields differential equations governing orbital evolution. The form of these equations provides a mathematical framework for addressing MT acceleration. Regarding the MT process and its dynamical consequences, we focus on MT during short time intervals centered around orbital pericenter. WDs fill the Roche lobe and overflow only within a narrow phase range near pericenter in high-eccentricity orbits. In orbital dynamics, it is effective to treat the MT rate of the WD as a function sharply peaked around pericenter, resembling a delta function (Sepinsky et al. 2007b). The MT rate expression can be expanded in terms of the difference between the Roche radius and the radius of the WD.

This paper is organized as follows. In Section 2, using the perturbed Kepler method (Efroimsky 2005; Poisson & Will 2014), we describe the motion of the WD in the IMBH's relative coordinate system. We assume that all acceleration terms can be expressed in terms

of the required parameters. In Section 3, we present the WD state formulae (Zalamea et al. 2010), the MT model (Kolb & Ritter 1990; Sepinsky et al. 2007a; Cehula & Pejcha 2023a), and the dynamics of eccentric binaries under MT (Sepinsky et al. 2007b). In Section 4, we introduce the initial angle parameter representation for the case where the spin angular momentum of the IMBH is aligned with the Z-axis, and numerically compute the short-term orbital evolution using the PN method and the perturbed Kepler method, both with and without MT. In Section 5, we analyze the combined effects of MT and gravitational radiation on the long-term orbital evolution, using the time-averaged rate of change over one period. We describe the orbital evolution starting from the point where the Roche lobe radius at pericenter equals the WD radius. In Section 6, for the GW signal, we compute the time required for the orbital phase to change by 1 radian due to the MT effect, and identify the initial parameters that enable the detection of phase differences within 5 years. In Section 7 and 8, we discuss and summarize our results.

## 2 POST-NEWTONIAN DYNAMICS

### 2.1 Relative acceleration in general relativity

The relativistic dynamics of point particles can be described by a variation of the geodesic equation, following Blanchet et al. (1998); Blanchet (2014, 2024). The equation of motion is

$$\frac{d\mathcal{P}_{iA}}{dt} = \mathcal{F}_{iA}, \quad (1)$$

where  $\mathcal{P}_{iA}$  and  $\mathcal{F}_{iA}$  are

$$\mathcal{P}_{iA} = c \left( \frac{g_{i\mu} v^\mu}{\sqrt{-g_{\alpha\beta} v^\alpha v^\beta}} \right)_A, \quad \mathcal{F}_{iA} = \frac{c}{2} \left( \frac{v^\mu v^\nu \partial_i g_{\mu\nu}}{\sqrt{-g_{\alpha\beta} v^\alpha v^\beta}} \right)_A. \quad (2)$$

In these expressions, the Latin indices  $i, j, k$  denote the spatial components 1, 2, 3. The quantity  $\mathcal{P}_i$  represents the linear momentum density, while  $\mathcal{F}_i$  corresponds to the force density. The PN metric  $g_{\mu\nu}$  follows the PN expansion from the Landau–Lifshitz formulation of the field equations (Landau 2013), which involves the spatial integration of the energy-momentum tensor  $T_{\mu\nu}$ . By substituting the Dirac delta function form of  $T_{\mu\nu}$  for point particles into this integration and applying regularization methods, explicit expressions for the PN metric  $g_{\mu\nu}$  are obtained (Blanchet 2014, 2024). The particle's coordinate velocity is  $v^\mu = dx^\mu/dt = (c, v^i)$ , where  $x^\mu := (ct, x^i)$ , and  $v^i$  denotes the spatial velocity components. Additionally, in Equations (1) and (2), the subscript A denotes quantities evaluated at the spacetime point of particle A. In Equation (2),  $(g_{\mu\nu})_A$  represents the PN metric at this point, and  $(v^\mu)_A$  is the corresponding coordinate velocity of particle A.

To determine the individual positions of the particles in the center-of-mass frame, we impose the condition that the mass dipole moment, i.e.  $I_i = 0$ . For a binary system, the individual positions are given by (Blanchet 2014, 2024):

$$\begin{aligned} \mathbf{y}_1 &= \mathbf{r}_{\text{cm}} + \frac{m_2}{m} \mathbf{r} + \eta \Delta [\mathcal{P} \mathbf{r} + \mathcal{Q} \mathbf{v}] + O(c^{-7}), \\ \mathbf{y}_2 &= \mathbf{r}_{\text{cm}} - \frac{m_1}{m} \mathbf{r} + \eta \Delta [\mathcal{P} \mathbf{r} + \mathcal{Q} \mathbf{v}] + O(c^{-7}), \end{aligned} \quad (3)$$

where  $\mathbf{r}_{\text{cm}}$  denotes the position of the center-of-mass relative to an arbitrary coordinate system, and  $\mathbf{y}_A - \mathbf{r}_{\text{cm}}$  represents the position of particle A in the center-of-mass frame. The relative position between the two particles is  $\mathbf{r} = \mathbf{y}_1 - \mathbf{y}_2$ , the relative velocity is  $\mathbf{v} = d\mathbf{r}/dt$ . And the total mass is  $m = m_1 + m_2$ , the symmetric mass ratio is

$\eta = m_1 m_2 / m^2$ , and the mass difference ratio is  $\Delta = (m_1 - m_2) / m$ . The functions  $\mathcal{P}(\mathbf{r}, \mathbf{v})$  and  $\mathcal{Q}(\mathbf{r}, \mathbf{v})$  are the coefficients.

The relative acceleration  $\mathbf{a}(\mathbf{r}, \mathbf{v}) = \dot{\mathbf{v}}_1 - \dot{\mathbf{v}}_2$  can be directly calculated from  $\mathbf{a}_A(\mathbf{r}_A, \mathbf{v}_A, \mathbf{r}_B, \mathbf{v}_B)$  in Equation (1) and  $\mathbf{a}_A(\mathbf{a}_{\text{cm}}, \mathbf{r}, \mathbf{v}, \mathbf{a}, \dot{\mathbf{a}})$  from the second time derivative of Equation (3). The dots above the variables denote time derivatives.

Furthermore, first, for the case where the particle A has spin angular momentum  $\mathbf{S}_A$ , Tagoshi et al. (2001) provides the necessary expressions to compute the trajectory: The relative acceleration  $\mathbf{a}$  includes contributions of the spin-orbit term  $\mathbf{a}_{\text{SO}}$ , the spin-spin term  $\mathbf{a}_{\text{SS}}$ , and the spin-orbit PN term  $\mathbf{a}_{\text{SOPN}}$ , as given in their Equation (5.15); the spin precession equation,  $d\mathbf{S}_A/dt$ , is given in their Equation (2.17); the individual positions in the center-of-mass frame, analogous to Equation (3), is given in their Equation (5.13). Second, the additional acceleration term  $\mathbf{f}_{\text{MT}}$  due to the MT process is provided in Equation (14) of Sepinsky et al. (2007b). We will give the further details of  $\mathbf{f}_{\text{MT}}$  in Section 3.3.

Therefore, for a spinning binary system with the MT process, the equation of motion in relative acceleration form is

$$\mathbf{a} = -\frac{Gm}{r^2} [(1 + \mathcal{A})\mathbf{n} + \mathcal{B}\mathbf{v}] + \mathbf{a}_{\text{SO}} + \mathbf{a}_{\text{SS}} + \mathbf{a}_{\text{SOPN}} + \mathbf{f}_{\text{MT}} + \mathcal{O}(c^{-8}), \quad (4)$$

where  $r = |\mathbf{r}|$ ,  $\mathbf{n} = \mathbf{r}/r$ , and  $\mathcal{A}, \mathcal{B}$  are functions of  $\mathbf{r}$  and  $\mathbf{v}$  (Blanchet 2014). The terms  $\mathbf{a}_{\text{SO}}, \mathbf{a}_{\text{SS}}, \mathbf{a}_{\text{SOPN}}$  depend on  $(\mathbf{r}, \mathbf{v}, \mathbf{S}_1, \mathbf{S}_2)$  (Tagoshi et al. 2001), while  $\mathbf{f}_{\text{MT}}$  depends on  $(\mathbf{r}, \mathbf{v}, \dot{m}_1, \dot{m}_2)$  (Sepinsky et al. 2007b).

Equation (4) can be rearranged into

$$\mathbf{a} = \frac{d\mathbf{v}}{dt} = -\frac{Gm}{r^2}\mathbf{n} + \mathbf{f}, \quad (5)$$

where  $\mathbf{f}$  represents the relative acceleration due to perturbation, which can be written in the form of components:

$$\mathbf{f} = \mathcal{R}\mathbf{n} + \mathcal{S}\boldsymbol{\lambda} + \mathcal{W}\boldsymbol{\ell}. \quad (6)$$

Here,  $\mathbf{n}, \boldsymbol{\lambda}, \boldsymbol{\ell}$  are the basis vectors defined by the natural coordinate system. The basis vectors can be expressed in terms of  $\mathbf{r}, \mathbf{v}$  as follows:

$$\mathbf{n} = \frac{\mathbf{r}}{r}, \quad \boldsymbol{\ell} = \frac{\mathbf{n} \times \mathbf{v}}{|\mathbf{n} \times \mathbf{v}|}, \quad \boldsymbol{\lambda} = \boldsymbol{\ell} \times \mathbf{n}. \quad (7)$$

In addition, the spin change rate  $d\mathbf{S}_A/dt$  and the MT rate  $\dot{m}_1$  are essential for determining the time evolution of  $(\mathbf{S}_1, \mathbf{S}_2, m_1, m_2)$ . The  $d\mathbf{S}_A/dt$  can be expressed as (Tagoshi et al. 2001)

$$\frac{d\mathbf{S}_1}{dt} = \boldsymbol{\Omega}_1 \times \mathbf{S}_1 + \mathcal{O}(c^{-3}), \quad \frac{d\mathbf{S}_2}{dt} = \boldsymbol{\Omega}_2 \times \mathbf{S}_2 + \mathcal{O}(c^{-3}), \quad (8)$$

where  $\boldsymbol{\Omega}_1$  and  $\boldsymbol{\Omega}_2$  denote the rates at which the spin angular momentum rotates around the total angular momentum. We will derive  $\dot{m}_1$  in Section 3.

## 2.2 Classical Kepler orbit in relative coordinate

To describe the relative motion, we establish a general coordinate system in Figure 1, using the angular parameters  $(f, \omega, \Omega, \iota)$  (Poisson & Will 2014). The relative position  $\mathbf{r}$  can be described as  $\mathbf{r} = r\mathbf{n} = r^X \mathbf{e}_X + r^Y \mathbf{e}_Y + r^Z \mathbf{e}_Z$ . Here,  $\mathbf{e}_X, \mathbf{e}_Y, \mathbf{e}_Z$  are the fixed basis vectors of the Cartesian coordinate system, satisfying  $\dot{\mathbf{e}}_X = \dot{\mathbf{e}}_Y = \dot{\mathbf{e}}_Z = 0$ . Therefore,  $\mathbf{n}, \boldsymbol{\lambda}, \boldsymbol{\ell}$  can be expressed in terms of

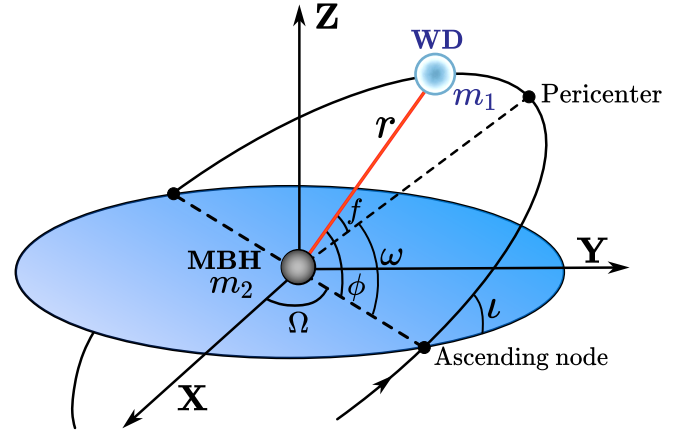


**Figure 1.** Definition of the relative coordinate and the angle parameters. The origin of the relative coordinate system is placed at mass  $m_2$ , while mass  $m_1$  follows an orbit defined by  $\mathbf{r} = r^X \mathbf{e}_X + r^Y \mathbf{e}_Y + r^Z \mathbf{e}_Z$ . For a quasi-Keplerian orbit, the system has pericenter and an ascending node, where the ascending node is the point of intersection of the orbit with the  $OXY$  plane. The parameters are as follows:  $\iota$  is the inclination of the orbital plane relative to the  $OXY$  plane;  $\Omega$  is the longitude of the ascending node, the angle between the ascending node and the positive  $X$ -axis;  $\omega$  is the argument of pericenter, the angle between the ascending node and the pericenter;  $f$  is the phase angle of  $m_1$  relative to the pericenter. The angle  $\phi$  is defined as  $\phi = \omega + f$ . The basis vectors  $\mathbf{e}_X, \mathbf{e}_Y, \mathbf{e}_Z$  define the Cartesian coordinate system with coordinates  $(X, Y, Z)$ .

$\mathbf{e}_X, \mathbf{e}_Y, \mathbf{e}_Z$  as column vectors :

$$\mathbf{n} = \begin{bmatrix} \cos \Omega \cos \phi - \cos \iota \sin \Omega \sin \phi \\ \sin \Omega \cos \phi + \cos \iota \cos \Omega \sin \phi \\ \sin \iota \sin \phi \end{bmatrix} = \frac{1}{r} \begin{bmatrix} r^X \\ r^Y \\ r^Z \end{bmatrix}, \quad (9)$$

$$\boldsymbol{\lambda} = \begin{bmatrix} -\cos \Omega \sin \phi - \cos \iota \sin \Omega \cos \phi \\ -\sin \Omega \sin \phi + \cos \iota \cos \Omega \cos \phi \\ \sin \iota \cos \phi \end{bmatrix}, \quad \boldsymbol{\ell} = \begin{bmatrix} \sin \iota \sin \Omega \\ -\sin \iota \cos \Omega \\ \cos \iota \end{bmatrix}.$$

For the classical Kepler orbit, i.e.  $\mathbf{f} = \mathbf{0}$ , the whole orbit lies in a fixed plane, without precession effect, i.e.  $\dot{\Omega} = \dot{\iota} = \dot{\omega} = 0$ , and  $\dot{\phi} = \dot{f}$ . Then, we have the equations of motion:

$$r = \frac{p}{1 + e \cos(\phi - \omega)}, \quad \dot{r} = \sqrt{\frac{Gm}{p}} e \sin(\phi - \omega),$$

$$\dot{\phi} = \sqrt{\frac{Gm}{p^3}} (1 + e \cos(\phi - \omega))^2, \quad (10)$$

$$v^2 = \frac{Gm}{p} \left[ (1 + e \cos(\phi - \omega))^2 + e^2 \sin^2(\phi - \omega) \right],$$

where  $p$  is the semi-latus rectum and  $e$  is the eccentricity.

Therefore, for  $\mathbf{f} = \mathbf{0}$ , the relative vectors  $\mathbf{r}, \mathbf{v}, \mathbf{a}$  are expressed as

$$\mathbf{r} = r\mathbf{n}, \quad \mathbf{v} = \dot{r}\mathbf{n} + r\dot{\phi}\boldsymbol{\lambda}, \quad \mathbf{a} = (\ddot{r} - r\dot{\phi}^2)\mathbf{n} + (r\ddot{\phi} + 2\dot{r}\dot{\phi})\boldsymbol{\lambda}. \quad (11)$$

We can then express  $(r^X, r^Y, r^Z), (v^X, v^Y, v^Z)$ , and  $(a^X, a^Y, a^Z)$  in terms of the parameters  $(p, e, f, \omega, \Omega, \iota)$ , which describe the trajectories of relative motion.

In a Kepler orbit under Newtonian gravity, the orbital energy, angular momentum, and the parameters  $(p, e, \omega, \Omega, \iota)$  are conserved. The motion follows these fixed parameters, i.e.

$$\frac{d\mathbf{r}_{\text{Kepler}}}{dt} = \mathbf{v}_{\text{Kepler}}, \quad \frac{d\mathbf{v}_{\text{Kepler}}}{dt} = -Gm \frac{\mathbf{r}_{\text{Kepler}}}{r_{\text{Kepler}}^3}, \quad (12)$$

where the subscript ‘‘Kepler’’ indicates the form in Equation (10).

### 2.3 Perturbed Kepler method

Assuming a non-zero perturbation acceleration,  $\mathbf{f} \neq \mathbf{0}$ , we propose that the Keplerian form in Equation (10) remains valid, but the orbital parameters  $p, e, f, \omega, \Omega, \iota$  evolve with time. The relative position vector  $\mathbf{r}$  and velocity vector  $\mathbf{v}$  can then be expressed as

$$\mathbf{r}(t) = \mathbf{r}_{\text{Kepler}}(f(t), \mu^a(t)), \quad \mathbf{v}(t) = \mathbf{v}_{\text{Kepler}}(f(t), \mu^a(t)), \quad (13)$$

where  $\mu^a = (p, e, \omega, \Omega, \iota)$  represents the orbital parameters, with the superscript  $a$  denoting different parameters. A single vector of  $\mu^a$  in parameter space corresponds to a specific Keplerian orbit. Moreover,  $(f, p, e, \omega, \Omega, \iota)$  forms a vector in real phase space, describing the position and velocity of a particle in the relative coordinate system at a given time. For details on gauge freedom in phase space in orbital mechanics, see [Efroimsky \(2005\)](#). In the perturbed Kepler method,  $\dot{\mu}^a(\mathcal{R}, \mathcal{S}, \mathcal{W}) \neq 0$ .

The derivation of  $\dot{f}(\mathcal{R}, \mathcal{S}, \mathcal{W})$  and  $\dot{\mu}^a(\mathcal{R}, \mathcal{S}, \mathcal{W})$  are given in Appendix A. The equations for  $\dot{f}$  and  $\dot{\mu}^a$  are :

$$\frac{dp}{dt} = \sqrt{\frac{p}{Gm}} p \frac{2}{1 + e \cos f} \mathcal{S}, \quad (14a)$$

$$\frac{de}{dt} = \sqrt{\frac{p}{Gm}} \left[ \sin f \mathcal{R} + \frac{2 \cos f + e(1 + \cos^2 f)}{1 + e \cos f} \mathcal{S} \right], \quad (14b)$$

$$\begin{aligned} \frac{df}{dt} &= \sqrt{\frac{Gm}{p^3}} (1 + e \cos f)^2 \\ &+ \sqrt{\frac{p}{Gm}} \frac{1}{e} \left[ \cos f \mathcal{R} - \frac{2 + e \cos f}{1 + e \cos f} \sin f \mathcal{S} \right], \end{aligned} \quad (14c)$$

$$\begin{aligned} \frac{d\omega}{dt} &= \sqrt{\frac{p}{Gm}} \frac{1}{e} \left[ -\cos f \mathcal{R} + \frac{2 + e \cos f}{1 + e \cos f} \sin f \mathcal{S} \right. \\ &\quad \left. - \cot \iota \frac{e \sin(\omega + f)}{1 + e \cos f} \mathcal{W} \right], \end{aligned} \quad (14d)$$

$$\frac{d\Omega}{dt} = \sqrt{\frac{p}{Gm}} \frac{\sin(\omega + f)}{1 + e \cos f} \csc \iota \mathcal{W}, \quad (14e)$$

$$\frac{d\iota}{dt} = \sqrt{\frac{p}{Gm}} \frac{\cos(\omega + f)}{1 + e \cos f} \mathcal{W}. \quad (14f)$$

For the changes of base vectors  $\mathbf{n}, \boldsymbol{\lambda}, \boldsymbol{\ell}$ , we can obtain the following equations in Appendix A:

$$\frac{d\mathbf{n}}{dt} = \sqrt{\frac{Gm}{p^3}} (1 + e \cos f)^2 \boldsymbol{\lambda}, \quad (15a)$$

$$\frac{d\boldsymbol{\lambda}}{dt} = \sqrt{\frac{p}{Gm}} \frac{\mathcal{W}}{1 + e \cos f} \boldsymbol{\ell} - \sqrt{\frac{Gm}{p^3}} (1 + e \cos f)^2 \mathbf{n}, \quad (15b)$$

$$\frac{d\boldsymbol{\ell}}{dt} = -\sqrt{\frac{p}{Gm}} \frac{\mathcal{W}}{1 + e \cos f} \boldsymbol{\lambda}. \quad (15c)$$

Thus, we can directly derive the new expressions for the vector  $\mathbf{r} = r\mathbf{n}$ , and its time derivatives  $\mathbf{v}$  and  $\mathbf{a}$ , when  $\mathbf{f} \neq \mathbf{0}$ :

$$\mathbf{r} = r\mathbf{n}, \quad \mathbf{v} = \dot{r}\mathbf{n} + r\dot{\mathbf{n}}, \quad (16)$$

$$\mathbf{a} = (\ddot{r} - r\dot{\mathbf{n}}^2)\mathbf{n} + (r\ddot{\mathbf{n}} + 2\dot{r}\dot{\mathbf{n}})\boldsymbol{\lambda} + r\dot{\mathbf{n}}^2\mathcal{W}_f\boldsymbol{\ell},$$

where

$$\dot{\mathbf{n}} := \sqrt{\frac{Gm}{p^3}} (1 + e \cos f)^2, \quad \mathcal{W}_f := \frac{p^2 \mathcal{W}}{Gm(1 + e \cos f)^3}. \quad (17)$$

Here,  $\dot{\mathbf{n}}$  has the same form as  $\dot{\phi}$  in Equation (10). The dimensionless quantity  $\mathcal{W}_f$  simplifies the equations when  $\mathcal{W} \neq 0$ . The expressions

for  $\mathbf{r}$  and  $\mathbf{v}$  in Equation (16) are identical to those in Equation (11), except that  $\mathbf{a}$  includes an additional term involving  $\mathcal{W}$ , which get from  $d\boldsymbol{\lambda}/dt$  in Equation (15). Equation (16) is essential for calculating the orbital trajectory with perturbation acceleration  $\mathbf{f}$  when  $\mathcal{W} \neq 0$ .

The spin angular momentum  $\mathbf{S}_A$  can be expressed as  $S_{An}\mathbf{n} + S_{A\lambda}\boldsymbol{\lambda} + S_{A\ell}\boldsymbol{\ell}$ . Substituting  $(\dot{\mathbf{n}}, \dot{\boldsymbol{\lambda}}, \dot{\boldsymbol{\ell}})$  in Equation (15) into Equation (8), we obtain the differential equations for the spin components  $S_{An}, S_{A\lambda}$ , and  $S_{A\ell}$ :

$$\frac{dS_{An}}{dt} = (\boldsymbol{\Omega}_A \times \mathbf{S}_A)_n + \dot{\mathbf{n}}_N S_{A\lambda}, \quad (18a)$$

$$\frac{dS_{A\lambda}}{dt} = (\boldsymbol{\Omega}_A \times \mathbf{S}_A)_\lambda - \dot{\mathbf{n}}_N S_{An} + \dot{\mathbf{n}}_N \mathcal{W}_f S_{A\ell}, \quad (18b)$$

$$\frac{dS_{A\ell}}{dt} = (\boldsymbol{\Omega}_A \times \mathbf{S}_A)_\ell - \dot{\mathbf{n}}_N \mathcal{W}_f S_{A\lambda}. \quad (18c)$$

Therefore, a comprehensive set of differential equations governing the dynamics of the inspiralling binary system with the MT process can be derived. This includes the following variables:

$$\{\dot{r}, \dot{\phi}, \dot{p}, \dot{e}, \dot{\omega}, \dot{\Omega}, \dot{\iota}, \dot{S}_{1n}, \dot{S}_{1\lambda}, \dot{S}_{1\ell}, \dot{S}_{2n}, \dot{S}_{2\lambda}, \dot{S}_{2\ell}, \dot{m}_1, \dot{m}_2\}.$$

### 3 MASS TRANSFER FOR ECCENTRIC BIARY

For the mass stripping of WD, we adopt the WD model in Section 3.1 ([Zalamea et al. 2010](#)), and give the MT rate  $\dot{m}_1$  in Section 3.2 ([Kolb & Ritter 1990](#)). To calculate the perturbation of orbital variables caused by MT, we use the additional acceleration  $\mathbf{f}_{\text{MT}}$  derived in Section 3.3 ([Sepinsky et al. 2007b](#)).

#### 3.1 Hydrostatic equilibrium model of white dwarf

In the follow, we assume that the polytropic equation of state (EOS) for the surface layer of the WD is  $P = K\rho^\Gamma$  ([Zalamea et al. 2010](#)), where  $\Gamma = 5/3$  and  $K \equiv (3/\pi)^{2/3} h^2 / 20m_e (\mu_e m_p)^{5/3}$ . Here,  $h$  is the Planck constant,  $m_e$  is the electron mass,  $m_p$  is the proton mass, and  $\mu_e \approx 2$  is the mean molecular weight per electron. And the radius of WD can be expressed as ([Zalamea et al. 2010](#)):

$$R_{\text{WD}}(M_{\text{WD}}) \approx 6120 \frac{GM_\odot}{c^2} \left( \frac{M_{\text{WD}}}{M_{\text{Ch}}} \right)^{-1/3} \left( 1 - \frac{M_{\text{WD}}}{M_{\text{Ch}}} \right)^{0.447}, \quad (19)$$

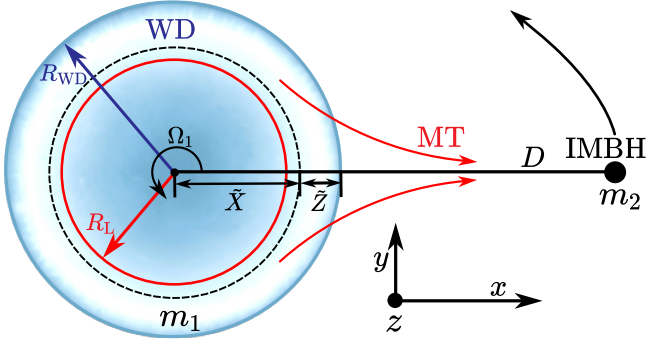
where  $M_{\text{Ch}}$  is the Chandrasekhar mass.

To obtain the density  $\rho$  and pressure  $P$  distribution in a WD under tidal effect, we adopt a quasi-static approach for the WD's surface, assuming the MT process is governed by the gradients in the gravitational potential  $\phi$  and pressure  $P$ . Under the influence of the IMBH's gravitational field and the WD's spin, the hydrostatic equilibrium equation is modified compared to an unperturbed WD ([Sepinsky et al. 2007a](#)). We focus on the one-dimensional distribution along the line connecting the centers of mass:

$$\frac{dP}{d\tilde{Z}} = -\rho \frac{d}{d\tilde{X}} \left[ \frac{Gm_1}{\tilde{X}} + \frac{1}{2} \Omega_1^2 \tilde{X}^2 + \frac{Gm_2}{D} \left( \frac{1}{1 - \tilde{X}/D} - \frac{\tilde{X}}{D} \right) \right], \quad (20)$$

where  $m_1, m_2, \tilde{Z}, \tilde{X}, \Omega_1$  are described in Figure 2. We can integrate Equation (20) by using the EOS, the boundary condition  $\rho(\tilde{Z} = 0) = \rho_{\text{ph}}$  and  $\tilde{X} = R_{\text{WD}} - \tilde{Z}$ . We obtain:

$$\begin{aligned} \rho^{\Gamma-1}(\tilde{Z}) &= \rho_{\text{ph}}^{\Gamma-1} + \frac{\Gamma-1}{K\Gamma} \left\{ \frac{Gm_1}{R_{\text{WD}}} \left( \frac{R_{\text{WD}}}{R_{\text{WD}} - \tilde{Z}} - 1 \right) \right. \\ &\quad \left. - \frac{1}{2} \Omega_1^2 (2R_{\text{WD}} - \tilde{Z})\tilde{Z} + \frac{Gm_2}{D} \left[ \frac{\tilde{Z}}{D} + \frac{D}{D - R_{\text{WD}} + \tilde{Z}} - \frac{D}{D - R_{\text{WD}}} \right] \right\}. \end{aligned} \quad (21)$$



Note: Figure not drawn to scale.

**Figure 2.** The top view of the instantaneous orbital plane. The directions of  $x$ ,  $y$ ,  $z$  are determined by the line connecting the center-of-mass and the rotation axis of WD. The donor (WD) has mass  $m_1$ , and the accretor (IMBH) has mass  $m_2$ . The parameters are as follows:  $\tilde{Z}$  is the depth beneath the donor surface,  $\tilde{X}$  is the distance from the center-of-mass of the donor to the mass element,  $D$  is the distance from the center-of-mass of the donor to the accretor,  $\Omega_1$  is the spin angular velocity of the donor,  $R_{WD}$  is the radius of WD,  $R_L$  is the Roche-lobe radius. The Schwarzschild radius of the IMBH is much larger than the WD radius, so it is not drawn to scale.

The surface (photosphere) density  $\rho_{\text{ph}}$  of a WD, obscured by an external non-degenerate atmosphere, cannot be directly determined. It depends on various factors such as metallicity, evolutionary time, boundary conditions, and the EOS (Cehula & Pejcha 2023a). To represent  $\rho_{\text{ph}}$ , we introduce a dimensionless surface equivalent depth  $\xi_0$ , as an adjustable parameter:

$$\rho_{\text{ph}} := \left[ \frac{\Gamma - 1}{K\Gamma} \left( \frac{GM_{\text{WD}}}{R_{\text{WD}}} \frac{\xi_0}{1 - \xi_0} \right) \right]^{\Gamma-1}. \quad (22)$$

The definition of  $\rho_{\text{ph}}$  is equivalent to the density of a non-rotating WD at depth  $\tilde{Z} = \xi_0 R_{\text{WD}}$  without tidal effect. This definition is convenient in subsequent mathematical treatment. The outermost layer of a WD has a relatively low density  $\rho_{\text{ph}}$ , ranging from  $10^{-5}$  to  $10^{-3} \text{ g cm}^{-3}$  (Ritter 1988; Seymour 1984). We assume that this atmosphere is stripped away before the WD reaches pericenter and cannot be regenerated within one cycle. Consequently, the exposed surface consists of a denser hydrogen or helium layer, with a density of  $10^2$  to  $10^4 \text{ g cm}^{-3}$  (Seymour 1984). While a minimum density of  $10 \text{ g cm}^{-3}$  is considered, the actual value is likely much higher. The parameter  $\xi_0$  can be estimated as

$$\begin{aligned} \xi_0 &\approx \frac{K\rho_{\text{ph}}^{\Gamma-1}}{c^2} \frac{R_{\text{WD}}}{GM_{\text{WD}}/c^2} \frac{\Gamma}{\Gamma-1} \\ &\approx 3.5 \times 10^{-3} \left( \frac{\rho_{\text{ph}}}{10 \text{ g cm}^{-3}} \right)^{2/3} \left( \frac{M_{\text{WD}}}{0.15 M_{\odot}} \right)^{-4/3}. \end{aligned} \quad (23)$$

### 3.2 Mass transfer model

We divide the MT process over one orbital period into two phases: isothermal (optically thin) and adiabatic (optically thick) accretion (Cehula & Pejcha 2023b). If the donor is Roche-lobe underfilling ( $R_{\text{WD}} < R_L$ ), the MT stream is optically thin and isothermal (Lubow & Shu 1975a; Ritter 1988; Jackson et al. 2017). The prescription assumes that, even if  $R_{\text{WD}} < R_L$ , the density profile of donor's atmosphere extends above its photosphere to the first Lagrange point L1. The gas above the photosphere is optically thin to radiation from the donor, but is in equilibrium with the surrounding radiation field

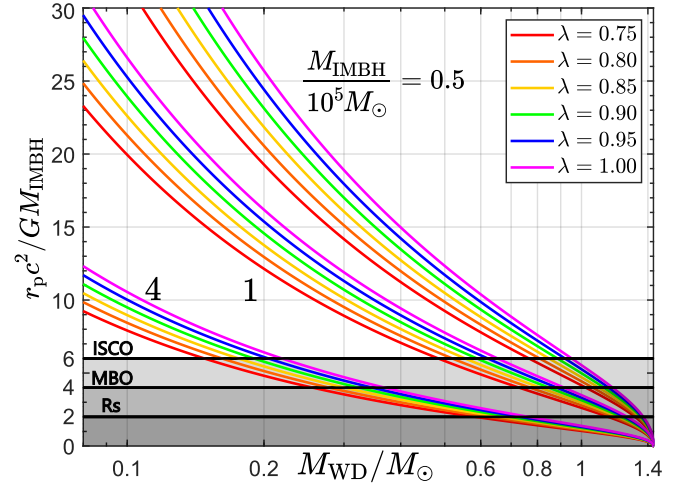


**Figure 3.** The pericenter distance  $r_p$  for Roche-lobe overflow given by  $r_p = \lambda R_{\text{WD}}(M_{\text{WD}}) / f(A, q)$ , is shown as a function of  $M_{\text{WD}}$  for fixed values of  $M_{\text{IMBH}}/10^5 M_{\odot} = 0.5, 1, 4$ . Here,  $\lambda \leq 1$  ensures  $R_L \leq R_{\text{WD}}$  at pericenter. The three black lines represent different distances: ISCO is the innermost stable circular orbit of a Schwarzschild black hole,  $r_{\text{ISCO}} = 6GM_{\text{IMBH}}/c^2$ ; MBO is the marginally bound orbit,  $r_{\text{MBO}} = 4GM_{\text{IMBH}}/c^2$ ;  $R_s$  is the Schwarzschild radius,  $R_s = 2GM_{\text{IMBH}}/c^2$ .

(Cehula & Pejcha 2023b). After the gas passes through L1, it accretes supersonically on to the accretor (Lubow & Shu 1975b).

Conversely, if the donor is Roche-lobe overflowing ( $R_{\text{WD}} > R_L$ ), the MT is optically thick and adiabatic (Kolb & Ritter 1990; Pavlovskii & Ivanova 2015; Marchant, Pablo et al. 2021). It is assumed that there is no energy transport within the gas and between the gas and the surrounding radiation field.

The Roche lobe radius is  $R_L = f(A, q) D$ , where  $f(A, q)$  is a dimensionless function of  $A = \Omega_1^2 D^3 / G(m_1 + m_2)$  and the mass ratio  $q = m_1 / m_2$ . The factor  $A$  represents the ratio of the centrifugal potential by self-rotation to the gravitational potential. Because the WD's rotational angular speed  $\Omega_1$  and pericenter distance  $r_p$  are sufficiently small, we assume  $A \rightarrow 0$  at pericenter (i.e.  $\Omega_1 r_p \ll c\sqrt{R_s/r_p}$ ). Thus,  $f(A, q)$  can be approximated using a zeroth-order expansion near pericenter (Sepinsky et al. 2007a):

$$f(A, q) = \frac{0.5439 - 0.0245 \exp[-(0.5 + \log_{10} q)^2]}{0.6 + \ln(1 + q^{1/3}) q^{-2/3}} + \mathcal{O}(A). \quad (24)$$

For a given value of  $M_{\text{IMBH}}$ , there exists an upper limit for  $M_{\text{WD}}$ , the maximum WD mass that can undergo Roche-lobe overflow without falling into the IMBH. This limit arises from the fact that the WD radius  $R_{\text{WD}}(M_{\text{WD}})$  decreases as the mass increases, allowing a smaller pericenter distance for Roche-lobe overflow, i.e.  $r_p \leq R_{\text{WD}}/f(A, q)$ . However,  $r_p$  cannot be reduced indefinitely, the WD will fall into the IMBH. There is a minimum stable pericenter distance  $r_p^{\text{bound}} \leq r_p$  for bound orbit. The limit to WD mass is given by  $R_{\text{WD}} = f(A, q)r_p$ .

In Figure 3, we show the relationship between  $r_p$  and  $M_{\text{WD}}$  for Roche-lobe overflow to happen, i.e.  $\lambda := f(A, q)r_p/R_{\text{WD}} \leq 1$ , with fixed  $M_{\text{IMBH}}$ . The bound orbit condition for  $r_p^{\text{bound}} = r_{\text{ISCO}}$  leads to the limit to WD mass less than  $0.2 M_{\odot}$ , with  $M_{\text{IMBH}} = 4 \times 10^5 M_{\odot}$ .

To represent the MT rate  $\dot{m}_1$ , we adopt the formulation from Kolb

& Ritter (1990); Jackson et al. (2017); Cehula & Pejcha (2023a):

$$-\dot{m}_1 = \frac{2\pi}{\sqrt{BC}} \left\{ \frac{\rho_{\text{ph}}}{\sqrt{e}} c_{\text{T}}^3 \left[ 1 + [1 - H] \cdot \left( \exp \left( -\frac{\phi_1 - \phi_{\text{ph}}}{c_{\text{T}}^2} \right) - 1 \right) \right] + H \cdot F(K, \Gamma) \left( P_1^{\frac{3\Gamma-1}{2\Gamma}} - P_{\text{ph}}^{\frac{3\Gamma-1}{2\Gamma}} \right) \right\}, \quad (25)$$

where  $H(R_{\text{WD}} - R_{\text{L}})$  is the Heaviside step function, which models the transition between isothermal and adiabatic states. The sound speed can be calculated with  $c_{\text{T}}^2 = P_{\text{ph}}/\rho_{\text{ph}}$ . When  $R_{\text{WD}} < R_{\text{L}}$ , the Roche lobe is underfilling, and Equation (25) simplifies to:

$$-\dot{m}_1^{\text{iso}} = \frac{2\pi}{\sqrt{BC}} \frac{\rho_{\text{ph}}}{\sqrt{e}} c_{\text{T}}^3 \cdot \exp \left( -\frac{\phi_1 - \phi_{\text{ph}}}{c_{\text{T}}^2} \right). \quad (26)$$

Conversely, when  $R_{\text{WD}} > R_{\text{L}}$ , the Roche lobe is overfilling:

$$-\dot{m}_1^{\text{adi}} = \frac{2\pi}{\sqrt{BC}} \left\{ \frac{\rho_{\text{ph}}}{\sqrt{e}} c_{\text{T}}^3 + F(K, \Gamma) \left( P_1^{\frac{3\Gamma-1}{2\Gamma}} - P_{\text{ph}}^{\frac{3\Gamma-1}{2\Gamma}} \right) \right\}. \quad (27)$$

Here, the function  $F(K, \Gamma)$  is given by the  $K, \Gamma$ ,

$$F(K, \Gamma) = K^{\frac{1}{2\Gamma}} \left( \frac{2}{\Gamma+1} \right)^{\frac{\Gamma+1}{2(\Gamma-1)}} \left( \frac{2\Gamma^3/2}{3\Gamma-1} \right). \quad (28)$$

In Equation (26),  $\phi_1 = \phi(\tilde{X} = R_{\text{L}})$ , and  $\phi_{\text{ph}} = \phi(\tilde{X} = R_{\text{WD}})$ . In Equation (27),  $P_1 = P(\tilde{Z} = R_{\text{WD}} - R_{\text{L}})$ , and  $P_{\text{ph}} = P(\tilde{Z} = 0)$ . The pressure  $P(\tilde{Z})$  is described in Equation (21). The potentials  $\phi_1$  and  $\phi_{\text{ph}}$  are determined by  $D$  and  $\tilde{X}_{\text{D}} = \tilde{X}/D$ ,

$$\phi(D, \tilde{X}_{\text{D}}) = -\frac{Gm_2}{D} \left( \frac{q}{\tilde{X}_{\text{D}}} + \frac{1}{2} A(1+q)\tilde{X}_{\text{D}}^2 + \frac{1}{1-\tilde{X}_{\text{D}}} - \tilde{X}_{\text{D}} \right). \quad (29)$$

The factor  $2\pi/\sqrt{BC}$  in Equations (25), (26) and (27) is

$$\frac{2\pi}{\sqrt{BC}} = \frac{2\pi D^3}{Gm_2 \sqrt{\mathfrak{R} [\mathfrak{R} - A(1+q)]}}, \quad (30)$$

where  $\mathfrak{R}$  is defined as

$$\mathfrak{R} := \frac{q}{\tilde{X}_1^3} + \frac{1}{(1-\tilde{X}_1)^3}. \quad (31)$$

Here, dimensionless  $0 < \tilde{X}_1 \ll 1$  denotes the first Lagrangian point L1, which satisfies the following equation (Sepinsky et al. 2007a):

$$\frac{q}{\tilde{X}_1^2} + (1-\tilde{X}_1)^{-2} - A(1+q)\tilde{X}_1 + 1 = 0. \quad (32)$$

The coefficients  $B$  and  $C$  in Equation (30) satisfy (Cehula & Pejcha 2023a)

$$\phi = \phi^x(x) + \frac{B}{2}y^2 + \frac{C}{2}z^2 + O(y^3, z^3), \quad (33)$$

where  $x$  represents the distance from point L1 on the line connecting the center-of-mass, i.e.  $x = \tilde{X} - \tilde{X}_1 D$ . Here,  $y$  and  $z$  are shown in Figure 2.

Although we describe the MT rate using two phases, the transition between the isothermal and the adiabatic phases is continuous, implying  $\dot{m}_1^{\text{iso}} = \dot{m}_1^{\text{adi}}$  when  $R_{\text{WD}} = R_{\text{L}}$  (The reason for choosing isothermal accretion is to ensure the continuity of MT). Near pericenter, the adiabatic MT rate is much greater than the isothermal MT rate at  $R_{\text{WD}} = R_{\text{L}}$ , i.e.  $\dot{m}_1^{\text{adi}}(r_{\text{p}}) \gg \dot{m}_1^{\text{iso}}(R_{\text{WD}} = R_{\text{L}})$ . Far from pericenter, where  $(\phi_1 - \phi_{\text{ph}})/c_{\text{T}}^2 \gg 1$ , the exponential term approaches zero (Equation 26), the MT rate is negligible.

### 3.3 Dynamics under mass transfer

The MT process exchanges energy and angular momentum between the IMBH and the WD. For the evolution of the orbit of the WD, we use the time-varying mass parameters  $m_1(t), m_2(t), m(t), \eta(t), \Delta(t)$ . In addition, we introduce the term  $f_{\text{MT}}$  in the perturbation acceleration  $f$ , employing the form given in Sepinsky et al. (2007b):

$$\begin{aligned} f_{\text{MT}} = & \frac{\dot{m}_1}{m_1} (\mathbf{W}_{\delta m_1} - \mathbf{v}_1 + \boldsymbol{\Omega}_{\text{orb}} \times \mathbf{r}_{A_1}) \\ & - \frac{\dot{m}_2}{m_2} (\mathbf{W}_{\delta m_2} - \mathbf{v}_2 + \boldsymbol{\Omega}_{\text{orb}} \times \mathbf{r}_{A_2}) \\ & + \frac{\dot{m}_1}{m_1} \mathbf{r}_{A_1} - \frac{\dot{m}_2}{m_2} \mathbf{r}_{A_2} + \frac{f_1}{m_1} - \frac{f_2}{m_2}. \end{aligned} \quad (34)$$

Here,  $f_i$  is the total gravitational force exerted on star  $i$  by the particles in the MT stream;  $\boldsymbol{\Omega}_{\text{orb}}$  is the instantaneous angular velocity of the orbit;  $\mathbf{r}_{A_i}$  is the relative position vector on the stellar surface at which mass is lost or accreted;  $\mathbf{W}_{\delta m_i}$  is the absolute velocity of the ejected/accreted mass;  $\mathbf{v}_i$  is the absolute velocity of star  $i$ .

We assume that for the WD,  $\mathbf{r}_{A_1} = -R_{\text{WD}} \hat{\mathbf{r}}$ , and for the IMBH,  $|\mathbf{r}_{A_2}| \rightarrow 0$ . The gravitational effects of the MT flow and the second-order time derivative of mass are neglected. For high-eccentricity WD–IMBH systems, the velocity at pericenter is sufficiently high that some matter may exceed the system's gravitational binding energy, leading to potential mass loss (Rees 1988). We consider the case of non-conservation mass transfer, i.e.  $\dot{m}_1 + \dot{m}_2 < 0$ . More specifically, we assume  $\dot{m} = (1 - \gamma)\dot{m}_1 \leq 0$  and  $\dot{m}_2 = -\gamma\dot{m}_1 \geq 0$ , where  $0 \leq \gamma \leq 1$  represents the MT efficiency from WD to IMBH. The Equation (34) is then reformulated as:

$$f_{\text{MT}} = -\frac{\dot{m}_1}{m_1} [(\mathbf{v}_1 + \gamma q \mathbf{v}_2) - (\mathbf{W}_{\delta m_1} + \gamma q \mathbf{W}_{\delta m_2}) + R_{\text{WD}} \dot{f}_{\text{N}} \hat{\boldsymbol{\lambda}}].$$

To calculate absolute velocity  $\mathbf{v}_1$  and  $\mathbf{v}_2$ , we use the individual positions relative to center-of-mass from Equation (3). The classical center-of-mass relation (OPN) remains valid when we only consider the first-order effects of  $q$ .

Two common methods exist for deriving expressions for  $\mathbf{W}_{\delta m_i}$  (Zalamea et al. 2010; Sepinsky et al. 2007b). The first method assumes that the ejected/accreted mass moves with the same velocity as the donor/accretor (Zalamea et al. 2010), leading to  $\mathbf{W}_{\delta m_1} = \mathbf{v}_1 + R_{\text{WD}} \dot{f}_{\text{N}} \hat{\boldsymbol{\lambda}}$ ,  $\mathbf{W}_{\delta m_2} = \mathbf{v}_2$ , where  $R_{\text{WD}} \ll |\mathbf{v}|/\dot{f}_{\text{N}} \sim r$ . In this case, the MT process only affects  $m_1(t), m_2(t), m(t), \eta(t), \Delta(t)$ , while the form of acceleration remains and  $f_{\text{MT}} = \mathbf{0}$ .

The second method starts from the discussion of orbital angular momentum (Sepinsky et al. 2007b; King 2020, 2022). MT results in the formation of an accretion disk, or the angular momentum might be lost from the system. Part of the angular momentum of the ejected/accreted mass may be transferred to the donor/accretor's spin angular momentum. Orbital angular momentum loss also occurs when binary total mass conservation. To account for both conservative and non-conservative MT processes, we introduce two functions,  $\tilde{f}$  and  $\tilde{g}$ , representing these distinct influences. We define the orbital angular momentum loss due to MT as

$$\frac{J_{\text{orb}}}{J_{\text{orb}}} := \gamma \tilde{f}(\alpha, q, \gamma) \frac{\dot{m}_1}{m_1} + (1 - \gamma) \tilde{g}(\beta, q, \gamma) \frac{\dot{m}}{m}. \quad (35)$$

The functions  $\tilde{f}(\alpha, q, \gamma)$  and  $\tilde{g}(\beta, q, \gamma)$  represent  $J_{\text{orb}}$  loss for conservative and non-conservative MT processes, respectively. The constants  $\alpha$  and  $\beta$  control the  $J_{\text{orb}}$  loss in these functions. These functions satisfy the conditions  $\tilde{f}(0, q, \gamma) = \tilde{f}(\alpha, 0, \gamma) = 0$  and  $\tilde{g}(0, q, \gamma) = \tilde{g}(\beta, 0, \gamma) = 0$ , indicating no  $J_{\text{orb}}$  loss when  $\alpha$  and  $\beta$  vanish and when  $q \rightarrow 0$ . In addition, as  $\gamma \rightarrow 1$ , there is no total mass loss, i.e.  $\tilde{g}(\beta, q, 1) = 0$ .

In addition, using the definition  $J_{\text{orb}} = m\eta\sqrt{Gmp}$ , the time derivative of the orbital angular momentum  $J_{\text{orb}}$  can be expressed as:

$$\frac{\dot{J}_{\text{orb}}}{J_{\text{orb}}} = \frac{\dot{m}_1}{m_1} + \frac{\dot{m}_2}{m_2} - \frac{1}{2} \frac{\dot{m}}{m} + \sqrt{\frac{r}{Gm(1+e\cos f)}} \mathcal{S}, \quad (36)$$

where  $\mathcal{S}$  arises from  $dp/dt$  in Equation (14a). Here,  $\dot{m}_1$  and  $\dot{m}_2$  are from  $d\eta/dt$ . Based on the previous assumptions for  $\dot{m}_2 = -\gamma\dot{m}_1$ , we can rewrite these mass derivative using  $\gamma$  and  $q$ ,

$$\frac{\dot{m}_1}{m_1} + \frac{\dot{m}_2}{m_2} - \frac{1}{2} \frac{\dot{m}}{m} = \frac{\dot{m}_1}{m_1} \frac{2(1-\gamma q^2) + q(1-\gamma)}{2(1+q)}. \quad (37)$$

Equation (35) is an additional equation for reflecting the non-conservation of  $J_{\text{orb}}$  caused by MT, and Equation (36) is a generalized equation determined by the system parameters. These two equations are independent of each other. We equate the right-hand sides of equations (35) and (36), and express  $\dot{m}_2$  and  $\dot{m}$  in terms of  $\gamma$ ,  $q$ , and  $\dot{m}_1$ . The vector  $\mathcal{S}$ , the component of  $\mathbf{f}_{\text{MT}}$  in the direction of  $\lambda$ , can be written as a function of  $q$ ,  $\gamma$ ,  $\tilde{f}$ ,  $\tilde{g}$ ,

$$\begin{aligned} \mathcal{S} &= \left( -\frac{\dot{m}_1}{m_1} \right) r \dot{f}_{\text{N}} \left\{ \frac{2(1-\gamma q^2) + q(1-\gamma)[1-2(1-\gamma)\tilde{g}]}{2(1+q)} - \gamma \tilde{f} \right\} \\ &:= \left( -\frac{\dot{m}_1}{m_1} \right) r \dot{f}_{\text{N}} (1-q) \tilde{h}(q, \gamma, \alpha, \beta). \end{aligned} \quad (38)$$

For  $\gamma=1$  and  $\alpha=0$ , corresponding to mass conservation ( $\dot{m}=0$ ) and no  $J_{\text{orb}}$  loss, (i.e., the right-hand side of Equation (35) is zero), we find  $\tilde{h}(q, 1, 0, \beta) = 1$ , returning to Equation (30) in Sepinsky et al. (2007b).

However, the second method only provides the acceleration in the direction of  $\lambda$  for the MT process, because  $\dot{J}_{\text{orb}}/J_{\text{orb}}$  in Equation (36) only have the function  $\mathcal{S}$ . The form of  $\mathcal{R}$  in the radial direction  $\mathbf{n}$  cannot be derived from orbital angular momentum (Equation 36).

For the following reasons, we can assume that the MT process does not induce acceleration in the radial direction. Because the orbit has high eccentricity, the MT process occurs exclusively at pericenter, i.e.  $\dot{m}_1 \propto \delta(f)$ , then  $\mathcal{R}$  does not need to be determined. This is because the coefficient of  $\mathcal{R}$  in  $de/dt$  in Equation (14b) contains  $\sin f$ , which vanishes at  $f=0$ , and is an odd function. In addition, according to Equation (14), for the pericenter distance variation,  $\dot{r}_{\text{p}} = (\dot{p} - \dot{e}r_{\text{p}})(r_{\text{p}}/p)$ , it is

$$\frac{dr_{\text{p}}}{dt} = \sqrt{\frac{r_{\text{p}}^3}{Gm(1+e)}} \left[ -\sin f \mathcal{R} + \frac{2(2+e+e\cos f)}{1+e\cos f} \sin^2 \frac{f}{2} \mathcal{S} \right]. \quad (39)$$

The presence of  $(\sin f)$  and  $(\sin^2 f/2)$  in this equation, result from  $r_{\text{p}}$  will hardly change compared with  $p$ . Therefore, assuming  $\mathcal{R}=0$  is a reasonable simplification for high-eccentricity systems.

Several points merit further discussion. First, the challenge in both methods is determining the absolute velocity  $\mathbf{W}_{\delta m_i}$  of the ejected/accreted mass in general orbits. Second, the acceleration  $\mathbf{f}_{\text{MT}}$  in Equation (34) is derived using classical Galilean transformation (Sepinsky et al. 2007b), and the  $J_{\text{orb}}$  follows the classical Newtonian form (OPN), i.e.  $J_{\text{orb}} = \sum m_i \mathbf{y}_i \times \mathbf{v}_i$ . However, near pericenter, where  $r_{\text{p}} < 10Gm/c^2$  and the velocity is approximately  $0.1c$ , applying Equation (34) may yield inaccurate results. These limitations should be addressed in future work.

In following Sections 4, 5 and 6, we adopt the second method, which yields Equation (38). We only consider the conservation of total mass and orbital angular momentum where  $\tilde{h}=1$ , and thus do not specify the exact forms of the functions  $\tilde{f}(\alpha, q, \gamma)$  and  $\tilde{g}(\beta, q, \gamma)$ . The first method assumes co-velocity motion, which causes the MT to appear weak and does not introduce additional dynamical effects

that contribute to MT or accretion. Moreover, to understand the first method from the second method's perspective, we can take  $\mathcal{S}=0$  in Equation (36). In this case, orbital angular momentum is not conserved. Under the assumption of total mass conservation and  $q \ll 1$ , we have  $\dot{J}_{\text{orb}}/J_{\text{orb}} \approx \dot{m}_1/m_1$ , meaning that all angular momentum from the transferred mass is lost. This assumption is less reasonable than the second method.

## 4 SHORT-TERM ORBITAL EVOLUTION USING POST-NEWTONIAN METHOD

In this section, we analyze the orbital evolution of an EMRI system using the PN method, as described in Section 2.1. We adopt the PN method rather than the Kerr spacetime geodesic approach because it provides a specific form of the perturbation acceleration, as shown in Equation (4). The acceleration  $\mathbf{f}_{\text{MT}}$  from MT can be directly added to this perturbation. Such a simulation is simple. In contrast, converting the geodesic equation into an acceleration form and applying the perturbed Kepler method is challenging, as is incorporating the effect of gravitational radiation into geodesics.

Section 4.1 establishes the relationship between the latitude angle  $\psi$ , and the orbital elements  $f$ ,  $\omega$ ,  $\phi$ ,  $\Omega$ ,  $\iota$ . Here,  $\psi$  is the angle between the instantaneous orbital plane and the equatorial plane, which is perpendicular to the IMBH's spin axis. Section 4.2 neglects the MT process for a moment and shows the results of the variable  $\epsilon = (R_{\text{WD}} - R_{\text{LP}})/R_{\text{WD}}$ , radial eccentricity  $e_r$ , and period  $T$ . Section 4.3 includes the MT process and compare the effects of MT and gravitational radiation on key orbital parameters.

### 4.1 Angular relationship in relative coordinate

We use the relative coordinate system shown in Figure 1, with the XYZ axes corresponding to the spherical coordinates  $(r, \theta, \varphi)$ , i.e.  $(r^X, r^Y, r^Z) = r(\sin \theta \cos \varphi, \sin \theta \sin \varphi, \cos \theta)$ . From Equation (9), we derive  $\theta = \cos^{-1}(\sin \iota \sin \phi)$ . The angle  $\theta$  is the polar angle, with its complement  $\psi = \pi/2 - \theta$  referred to as the latitude.

We align the IMBH spin direction along the Z-axis and set the WD at pericenter at the initial time, i.e.  $f_0 = \phi_0 - \omega_0 = 0$ . Additionally, we assume  $\varphi_0 = \pi/2$ . The subscript 0 denotes the initial moment. All the orbital angular parameters are then given by  $\Omega_0 = \pi/2 - \varphi_0$ ,  $\iota_0 = \pi/2 - \theta_0$ ,  $\phi_0 = \varphi_0$ ,  $\omega_0 = \phi_0 - f_0$ .

We define the direction of the spin angular momentum using the angles  $\vartheta$  and  $\varphi$  along with the vectors  $\mathbf{n}$ ,  $\lambda$ ,  $\ell$

$$\frac{\mathbf{S}_A}{|\mathbf{S}_A|} := \sin \vartheta_A \cos \varphi_A \mathbf{n} + \sin \vartheta_A \sin \varphi_A \lambda + \cos \vartheta_A \ell, \quad (40)$$

where  $|\mathbf{S}_A| = \chi_A Gm_A^2/c$ . Here,  $\chi_A$  is a dimensionless spin size parameter, generally ranging from 0 to 1. The initial spin  $\mathbf{S}_{20}$  of the IMBH can be expressed as  $|\mathbf{S}_{20}|(\cos \theta_0 \mathbf{n} + \sin \theta_0 \ell)$ . From Equation (40), the initial angle relations between the pairs  $(\theta_0, \varphi_0)$  and  $(\vartheta_{20}, \varphi_{20})$  are given by  $\vartheta_{20} = \frac{\pi}{2} - \theta_0 = \iota_0$  and  $\varphi_{20} = 0$ . In Kerr spacetime,  $|\psi_0| = |\pi/2 - \theta_0|$  represents the maximum latitude of the geodesic (Schmidt 2002; Fujita & Hikida 2009).

In general, the initial angle conditions are

$$\begin{aligned} \Omega_0 &= 0, & \psi_0 &= \iota_0 = \frac{\pi}{2} - \theta_0, & \phi_0 &= \frac{\pi}{2}, & \omega_0 &= \frac{\pi}{2}, & f_0 &= 0, \\ \vartheta_{20} &= \frac{\pi}{2} - \theta_0, & \varphi_{20} &= 0. \end{aligned} \quad (41)$$

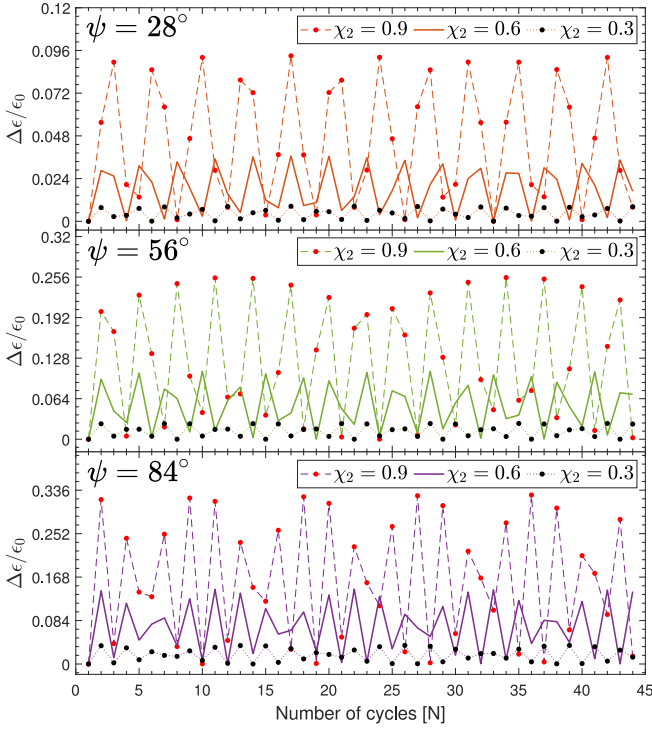


**Figure 4.** The evolution of  $\Delta\epsilon/\epsilon_0$  with PN method, where  $\Delta\epsilon(N) := \epsilon(N) - \epsilon_0$ . Here,  $\epsilon_0 = 5 \times 10^{-3}$ , and  $\epsilon(N) = 1 - r_p(N)C_L/R_{WD}$  represents the ratio of the difference between the  $R_{LP}$  and  $R_{WD}$  with the specific  $\chi_2$  and initial  $\psi_0$  indicated in the legend. Other orbital parameters are specified in Sections 4.1 and 4.2.

## 4.2 Orbital evolution without mass transfer

In this section, we use the PN method without the MT process in the orbital evolution analysis, providing a template for comparison. The pericenter distance  $r_p$  and radial eccentricity  $e_r = (r_a - r_p)/(r_a + r_p)$  can be roughly determined. First, the MT process requires that  $R_{LP} = f(A, q)r_p \leq R_{WD}(M_{WD})$ , as outlined in Section 3.2, with  $M_{WD}^{\text{limit}}(M_{\text{IMBH}}, r_p^{\text{bound}}) \ll M_{\text{ch}}$ , which directly constrains the range of  $r_p$ . Second, due to the Hills mechanism, and to match the periods observed in QPE light curves (Miniutti et al. 2019; Miniutti, G. et al. 2023a), the radial eccentricity  $e_r > 0.9$ .

We assume that the spin of the low-mass WD can be ignored, setting  $\chi_1 = 0$ . We also set the mass  $m_1 = M_{WD} = 0.15 M_\odot$ ,  $m_2 = M_{\text{IMBH}} = 4 \times 10^5 M_\odot$ , and  $q = m_1/m_2 = 3.75 \times 10^{-7}$ .

Because the initial pericenter distance  $r_{p0}$  is determined based on the relationship between  $R_{LP}$  and  $R_{WD}$ , where  $R_{LP} = f(A, q)r_p := (1 - \epsilon)R_{WD} < R_{WD}$ . We quantify  $r_{p0}$  using the dimensionless variable  $\epsilon(r_p, M_{WD}, q) = 1 - r_p C_L(q)/R_{WD}(M_{WD})$ , which reflects the difference between  $R_{LP}$  and  $R_{WD}$ , where  $C_L = f(A = 0, q)$ . Then we set the initial  $\epsilon_0 = 5 \times 10^{-3}$ . Therefore,  $r_{p0} \approx 3.1502 \times 10^6 \text{ GM}_\odot/c^2 \approx 7.875 \text{ Gm}_2/c^2 \approx 253.87 R_{WD}(M_{WD})$ . We fix the  $r_{p0}$  in Section 4. For the radial eccentricity, we set  $e_r = 0.99$ , when  $\chi_2 = 0$ . This choice for  $r_{p0}$  and  $e_r$  allows us to maintain consistent initial orbital parameters when reconsidering MT process in other sections.

For initial angular configurations, we use the angular relationships described in Section 4.1. We only need to adjust initial latitude  $\psi_0$  and IMBH spin parameter  $\chi_2$ . We set  $\psi_0 = 0^\circ, 28^\circ, 56^\circ, 84^\circ$ , and  $\chi_2 = 0, 0.3, 0.6, 0.9$ .

Studying the changes in  $\epsilon$  helps us understand the impact of PN orbits on the MT process. In Figure 4, we show the evolution of

**Table 1.** The average radial eccentricity  $\bar{e}_r$  and the difference  $e_{r\text{max}} - \bar{e}_r$ , and the average period  $\bar{T}$  and the ratio of the difference  $(T_{\text{max}} - \bar{T})/\bar{T}$  without the MT process.

$\bar{e}_r - 0.99$	$\chi_2 = 0$	$\chi_2 = 0.3$	$\chi_2 = 0.6$	$\chi_2 = 0.9$
$\psi_0 = 0^\circ$	0	-0.0200	-0.0396	-0.0588
$\psi_0 = 28^\circ$	0	-0.0177	-0.0352	-0.0525
$\psi_0 = 56^\circ$	0	-0.0113	-0.0228	-0.0344
$\psi_0 = 84^\circ$	0	-0.0023	-0.0048	-0.0077
$e_{r\text{max}} - \bar{e}_r$	$\chi_2 = 0$	$\chi_2 = 0.3$	$\chi_2 = 0.6$	$\chi_2 = 0.9$
$\psi_0 = 0^\circ$	5.358e-6	5.019e-6	4.984e-6	4.954e-6
$\psi_0 = 28^\circ$	5.358e-6	2.146e-5	7.786e-5	1.959e-4
$\psi_0 = 56^\circ$	5.358e-6	5.164e-5	2.168e-4	5.223e-4
$\psi_0 = 84^\circ$	5.358e-6	7.477e-5	2.904e-4	6.508e-4
$\bar{T}$	$\chi_2 = 0$	$\chi_2 = 0.3$	$\chi_2 = 0.6$	$\chi_2 = 0.9$
$\psi_0 = 0^\circ$	76.460	14.911	7.0774	4.3667
$\psi_0 = 28^\circ$	76.460	16.772	8.1180	5.0305
$\psi_0 = 56^\circ$	76.460	24.730	13.055	8.3270
$\psi_0 = 84^\circ$	76.460	56.415	42.455	32.573
$(T_{\text{max}} - \bar{T})/\bar{T}$	$\chi_2 = 0$	$\chi_2 = 0.3$	$\chi_2 = 0.6$	$\chi_2 = 0.9$
$\psi_0 = 0^\circ$	7.992e-4	2.511e-4	1.501e-4	1.080e-4
$\psi_0 = 28^\circ$	7.992e-4	1.158e-3	2.602e-3	4.850e-3
$\psi_0 = 56^\circ$	7.992e-4	3.588e-3	9.925e-3	1.789e-2
$\psi_0 = 84^\circ$	7.992e-4	9.162e-3	2.961e-2	5.620e-2

$\Delta\epsilon/\epsilon_0$  for different  $\chi_2$  and  $\psi_0$ . When  $\chi_2 \neq 0$  and  $\psi_0 \neq 0^\circ$ , we find that  $\Delta\epsilon/\epsilon_0 \geq 0$ . At  $t = 0$ , all cases start with the same initial  $r_{p0}$  and  $\epsilon_0$ . However, over time, variations in  $\epsilon$  arise due to the PN terms in Equation (4). In some cases,  $\epsilon$  exhibits a double-cycle structure. Higher  $\psi_0$  and larger  $\chi_2$  amplify the oscillatory behavior of  $\epsilon$ .

The relationship between  $\Delta\epsilon$  and  $\Delta r_p$  ( $\Delta\epsilon \ll \epsilon$ ,  $\Delta r_p \ll r_p$ ) can be expressed using a first-order Taylor expansion, where  $\epsilon = 1 - r_p C_L/R_{WD}$ :

$$\frac{\Delta\epsilon}{1 - \epsilon} \approx -\frac{\Delta r_p}{r_p} - \frac{\Delta(C_L/R_{WD})}{C_L/R_{WD}}, \quad (42)$$

where  $\Delta(C_L/R_{WD})$  reflects the change of  $M_{WD}$  and  $M_{\text{IMBH}}$ . In the absence of the MT process,  $\Delta(C_L/R_{WD}) = 0$ . From Equation (42),  $\epsilon$  changes as  $r_p$  varies. Because  $\epsilon \ll 1$ , we find that  $\Delta\epsilon/\epsilon \approx -\Delta r_p/(r_p\epsilon) \gg -\Delta r_p/r_p$ . When  $\chi_2$  and  $\psi_0$  are large, a jitter in  $r_p$  of  $10^{-4}$  can alter  $\epsilon$  by over 10%, significantly impacting the MT rate upon reconsideration of the MT process. This underscores the importance of emphasizing short-term evolution characteristics in the PN method.

This oscillation phenomenon also exists for radial eccentricity  $e_r$  and orbital period  $T$ . We give the average values and the maximum jitter difference of  $e_r$  and  $T$  in Table 1. Lower  $\chi_2$  and higher initial  $\psi_0$  lead to higher  $\bar{e}_r$  and  $\bar{T}$ . However, higher  $\chi_2$  and initial  $\psi_0$  enhance the jitter difference of the  $\Delta e_r$  and  $\Delta T$ .

We note that the relationship between  $\bar{e}_r$  and  $\bar{T}$  and the relationship between  $\Delta e_r$  and  $\Delta T$ , can be explained by Kepler's law even though the equations of motion include PN corrections. Using Kepler's period expression  $T \propto a^{3/2}$ , where  $a = (r_a + r_p)/2$ , and applying a first-order expansion for  $\Delta T \ll \bar{T}$ , we can get

$$\frac{\bar{T}_1}{\bar{T}_2} = \left( \frac{\bar{r}_{p1} (1 - \bar{e}_{r2})}{\bar{r}_{p2} (1 - \bar{e}_{r1})} \right)^{3/2} = \left( \frac{\bar{r}_{a1} (1 + \bar{e}_{r2})}{\bar{r}_{a2} (1 + \bar{e}_{r1})} \right)^{3/2} \approx \left( \frac{\bar{r}_{a1}}{\bar{r}_{a2}} \right)^{3/2},$$

$$\frac{\Delta T}{\bar{T}} \approx \frac{3}{2} \frac{\Delta r_a + \Delta r_p}{\bar{r}_a + \bar{r}_p} \approx \frac{3}{2} \frac{\Delta e_r}{1 - \bar{e}_r}. \quad (43)$$

The above two equations provide good fit to the results presented in Table 1. These relationships can also help us calculate the effects of MT and gravitational radiation in Section 4.3.

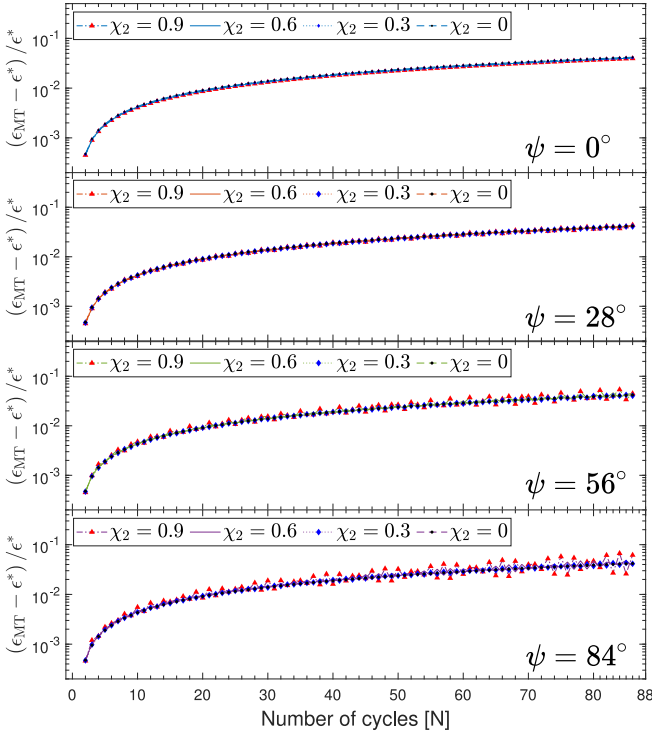


**Figure 5.** The evolution of  $(\epsilon_{\text{MT}} - \epsilon^*) / \epsilon^*$  due to the MT process, where  $\epsilon_{\text{MT}}$  denotes  $\epsilon$  with MT ( $\xi_0 = 3.98 \times 10^{-3}$ ), and  $\epsilon^*$  denotes  $\epsilon$  without MT. For the same initial  $\psi_0$ , the results for different  $\chi_2$  are shown in a single subfigure. In the top panel, where  $\psi_0 = 0^\circ$ , the four lines do not overlap; the lower the  $\chi_2$ , the greater the value.

In Table 1,  $\bar{T}$  decreases significantly with higher  $\chi_2$  and lower initial  $\psi_0$ . This reduction in  $\bar{T}$  arises from the contraction of orbit (the pericenter distance  $r_p$  remains almost constant, while the apocenter distance  $r_a$  changes greatly), as  $\bar{T}_1/\bar{T}_2 \approx (\bar{r}_{a1}/\bar{r}_{a2})^{3/2}$  in Equation (43). For instance,  $r_a$  with  $e_r = 0.99$  is seven times larger than that with  $e_r = 0.93$  under same  $r_p$ . The significant variation in orbital contraction by spin, is due to the fact that all the considered orbits are prograde with respect to the spin angular momentum of the IMBH. The frame-dragging effect of  $\chi_2$  increases the orbital energy. As the value of  $\chi_2$  increases and the orbit gets closer to the equatorial plane with lower  $\psi_0$ , this effect becomes more significant.

The distinctive periodic oscillation effect in Figure 4 does not occur in the geodesic of Kerr spacetimes, nor is it present in non-spinning binary systems using the PN method. We speculate that this effect arises from the spin terms  $\mathbf{a}_{\text{SO}}$ ,  $\mathbf{a}_{\text{SS}}$ ,  $\mathbf{a}_{\text{SOPN}}$  in the PN orbital dynamics described in Equation (4), derived from Tagoshi et al. (2001) using the harmonic gauge condition. Furthermore, we found that the changes in  $\Delta\epsilon/\epsilon_0$  does not decrease in higher-order relative acceleration terms (below 4 PN) when using equations from different PN orders to reproduce the same  $r_p$  and  $T$ . This suggests that higher-order terms involving the spin parameter  $\chi_2$  should be considered, or it may indicate a subtle connection between harmonic coordinates and Boyer-Lindquist coordinates.

### 4.3 Orbital evolution with mass transfer

In this subsection, we analyze the orbits using the PN method with the MT processes.

Compared with Section 4.2, the only new parameter introduced is  $\xi_0$ , which regulates the WD surface density  $\rho_{\text{ph}}$  in Equation (22).

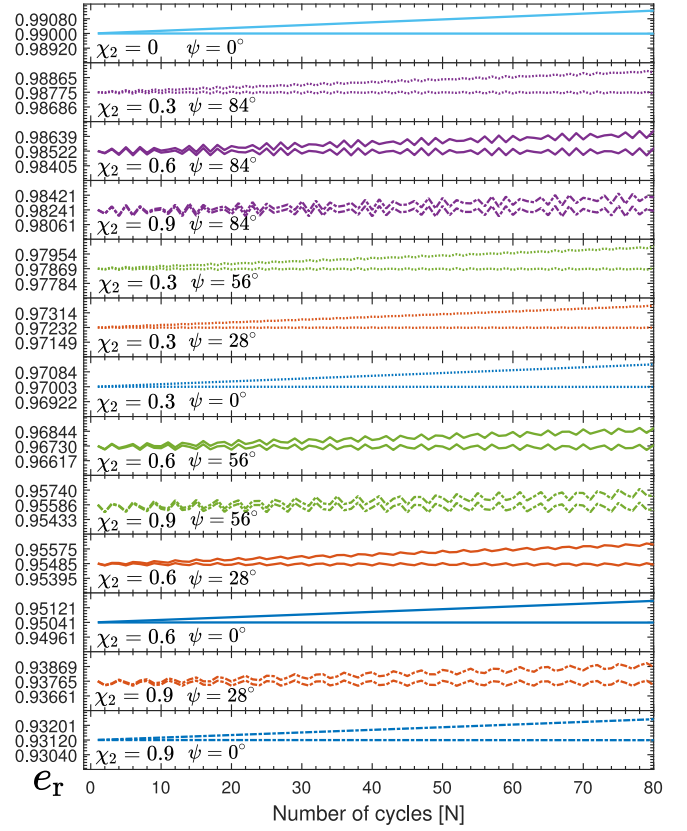


**Figure 6.** The evolution of the radial eccentricity  $e_r$  with and without MT. In each panel, the higher curve represents the evolution of  $e_r^{\text{MT}}$  with MT, and the low one represents the evolution of  $e_r$  without MT. Different line colors correspond to the same initial latitude  $\psi_0$ , and different line styles denote the same IMBH spin parameters  $\chi_2$ .

Here, we set  $\xi_0 = 3.98 \times 10^{-3}$ . We continue to assume that  $\chi_1 = 0$ , and use the same values for  $m_1$ ,  $m_2$ ,  $e_0$  and  $\epsilon_0$  as given in Section 4.2. We still set  $\psi_0 = 0^\circ, 28^\circ, 56^\circ, 84^\circ$ , and  $\chi_2 = 0, 0.3, 0.6, 0.9$ , consistent with the setup in Section 4.2. We examine the influence of the MT process on the evolution of  $\epsilon_{\text{MT}}$  (Figure 5),  $e_r^{\text{MT}}$  (Figure 6), and  $T_{\text{MT}}$  (Figure 7) for different  $\chi_2$  and  $\psi_0$ .

In Figure 5, different values of  $\chi_2$  and  $\psi_0$  have almost no effect on  $(\epsilon_{\text{MT}} - \epsilon^*) / \epsilon^*$ , the periodic oscillations caused by the PN method are tightly concentrated around a single curve on the logarithmic plot. This indicates that spin is not strongly related to the growth of  $\epsilon_{\text{MT}}$  under MT.

According to Equation (42),  $\Delta(C_L/R_{\text{WD}}) / (C_L/R_{\text{WD}}) \neq 0$  causes  $(\epsilon_{\text{MT}} - \epsilon^*) / \epsilon^*$  to grow with time in Figure 5. To understand the relative importance of  $\Delta(C_L/R_{\text{WD}}) / (C_L/R_{\text{WD}})$ , we give the first-order expansion by  $\Delta M_{\text{WD}}/M_{\text{WD}}$ , using the Equations (19) and (24):

$$-\frac{\Delta(C_L/R_{\text{WD}})}{C_L/R_{\text{WD}}} \approx -\frac{2 + q\gamma}{3} \frac{\Delta M_{\text{WD}}}{M_{\text{WD}}} > 0. \quad (44)$$

Here,  $\Delta$  represents the difference between the MT process and the process without MT. From the results of numerical calculation, we find  $|\Delta M_{\text{WD}}/M_{\text{WD}}| \gg |\Delta r_p/r_p|$ . Therefore, in Equation (42),

$$\frac{\epsilon_{\text{MT}} - \epsilon^*}{\epsilon^*} \approx -\frac{\Delta(C_L/R_{\text{WD}})}{C_L/R_{\text{WD}}} \approx -\frac{2 + q\gamma}{3} \frac{\Delta M_{\text{WD}}}{M_{\text{WD}}} > 0. \quad (45)$$

Equation (45) shows that the evolution trend of  $\Delta M_{\text{WD}}$  is almost unaffected by the spin of IMBH, and this explains the behavior of the curves in Figure 5.

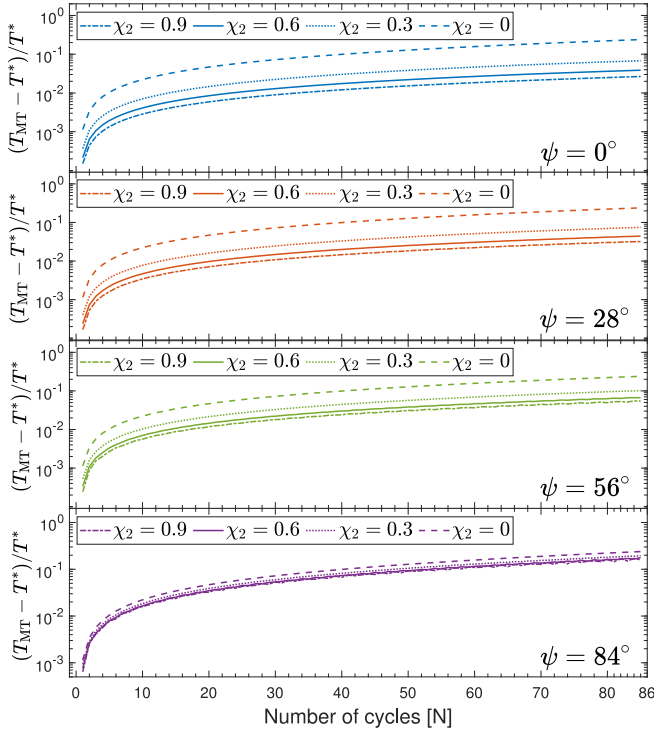


**Figure 7.** The evolution of  $(T_{\text{MT}} - T^*)/T^*$  due to the MT process, where  $T^*(N)$  denotes the period without MT process. In contrast,  $T_{\text{MT}}(N)$  represents the period with MT ( $\xi_0 = 3.98 \times 10^{-3}$ ). We give the influence of different  $\chi_2$  under identical initial  $\psi_0$  conditions.

Using the results of numerical calculation, we give the changes in  $r_p$  and  $\epsilon$  for every cycle, i.e.  $\delta r_p := r_p(N) - r_p(N-1)$ . On average,  $\delta \bar{r}_p^{\text{GW}}/\bar{r}_p \approx -3.3 \times 10^{-8}$  and  $\delta \bar{r}_p^{\text{GW+MT}}/\bar{r}_p \approx -1.7 \times 10^{-8}$ ;  $\delta \bar{\epsilon}^{\text{GW}}/\bar{\epsilon} \approx 5.5 \times 10^{-6}$  and  $\delta \bar{\epsilon}^{\text{GW+MT}}/\bar{\epsilon} \approx 4.6 \times 10^{-4}$ .

Since  $\delta \bar{r}_p^{\text{GW}} < \delta \bar{r}_p^{\text{GW+MT}} < 0$ , the MT process results in a slower decay compared to the case where only gravitational radiation is considered. We also find  $\delta \bar{\epsilon}^{\text{GW+MT}} \gg \delta \bar{\epsilon}^{\text{GW}}$ , according to Equations (42) and (44), it shows the MT process lead to  $|\delta M_{\text{WD}}/M_{\text{WD}}| \gg |\delta r_p/r_p|$ . This relationship arises from the radius-mass relation of the WD given in Equation (19). As the WD mass decreases, its radius increases. And in Equation (24), as  $q \rightarrow 0$ , we find  $R_L \propto q^{1/3}$ . Because MT causes  $q$  to decrease,  $R_L$  decreases slightly. These significantly enlarging the difference between  $R_{\text{WD}}$  and  $R_L$ , and then increase MT rate. A compact object as donor whose radius decreases after its mass decreases will not have this effect.

However, the ratio  $\delta \bar{r}_p^{\text{GW+MT}}/\bar{r}_p$  and  $\delta \bar{\epsilon}^{\text{GW+MT}}/\bar{\epsilon}$  are much smaller than the jitter of magnitude  $10^{-2}$  to  $10^{-1}$  caused by the spin in the PN method. Our simulations suggest that at least  $10^2$  to  $10^3$  cycles are needed for the MT effect to significantly exceed the jitter caused by the PN terms, after which we can observe the increase in  $\epsilon$  due to the MT process. The required number of cycles depends on  $\chi_2$  and initial  $\psi_0$ .

Although the effect of MT on the evolution of  $\epsilon$  is weak and takes many orbital cycles to become discernible, the effects on orbital eccentricity and period much more quickly becomes significant and observable. In Figure 6, the evolution of  $e_r$  with MT and  $e_r^*$  without MT are shown. Radial eccentricity  $e_r$  is decreased by gravitational radiation, but is increased by MT. The increasing rate of  $e_r$  with MT is  $\delta e_r^{\text{GW+MT}} \approx 10^{-5}$ , in contrast to a decrease of  $\delta e_r^{\text{GW}} \approx -10^{-7}$  only by gravitational radiation. Therefore, the MT effect is more dominant than gravitational radiation.

Figure 7 shows that, the orbital period becomes longer when MT is introduced, and the increment is larger for higher  $\psi_0$  and lower  $\chi_2$ . This result, in fact, can be inferred from the increase of  $e_r$  as described in Equation (43). We also get  $\delta \bar{T}_{\text{GW+MT}}/\bar{T} \approx 10^{-3}$ , and  $\delta \bar{T}_{\text{GW}}/\bar{T} \approx 10^{-5}$ . By comparing with  $(T_{\text{max}} - \bar{T})/\bar{T}$  in Table 1, we find that within  $10^2$  cycles, the change of period by the MT process completely masks the PN jitter effect, so no obvious jitter effect is found in Figure 7.

## 5 LONG-TERM EVOLUTION WITH MASS TRANSFER

Applying the PN method for calculations is computationally expensive, especially for long-duration simulations. Consequently, we employ a Keplerian orbital approximation and time-average approach to efficiently evaluate the long-term evolution.

First, we analyze the combined effects of the MT process and gravitational radiation on the long-term orbital evolution, as described in Section 5.1.1. To calculate the transferred mass  $\delta M_{\text{WD}}$  from the WD over one orbital period, we use the MT rate  $\dot{m}_1$  given in Equation (25), as detailed in Section 5.1.2 and Appendices B and C. Second, we orbital-average the parameters and analyze the long-term MT effects on a Keplerian elliptical orbit in Section 5.2. Third, we verify the accuracy of our long-term calculations through short-term numerical calculations in Section 5.3.

### 5.1 Relevance of the mass transfer effects

#### 5.1.1 The relative importance of MT and gravitational radiation

In this section, we use the second method in Section 3.3 to calculate the orbital evolution with MT. According to Equation (38), the MT acceleration  $f_{\text{MT}}^{\mathcal{B}}$  is

$$f_{\text{MT}}^{\mathcal{B}} = \left( -\frac{\dot{m}_1}{m_1} \right) r \dot{f}_N (1-q) \tilde{h} \lambda. \quad (46)$$

We can give the instantaneous change  $\dot{a}$  using  $\dot{p}$  and  $\dot{e}$  in Equation (14). In this case, using the periodic integral of Equation (46), we provides the secular change rate of the orbital semimajor axis  $\langle \dot{a}_{\text{MT}}^{\mathcal{B}} \rangle_{\text{sec}}$ , which can be expressed as

$$\langle \dot{a}_{\text{MT}}^{\mathcal{B}} \rangle_{\text{sec}} = \left( -\frac{\delta M_{\text{WD}}}{M_{\text{WD}}} \right) \sqrt{\frac{GM_{\text{WD}}}{c^2 a_r}} \frac{c}{\pi} \frac{1+e_r}{1-e_r} (1-q) \sqrt{\frac{1+q}{q}} \tilde{h}, \quad (47)$$

where  $\delta M_{\text{WD}}$  represents the transferred mass of the WD during each orbital period. Here,  $\langle \dots \rangle_{\text{sec}}$  is the periodic average operator.

In Section 3.3, we have assumed a MT rate  $\dot{m}_1$  without providing a formula to calculate it. Based on the assumptions made by Sepinsky et al. (2007b), we propose that the MT rate  $\dot{m}_1$  at high eccentricity  $e_r \lesssim 1$ , can be expressed as  $\dot{M}_{\text{WD}} := \dot{M}_0 \delta(f)$ . Therefore,  $\delta M_{\text{WD}}$  is calculated as:

$$\delta M_{\text{WD}} = \int_{-\pi}^{\pi} \dot{M}_0 \delta(f) \dot{f}_N^{-1} df \approx \dot{M}_0 \sqrt{\frac{a_r^3}{Gm}} \frac{(1-e_r)^{3/2}}{(1+e_r)^{1/2}}. \quad (48)$$

Conversly,  $\dot{M}_0$  can be expressed in terms of  $\delta M_{\text{WD}}$  as follows:

$$\dot{M}_0 \approx \frac{\delta M_{\text{WD}}}{T} 2\pi \frac{(1+e_r)^{1/2}}{(1-e_r)^{3/2}}. \quad (49)$$

In addition, the average change in the semi-major axis due to quadrupole gravitational radiation  $\langle \dot{a}_{\text{GW}} \rangle_{\text{sec}}$  is given by Peters (1964):

$$\langle \dot{a}_{\text{GW}} \rangle_{\text{sec}} = - \left( \frac{GM_{\text{WD}}}{c^2 a_r} \right)^3 \frac{64}{5} c \frac{1+q}{q^2} \frac{1 + \frac{73}{24} e_r^2 + \frac{37}{96} e_r^4}{(1-e_r^2)^{7/2}}. \quad (50)$$

Because  $\delta M_{\text{WD}} < 0$ , we have  $\langle \dot{a}_{\text{GW}} \rangle_{\text{sec}} < 0 < \langle \dot{a}_{\text{MT}}^{\mathcal{B}} \rangle_{\text{sec}}$ . To identify the dominant process that determines the evolution of  $a$ , we calculate the ratio  $\left| \dot{a}_{\text{MT}}^{\mathcal{B}} / \dot{a}_{\text{GW}} \right|_{\text{sec}}$ , which is given by

$$\left| \frac{\dot{a}_{\text{MT}}^{\mathcal{B}}}{\dot{a}_{\text{GW}}} \right|_{\text{sec}} = \left( -\frac{\delta M_{\text{WD}}}{M_{\text{WD}}} \right) \sigma^{-1}, \quad (51)$$

$$\sigma = \tilde{\lambda}^{-5/2} q \frac{64}{5} \pi \frac{1 + \frac{73}{24} e_r^2 + \frac{37}{96} e_r^4}{(1 + e_r)^{9/2}} \frac{\sqrt{1+q}}{(1-q)\tilde{h}},$$

where  $\tilde{\lambda} := r_p / (Gm_2/c^2) \approx 7.875$ ,  $q = 3.75 \times 10^{-7}$ ,  $e_r = 0.99$  and  $\tilde{h} = 1$  under the orbital conditions specified in Section 4. Following this condition, we find  $\sigma = 1.7 \times 10^{-8}$ . For gravitational radiation to dominate, the system should satisfy  $\left| \dot{a}_{\text{MT}}^{\mathcal{B}} / \dot{a}_{\text{GW}} \right|_{\text{sec}} < 1$ , which implies  $|\delta M_{\text{WD}}| < 1.7 \times 10^{-8} M_{\text{WD}}$  per period. Under the above orbital conditions with  $M_{\text{WD}} = 0.15 M_{\odot}$  and  $T \sim 76$  hr, this leads to  $|\dot{M}_{\text{WD}}|_{\text{sec}} < 2.94 \times 10^{-7} M_{\odot} \text{ yr}^{-1}$ . This represents an exceptionally low MT rate. Because  $\langle \dot{a}_{\text{MT}}^{\mathcal{B}} \rangle_{\text{sec}} \propto |\delta M_{\text{WD}}| (1 - e_r)^{-1}$  in Equation (47), for  $\langle \dot{a}_{\text{MT}}^{\mathcal{B}} \rangle_{\text{sec}} = -\langle \dot{a}_{\text{GW}} \rangle_{\text{sec}}$ , we can get  $|\delta M_{\text{WD}}| \propto -\langle \dot{a}_{\text{GW}} \rangle_{\text{sec}} (1 - e_r)$ . The factor  $(1 - e_r)$  in Equation (47) is a small amount arises from the integral of the MT rate in Equation (48). Therefore, the low transferred mass  $|\delta M_{\text{WD}}|$  is due to the high eccentricity.

Our above conclusion differs from that of Wang et al. (2022). Their  $\dot{M}_{\text{WD}}$  corresponds to our  $\dot{M}_0$  in Equation (49); however,  $\dot{M}_0 < 0$  does not represent an instantaneous MT rate. They neglected the factor  $(1 - e_r)^{-3/2} \gg 1$  for  $\dot{M}_0$ . As a result, they suggest that  $|\delta M_{\text{WD}}| > 10^{-3} M_{\text{WD}}$  is required for the MT process to dominate, i.e.  $\left| \dot{a}_{\text{MT}}^{\mathcal{B}} / \dot{a}_{\text{GW}} \right|_{\text{sec}} > 1$ , based on their parameters.

### 5.1.2 Simplification of MT model

To investigate the orbital evolution induced by  $f_{\text{MT}}^{\mathcal{B}}$ , it is essential to estimate the  $\delta M_{\text{WD}}$ . Direct calculations using Equation (25) does not readily reveal the dependencies of  $\delta M_{\text{WD}}$  on the variables  $r_p$ ,  $e$ ,  $M_{\text{WD}}$ , and  $M_{\text{IMBH}}$ . Therefore, we simplify the integration of  $\dot{m}_1$  by expressing it as a function of these variables.

We introduce the variable  $\varepsilon := (R_{\text{WD}} - R_{\text{L}}) / R_{\text{WD}}$ , where we consider the limiting case  $0 \leq \varepsilon \ll 1$  at pericenter. Note that  $\varepsilon$  is distinct from  $\epsilon$ , but they are related by  $\epsilon = \varepsilon(D = r_p)$ .

In estimating the transferred mass per cycle, we will exclude the effect of  $\dot{m}_1^{\text{iso}}$  from Equation (26) on  $\delta M_{\text{WD}}$  and only consider  $\dot{m}_1^{\text{adi}}$  from Equation (27), because the isothermal accretion is important only when the WD is far away from the pericenter. Away from the pericenter, the dynamic effect of MT is negligible given our assumption of a delta-function for the MT rate.

The simplified expression for  $\dot{m}_1$  is

$$\dot{m}_1 \approx -H(\varepsilon) \cdot 2\pi \cdot W(K, \Gamma) \cdot (GM_{\text{IMBH}})^2 \frac{C_{\text{L}}^3}{\sqrt{\mathcal{R}_0}} \times \left( \sum_{m=0}^{\infty} S_m \varepsilon^m \right) \left( \sum_{n=0}^{\infty} \mathcal{U}_{\varepsilon n} \varepsilon^n \right), \quad (52)$$

where  $W(K, \Gamma) = F(K, \Gamma) \cdot \left[ K^{-\frac{1}{\Gamma}} (\Gamma - 1) / \Gamma \right]^{\frac{3\Gamma-1}{2(\Gamma-1)}}$ . Expressions for the coefficients  $\mathcal{R}_0$ ,  $S_m$ , and  $\mathcal{U}_{\varepsilon n}$  are provided in Appendix B.

For a Keplerian elliptical orbit, the integral of  $\dot{m}_1$  over a full period

can be rearranged as

$$\delta M_{\text{WD}} \approx \int_{-\pi}^{\pi} \dot{m}_1 \dot{f}_N^{-1} df = C \dot{m}_1 \sqrt{\frac{p^3}{Gm}} \sum_{n=0}^{\infty} C_{\varepsilon n} \int_{-f_0}^{f_0} \frac{\varepsilon(f)^n df}{(1 + e \cos f)^2}, \quad (53)$$

where  $C \dot{m}_1$  and  $C_{\varepsilon n}$  are derived in Appendix C. The  $f_0$  represents the critical phase satisfying  $R_{\text{L}}(f_0) = R_{\text{WD}}$ , i.e.  $\varepsilon(f_0) = 0$ . The expression of  $f_0(e, \varepsilon)$  in Equation (C9) is due to  $\varepsilon(f_0) = 0$  and the variable  $\epsilon = \varepsilon(f = 0)$ . The definite integral can be expressed in terms of the Appell hypergeometric function,  $\text{AF1}(\alpha; \beta, \beta'; \gamma; x, y)$ . For a Keplerian elliptical orbit, the function  $\delta M_{\text{WD}}(\varepsilon, e, M_{\text{WD}}, q)$  is

$$\delta M_{\text{WD}} \approx \frac{4 C \dot{m}_1 r_p^{3/2}}{\sqrt{Gm}} \sqrt{\frac{\epsilon}{2e}} \sum_{n=0}^{\infty} \sum_{m=0}^{\infty} C_{\varepsilon n} \binom{n}{m} (-1)^m (1 - \epsilon)^m \times \text{AF1} \left[ \frac{1}{2}; \frac{1}{2}, m+2; \frac{3}{2}; \frac{1+e}{2e} \epsilon, \epsilon \right]. \quad (54)$$

### 5.2 Long-term orbital effects in Newtonian elliptical orbits

To evaluate the long-term orbital evolution, we also require the secular change rate of orbital eccentricity. For MT,  $\langle \dot{e}_{\text{MT}}^{\mathcal{B}} \rangle_{\text{sec}}$  is obtained using Equations (14b) and (46). For gravitational radiation,  $\langle \dot{e}_{\text{GW}} \rangle_{\text{sec}}$  is taken from Peters (1964):

$$\langle \dot{e}_{\text{MT}}^{\mathcal{B}} \rangle_{\text{sec}} = \left( -\frac{\delta M_{\text{WD}}}{M_{\text{WD}}} \right) \sqrt{\frac{GM_{\text{WD}}}{c^2 a_r}} \frac{c(1+e_r)}{\pi a_r} (1-q) \sqrt{\frac{1+q}{q}} \tilde{h},$$

$$\langle \dot{e}_{\text{GW}} \rangle_{\text{sec}} = - \left( \frac{GM_{\text{WD}}}{c^2 a_r} \right)^3 \frac{304}{15} \frac{c}{a_r} \frac{1+q}{q^2} \frac{e_r}{(1-e_r^2)^{5/2}} \left( 1 + \frac{121}{304} e_r^2 \right). \quad (55)$$

For the pericenter distance, using  $\langle \dot{r}_p \rangle_{\text{sec}} \approx (1-e) \langle \dot{a} \rangle_{\text{sec}} - a \langle \dot{e} \rangle_{\text{sec}}$ :

$$\langle \dot{r}_{\text{pMT}}^{\mathcal{B}} \rangle_{\text{sec}} = 0, \quad (56)$$

$$\langle \dot{r}_{\text{pGW}} \rangle_{\text{sec}} = - \left( \frac{GM_{\text{WD}}}{c^2 a_r} \right)^3 \frac{64}{5} c \frac{1+q}{q^2} \frac{\left( 1 - \frac{7}{12} e_r + \frac{7}{8} e_r^2 + \frac{47}{192} e_r^3 \right)}{(1-e_r)^{3/2} (1+e_r)^{7/2}}.$$

The result  $\langle \dot{r}_{\text{pMT}}^{\mathcal{B}} \rangle_{\text{sec}} = 0$  indicates that the MT process does not affect  $r_p$ . In Section 3.3, Equation (39) shows that, with the MT rate treated as a delta function, it does not lead to any change in  $r_p$ .

Assuming  $\gamma = 1$ , the orbital period is approximately  $\langle \dot{T} \rangle_{\text{sec}} \approx 3\pi \sqrt{a/Gm} \langle \dot{a} \rangle_{\text{sec}} = 3T \langle \dot{a} \rangle_{\text{sec}} / 2a$ . Hence, we have:

$$\langle \dot{T}_{\text{MT}}^{\mathcal{B}} \rangle_{\text{sec}} = \left( -\frac{\delta M_{\text{WD}}}{M_{\text{WD}}} \right) 3 \frac{1+e_r}{1-e_r} (1-q), \quad (57)$$

$$\langle \dot{T}_{\text{GW}} \rangle_{\text{sec}} = - \left( \frac{GM_{\text{WD}}}{c^2 a_r} \right)^{5/2} \frac{64}{5} 3\pi \sqrt{\frac{1+q}{q^3}} \frac{1 + \frac{73}{24} e_r^2 + \frac{37}{96} e_r^4}{(1-e_r^2)^{7/2}}.$$

Now, we can make qualitative predictions about the long-term evolution:

(i) If the pericenter distance  $r_p \geq R_{\text{WD}}/C_{\text{L}}$  (i.e.  $\epsilon \leq 0$ ), the Roche lobe is underfilled, and the MT rate is negligible. In this case, we can assume that orbital decay is driven only by gravitational radiation, i.e.  $\left| \dot{a}_{\text{MT}}^{\mathcal{B}} / \dot{a}_{\text{GW}} \right|_{\text{sec}} = 0$  and  $\delta M_{\text{WD}} = 0$ . Consequently,  $a$ ,  $e$ ,  $T$  and  $r_p$  all decrease.

(ii) When  $r_p < R_{\text{WD}}/C_{\text{L}}$  (i.e.  $\epsilon > 0$ ), and  $0 < \left| \dot{a}_{\text{MT}}^{\mathcal{B}} / \dot{a}_{\text{GW}} \right|_{\text{sec}} < 1$ , gravitational radiation still dominates. In this case,  $a$ ,  $e$ ,  $T$  and  $r_p$  continue to decrease. However,  $\epsilon$  gradually increases due to the radius-mass relationship of the WD (see Section 4.3 for details). Thus, according to Equation (54),  $|\delta M_{\text{WD}}|$  and  $\left| \dot{a}_{\text{MT}}^{\mathcal{B}} / \dot{a}_{\text{GW}} \right|_{\text{sec}} < 1$  gradually increases.

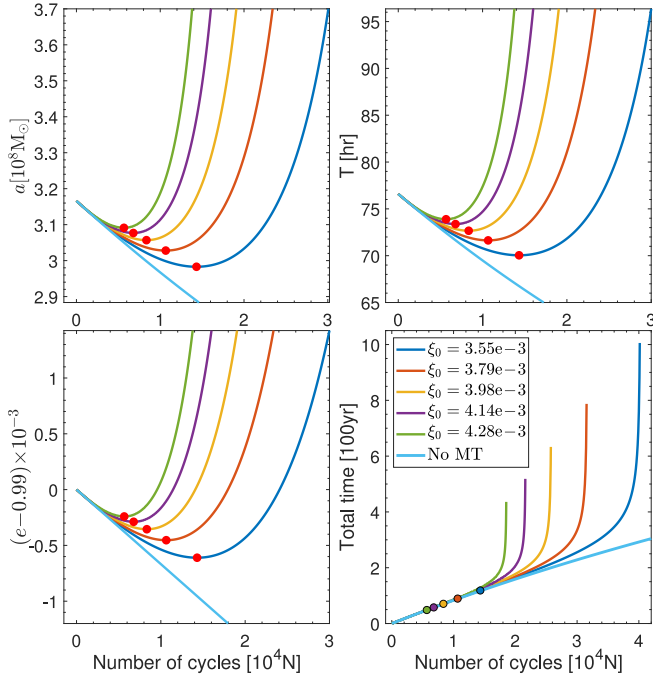


**Figure 8.** The evolution of  $a$ ,  $T$ ,  $e$ , and total time respectively. The evolution of  $a$ ,  $T$ ,  $e$  are synchronous. Red marks indicate the points where  $a$ ,  $T$ ,  $e$  reach their minimum values, and total time reach its inflection value. The sky blue curves show the results when MT is not included in the calculation, and hence they do not show minimum or inflection points.

(iii) As  $|\dot{a}_{\text{MT}}^{\mathcal{B}}/\dot{a}_{\text{GW}}|_{\text{sec}} \rightarrow 1$ , both  $a$  and  $T$  reach their minimum values simultaneously. Similarly, as  $|\dot{e}_{\text{MT}}^{\mathcal{B}}/\dot{e}_{\text{GW}}|_{\text{sec}} \rightarrow 1$ , the eccentricity  $e$  reaches its minimum value. The times at which  $a$ ,  $T$  reach their minima differ slightly from the time when  $e$  does, as the change rates due to gravitational radiation follow different formulae.

(iv) Beyond the threshold where  $|\dot{a}_{\text{MT}}^{\mathcal{B}}/\dot{a}_{\text{GW}}|_{\text{sec}} = 1$ , the parameters  $a$ ,  $T$ , and  $e$  will increase according to the equations in Sections 5.1.1 and 5.2. At this point, MT begins to dominate. However,  $\delta M_{\text{WD}}$  continues to rise as described by Equation (54), and  $r_{\text{p}}$  continues to decrease as given by Equation (56).

In the absence of other mechanisms, the MT process remains dominant without reverting to gravitational radiation dominance. Since  $\langle \dot{r}_{\text{p}} \rangle_{\text{sec}} = \langle \dot{r}_{\text{pMT}}^{\mathcal{B}} \rangle_{\text{sec}} + \langle \dot{r}_{\text{pGW}} \rangle_{\text{sec}} \leq 0$  always holds according to Equation (56), we infer that the MT process of a WD in a bound, high-eccentricity orbit around an IMBH is inherently irreversible.

Therefore, the long-term evolution for  $f_{\text{MT}}^{\mathcal{B}}$  may lead to two outcomes:

(i) Tidal disruption occurs when  $r_{\text{p}}$  falls below the tidal radius  $R_{\text{t}} \approx R_{\text{WD}} (M_{\text{IMBH}}/M_{\text{WD}})^{1/3}$  (Rees 1988). In our notation, the condition for tidal disruption is  $r_{\text{p}} = (1-\epsilon)R_{\text{WD}}/C_{\text{L}} < R_{\text{t}}$ , which is equivalent to  $\epsilon > \epsilon_{\text{t}} = 1 - C_{\text{L}} q^{-1/3} \sim 0.465$  for  $q \ll 1$ , where the value is obtained by taking  $q \rightarrow 0$  in  $\epsilon_{\text{t}}(q)$ , with  $C_{\text{L}}(q)$  given by Equation (24).

(ii) The WD escapes the gravitational potential of the IMBH, when  $e \geq 1$  but  $\epsilon < \epsilon_{\text{t}}$ .

The occurrence of these situations depends on the initial conditions. When  $\epsilon_0$  is slightly smaller than  $\epsilon_{\text{t}}$ , tidal disruption is more likely. While when  $\epsilon_0$  is much smaller than  $\epsilon_{\text{t}}$ , the WD is more likely to escape from the system. We note that for  $f_{\text{MT}}^{\mathcal{A}} = \mathbf{0}$ , the case follows the description in Zalamea et al. (2010), tidal disruption is inevitable.

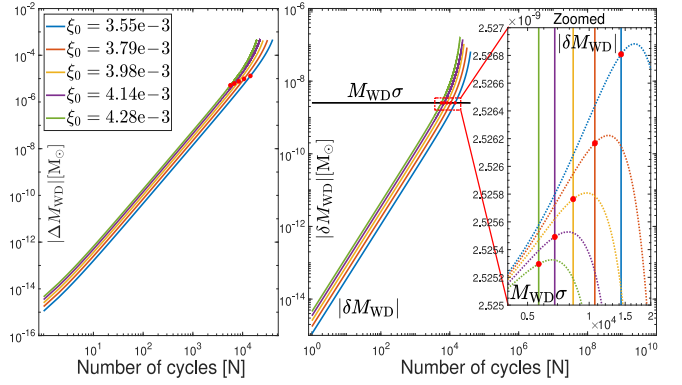


**Figure 9.** The evolution of  $M_{\text{WD}}$  over time due to the MT process. Left panel:  $|\Delta M_{\text{WD}}| := |M_{\text{WD}}(N) - M_{\text{WD}}(0)|$ , representing the total mass lost from  $t = 0$  to the end of the  $N$ -th cycle. Right panel:  $|\delta M_{\text{WD}}| := |M_{\text{WD}}(N) - M_{\text{WD}}(N-1)|$ , representing the transferred mass from the WD per cycle. The black lines show curves for different values of  $\xi_0$  of the function  $M_{\text{WD}}\sigma$ , which are clustered together. The zoomed in plot highlights  $|\delta M_{\text{WD}}|$  (solid line) and  $M_{\text{WD}}\sigma$  (dashed line). Red marks indicate the points where  $a$  and  $T$  reach their minimum values, which also correspond to the intersection of  $|\delta M_{\text{WD}}|$  and  $M_{\text{WD}}\sigma$ .

We consider spinless WD and IMBH with initial conditions:  $e_0 = 0.99$ ,  $\epsilon_0 = 0$ ,  $m_{10} = 0.15 M_{\odot}$ ,  $m_{20} = 4 \times 10^5 M_{\odot}$ . The parameter  $\xi_0$  in Equations (22) and (B4) is used to adjust  $\delta M_{\text{WD}}$ , with values  $\xi_0 \times 10^3 = 3.55, 3.79, 3.98, 4.14, 4.28$ .

In Figure 8, we show the evolution of  $a$ ,  $T$ ,  $e$ , and the total elapsed time, respectively. Initially, with  $\epsilon = 0$ , gravitational radiation dominates, causing  $a$ ,  $T$ ,  $e$  to decrease. After reaching the minimum, the three parameters begin to increase as the MT effect becomes dominant. The lower the initial value of  $\xi_0$ , the longer time it takes to reach the minimum, and the lower the minimum values. The evolution of the total elapsed time shows that, in the absence of the MT process, the slope decreases with increasing orbital cycles, corresponding to the decline in  $T$  due to gravitational radiation. After the inflection point, where the MT process becomes dominant, the slope increases, corresponding to the rise in  $T$  due to the MT effect. The red point on each curve marks the transition from GW-dominated evolution to an MT-dominated one. Figure 8 is consistent with the evolution we predicted earlier in this section.

In Figure 9, we show the evolution of  $M_{\text{WD}}$ . Smaller  $\xi_0$  requires more cycles to achieve the same mass, because it results in a lower MT rate  $|\dot{m}_1|$ . Although  $\xi_0$  differs for each line, when  $|\dot{a}_{\text{MT}}^{\mathcal{B}}/\dot{a}_{\text{GW}}|_{\text{sec}} \rightarrow 1$ ,  $\delta M_{\text{WD}}$  remains almost unchanged (i.e., the values of red points in the right panel are nearly the same). This is because the size of  $\sigma$  in Equation (51) is only related to  $q$ ,  $e_{\text{r}}$ , and  $r_{\text{p}}$ . In the right panel,  $M_{\text{WD}}\sigma(N)$  shows little change (The black lines show curves for different values of  $\xi_0$  of the function  $M_{\text{WD}}\sigma$  which are clustered together, with  $\sigma \approx 1.7 \times 10^{-8}$ ). This function is closely tied to the initial conditions, and since all our evolutions use the same initial orbital parameters, the function's initial value is the same for each dashed line.

In Figure 10, we show the evolution of  $\epsilon$ . The presence or absence of MT significantly affects  $\epsilon$ . From Equations (42) and (44), the integral for  $\epsilon(N)$  with  $\epsilon(N=0) = 0$  is

$$\begin{aligned} \epsilon(N) &\approx 1 - \frac{r_{\text{p}}(N)}{r_{\text{p}}(0)} \left( \frac{M_{\text{WD}}(N)}{M_{\text{WD}}(0)} \right)^{\frac{2+\gamma q(N)}{3}} \\ &\approx -\frac{\Delta r_{\text{p}}(N)}{r_{\text{p}}(N)} - \frac{2+\gamma q(N)}{3} \frac{\Delta M_{\text{WD}}(N)}{M_{\text{WD}}(N)}. \end{aligned} \quad (58)$$

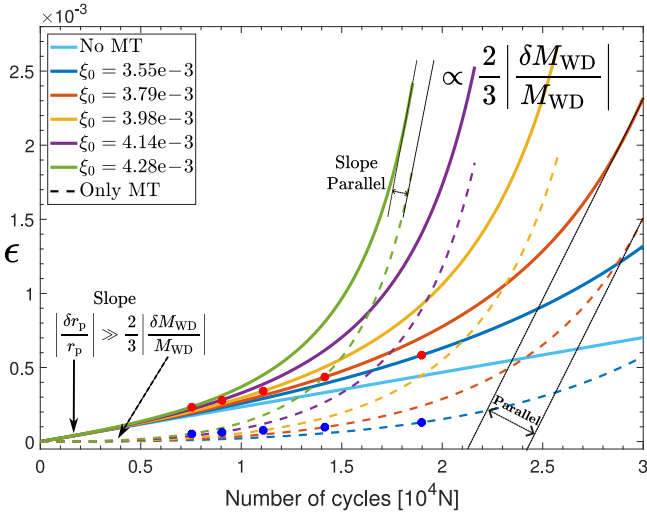


**Figure 10.** The evolution of  $\epsilon = 1 - r_p C_L / R_{\text{WD}}$  on long timescale. Sky blue solid line is the evolution of  $\epsilon$  without MT. Solid lines in other colors are the cases where both gravitational radiation and the MT process are considered. Dashed lines are the function  $1 - (M_{\text{WD}}(N)/M_{\text{WD}}(0))^{(2+\gamma q(N))/3}$ . Red and blue marks indicate the points where  $a$  and  $T$  reach the minimum.

where  $\Delta r_p(N) := r_p(N) - r_p(0)$ ,  $\Delta M_{\text{WD}}(N) := M_{\text{WD}}(N) - M_{\text{WD}}(0)$ . The slope  $d\epsilon/dN \approx \epsilon(N) - \epsilon(N-1)$  is  $|\delta r_p/r_p| + 2/3 |\delta M_{\text{WD}}/M_{\text{WD}}|$ . When the MT effect is weak,  $\epsilon$  is very small, and gravitational radiation dominates, causing  $|\delta r_p/r_p| \gg |\delta M_{\text{WD}}/M_{\text{WD}}|$ . According to Equation (56), the change in  $r_p$  is entirely governed by gravitational radiation. Thus, the initial slopes of solid lines in Figure 10 are similar. For comparison, we also plot the function obtained by excluding the change in  $r_p$  from Equation (58) (dashed line). The initial slope of the dashed line is nearly zero, reflecting that the MT effect is very weak at the beginning. When the MT effect dominates,  $|\delta r_p/r_p| \ll |\delta M_{\text{WD}}/M_{\text{WD}}|$ , this relationship has also been shown in the numerical simulations in Section 4.3. The fundamental reason for this relationship is the radius-mass relationship of the WD shown in Equation (19). Therefore, the slopes for the solid and dashed lines start to converge to  $2/3 |\delta M_{\text{WD}}/M_{\text{WD}}|$ .

### 5.3 Verification of long-term results

In Sections 5.1 and 5.2, we computed the evolution of Newtonian elliptical orbits. In Section 4, we include the effects of PN dynamics terms, specifically the contributions of  $\mathcal{A}$ ,  $\mathcal{B}$ , and the accelerations  $\mathbf{a}_{\text{SO}}$ ,  $\mathbf{a}_{\text{SS}}$ ,  $\mathbf{a}_{\text{SOPN}}$  in Equation (4). In long-term evolution, we observe minima in the evolution of orbital parameters (Figure 8), and the MT rate approaches consistency near these minima (Figure 9). To validate the long-term results, it is necessary to obtain the same conclusions in short-term calculations. In these, orbital parameters such as  $a$ ,  $T$ , and  $e$  should also reach their minimum values. When MT and gravitational radiation are in equilibrium, the transferred mass per cycle,  $\delta M_{\text{WD}}$ , should remain unaffected by  $\xi_0$ , i.e.  $|\delta M_{\text{WD}}| = M_{\text{WD}}\sigma$ , when  $|\dot{a}_{\text{MT}}/\dot{a}_{\text{GW}}|_{\text{sec}} = 1$ . We aim to investigate the minimum of  $a$  during short-term evolution using parameters from Section 5.2, and analyze  $\delta M_{\text{WD}}$  near  $a_{\text{min}}$ . In these short-term calculations, we do not assume a delta function for the MT rate  $\dot{M}_{\text{WD}}$  in Equation (48) (we use Equation 25), nor do we use the time-averaged orbital parameter change rate per cycle (we use Equation 14). As these phenomena occur near the minimum, we focus on the evolution over 100 cycles to verify these conclusions. The initial orbital parameters for the

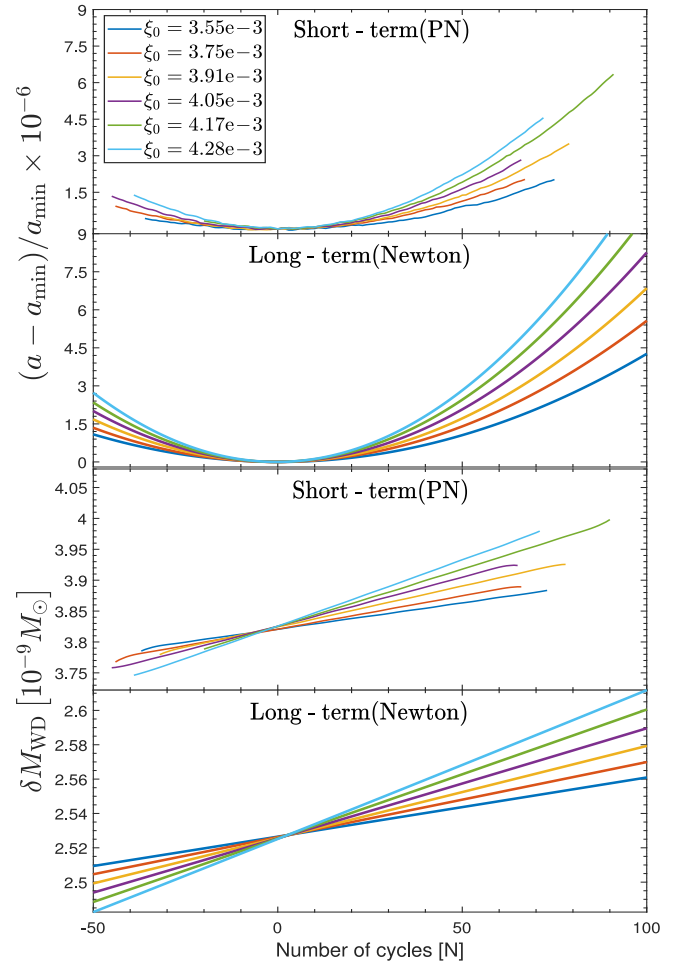


**Figure 11.** Comparison of the short-term and long-term evolution of  $(a - a_{\text{min}})/a_{\text{min}}$  and  $\delta M_{\text{WD}}$ . The short-term evolution uses the PN results from Section 4.3. The long-term evolution uses the Newtonian elliptical orbit results from Section 5.2. The x-axis is set to  $N(a_{\text{min}}) = 0$ .

short-term calculation are adjusted to correspond to those of the first few cycles before the minimum.

In Figure 11, we compare the short-term and long-term evolution of  $(a - a_{\text{min}})/a_{\text{min}}$  and  $\delta M_{\text{WD}}$ . For different values of  $\xi_0$ , the minimum  $a_{\text{min}}$  varies, we normalize the results by the ratio  $(a - a_{\text{min}})/a_{\text{min}}$ . As  $\xi_0$  increases, the rate of change of  $a$  accelerates, indicating that larger  $\xi_0$  correspond to more intense MT effects.

We also show the variation of  $\delta M_{\text{WD}}$  near  $a_{\text{min}}$  in Figure 11. According to Equation (51),  $\delta M_{\text{WD}}$  near  $a_{\text{min}}$  is independent on  $\xi_0$ . Therefore, for the same initial values of  $r_{p0}$ ,  $e_{r0}$  and  $q_0$ , the transferred mass  $\delta M_{\text{WD}}$  should converge into a value that  $|\delta M_{\text{WD}}| = M_{\text{WD}}\sigma$ . This convergence is well demonstrated in Figure 11 for both short-term and long-term evolution. The reasoning behind this behavior is explained in Figure 9 and Equation (58) for long-term evolution, and it is confirmed from short-term evolution in Figure 11.

Therefore, we confirm that the MT rate can be represented as a delta function at high eccentricity, and the time-averaged form can be used to calculate the evolution well. Furthermore, in the absence of effects other than MT and gravitational radiation, the evolution of orbital parameters inevitably exhibits extremal points.

**Table 2.** The time required for the phase difference to reach 1 radian, for the different initial  $e_0$  and  $\epsilon_0$ , with same  $\xi_0 = 3.55 \times 10^{-3}$ . The time unit is year.

$e_0 \backslash \epsilon_0$	0.980	0.982	0.984	0.986	0.988	0.990	0.992	0.994
0	7.188	8.170	9.427	11.087	13.367	16.674	21.846	30.934
0.30e-4	4.267	4.785	5.436	6.280	7.413	9.013	11.437	15.521
0.60e-4	2.945	3.286	3.713	4.263	4.999	6.032	7.587	10.186
0.90e-4	2.266	2.524	2.847	3.262	3.816	4.593	5.760	7.707
1.20e-4	1.858	2.068	2.330	2.667	3.117	3.748	4.694	6.272
3.51e-4	0.847	0.941	1.059	1.210	1.412	1.695	2.119	2.826
3.73e-4	0.809	0.899	1.011	1.156	1.349	1.619	2.024	2.699
3.95e-4	0.775	0.861	0.969	1.107	1.292	1.551	1.938	2.584

## 6 IMPACT ON GW SIGNAL AND DETECTION

As shown in Figure 8, after the same evolution time around the IMBH, the orbital period of the WD with MT and gravitational radiation is longer than that with only gravitational radiation. When  $\delta M_{\text{WD}}$  exceeds the limit value in Equation (51), the period can even increase over time. Because of the change of period, the MT process induces a phase shift in the GW signal. Over a sufficiently long observational time, the accumulated phase difference due to MT can be detected. In the following, we evaluate whether the MT could induce an accumulative phase shift as large as 1 radian over a period of  $t_{\text{obs}} = 5$  yr. Such a phase shift would be detectable by LISA and other space-based GW detectors (Kocsis et al. 2011; Derdzinski et al. 2019; Zwick et al. 2022; Zhang et al. 2024a).

Our orbit is highly eccentric, resulting in a nonlinear evolution of the orbital phase over time, which complicates the calculation of the phase shift. In the GW waveform, significant change of the amplitude occurs near pericenter over very short durations, appearing as periodic pulses in the time domain (Poisson & Will 2014; McCarr et al. 2021; Hughes et al. 2021). Since the period  $T$  changes very slowly due to the MT process, and the phase of each cycle always spans  $2\pi$ , it is unnecessary to compute the exact phase as a function of time during each period for our purposes. Instead, we can estimate the period of each cycle, which is sufficient to address the problem. We can demonstrate that (Appendix D), for the same number of cycles, the difference in total time is directly proportional to the difference in phase.

By the proof in Appendix D, when the conditions  $N \gg 1$  and  $T_N \ll \sum_{k=1}^{N-1} T_k$  are satisfied, we can replace time  $t$  with  $\sum_{k=1}^{N-1} T_k$  to approximate the phase change. Here,  $T_k$  represents the period of the  $k$ -th cycle, and  $N$  represents the integer value that satisfies the following inequality:

$$0 \leq \frac{|\Delta u_g|}{2\pi} \frac{1 - \varsigma_N}{\varsigma_N} - \frac{\sum_{k=1}^{N-1} T_k \varsigma_k}{T_N \varsigma_N} \leq 1, \quad (59)$$

where  $\Delta u_g$  represents the phase difference we want (in our requirements,  $\Delta u_g = -1$ ),  $\varsigma_k$  represents the difference between the period with MT and the period without MT in the  $k$ -th cycle, i.e.  $\varsigma_k := (T_k - T_k^*)/T_k > 0$ . Here, the superscript asterisk indicates that MT process is not considered. Inequality (59) is equivalent to Inequality (D6a). For the value of  $N$  is calculated from Inequalities (59) and (D6a), if the total time for the first  $(N-1)$  cycles,  $t_{pN-1} = \sum_{k=1}^{N-1} T_k$ , is less than the observation time  $t_{\text{obs}}$ , the phase shift caused by MT is observable within  $t_{\text{obs}}$ .

For a fixed mass combination, such as  $m_1 = 0.15 M_\odot$ ,  $m_2 = 4 \times 10^5 M_\odot$ ,  $q = 3.75 \times 10^{-7}$ , we use the long-term evolution of Newtonian elliptical orbits as described in 5.2. Therefore, only parameters  $e_0$ ,  $\epsilon_0$ , and  $\xi_0$  need to be adjusted. We fix the variable  $\xi_0 = 3.55 \times 10^{-3}$ . The initial values of  $e_0$  and  $\epsilon_0$  reflecting different initial periods and

**Table 3.** The time required for the semi-major axis  $a$  reaches its minimum value due to gravitational radiation and the MT process, for the different initial  $e_0$  and  $\epsilon_0$ , with same  $\xi_0 = 3.55 \times 10^{-3}$ . The time unit is year.

$e_0 \backslash \epsilon_0$	0.980	0.982	0.984	0.986	0.988	0.990	0.992	0.994
3.51e-4	4.132	4.842	5.779	7.061	8.898	11.692	16.324	25.081
3.73e-4	2.147	2.514	3.003	3.668	4.620	6.078	8.487	13.047
3.95e-4	0.213	0.246	0.294	0.353	0.445	0.585	0.806	1.240

pericenter distances. Table 2 shows the time required for the phase difference to reach 1 radian. Table 3 shows the time required for the semi-major axis  $a$  to reach its minimum.

In both Tables 2 and 3, the time required to observe the desired phase shift increases with increasing  $e_0$  and decreasing  $\epsilon_0$ . These variations are linked to the strength of MT. Increasing eccentricity  $e$  with a constant pericenter distance  $r_p$  reduces the angular range  $f_0$  over which MT occurs (Equation C9), shortening the Roche lobe overflow time in one period and decreasing the transferred mass  $\delta M_{\text{WD}}$  (Equation 54). This results in a weaker MT effect and a longer required time. Conversely, decreasing the pericenter distance  $r_p$  at constant eccentricity  $e$  increases  $\epsilon$ , the Roche radius  $R_L$  decreases, leading to an increase in  $\delta M_{\text{WD}}$ . This strengthens the MT effect and reduces the required time.

When the initial  $\epsilon_0$  is small, the time for the phase difference to reach 1 radian (Table 2) is shorter than the time for the semi-major axis  $a$  to reach its minimum (Table 3). However, for sufficiently large initial  $e_0$  (as shown in the last row of Tables 2 and 3), the value in Table 2 exceeds that in Table 3. Because the initial ratio  $|\dot{a}_{\text{MT}}^{\mathcal{B}}/\dot{a}_{\text{GW}}|_{\text{sec}}$  is non-zero, but the phase difference accumulates over time. There is no phase difference at the initial moment: it starts at zero initially. When the initial ratio  $|\dot{a}_{\text{MT}}^{\mathcal{B}}/\dot{a}_{\text{GW}}|_{\text{sec}}$  is large enough, the time of the phase difference to reach 1 radian exceeds the time to reach equilibrium. Therefore, in the observed GW signal, in addition to being able to detect the phase difference of MT, there may be a stage dominated by MT, i.e.  $|\dot{a}_{\text{MT}}^{\mathcal{B}}/\dot{a}_{\text{GW}}|_{\text{sec}} > 1$ .

For sufficiently large  $e_0$  and small  $\epsilon_0$ , the phase shift can be detected within the observation time  $t_{\text{obs}}$ . For initial eccentricity  $e_0 \approx 0.99$ , the required  $\epsilon_0$  should be greater than  $10^{-3}$ . The pericenter distance  $r_p = (1 - \epsilon)R_{\text{WD}}(m_1)/C_L(q)$  for  $\epsilon = 10^{-3}$  is nearly unchanged compared to  $\epsilon = 0$  ( $r_p \approx 7.875 Gm_2/c^2$  with  $m_1 = 0.15 M_\odot$  and  $m_2 = 4 \times 10^5 M_\odot$ ). This means a small change in pericenter distance  $r_p$  leads to a significant change in the required time, as shown in Table 2.

## 7 DISCUSSION

### 7.1 Implications for QPEs

The MT process may cause the WD to escape the gravitational potential of the IMBH (Section 5.2), potentially explaining the disappearance of the QPE signal in GSN 069, as reported by Miniutti, G. et al. (2023a,b). GSN 069, the first galactic nucleus to exhibit QPEs, was identified in December 2018. These high-amplitude, soft X-ray bursts recur approximately every 9 hours, lasting about 1 hour, with X-ray count rates increasing by up to two orders of magnitude from a stable quiescent level. However, following the XMM6 observation, eruptions have not been detected in subsequent exposures from May 2020 to December 2021 (XMM7–XMM11). The QPE reappeared in XMM12 observation in July 2022 after disappearing for  $2.0 \pm 0.5$  years (Miniutti, G. et al. 2023b). The new light curve features differ markedly from the previous ones.

To estimate the MT rate in the QPE light curve, we use the model of light curve for the partial TDE from the tidal stripping proposed by Rees (1988); Ulmer (1999). The accretion luminosity of the stripped material falling back to the IMBH is  $L(t) = \tilde{\eta} \dot{M}_{\text{IMBH}}(t) c^2$ , where  $\tilde{\eta} = 0.1$  is the typical radiative efficiency (King 2020). The peak rate of mass gain of IMBH is  $\delta M_{\text{WD}}/3P_{\text{min}}$ , where  $P_{\text{min}}$  is the shortest Keplerian orbital period (Ulmer 1999; Wang et al. 2019). Thus, we can give a relationship between the peak of the light curve  $L_{\text{peak}}$  and the transferred mass per cycle  $\delta M_{\text{WD}}$  by the WD:

$$\delta M_{\text{WD}} \approx 2.5 \times 10^{-8} M_{\odot} \left( \frac{\eta}{0.1} \right)^{-1} \left( \frac{L_{\text{peak}}}{10^{42} \text{ erg s}^{-1}} \right) \left( \frac{P_{\text{min}}}{1 \text{ ks}} \right). \quad (60)$$

Based on the initial parameters provided in Sections 4 and 5, if  $\delta M_{\text{WD}}$  has the value given by Equation (60), the MT effect on the orbit becomes dominant over gravitational radiation ( $\delta M_{\text{WD}}$  exceeds the value indicated by the red points in the right panel of Figure 9).

In our model, when MT becomes dominant, the orbital period and eccentricity increase (Figure 8), and the WD finally escapes from the gravitational potential of the IMBH. The lifetime of the WD-IMBH system, when MT dominates, is much shorter than the gravitational radiation timescale, i.e.  $t_{\text{life}} \sim (1-e)/\langle \dot{e} \rangle_{\text{sec}} \ll t_{\text{GW}} \sim \left| (r_p - R_t) / \langle \dot{r}_{\text{pGW}} \rangle_{\text{sec}} \right|$  (Equations 55 and 56). Higher  $\xi_0$  results in higher transferred mass  $\delta M_{\text{WD}}$ , causing the WD to escape the system on a shorter timescale. The escape timescale is approximately 10 to  $10^2$  years.

In addition, the MT rate is highly sensitive to the pericenter distance. For this escape to occur, the initial pericenter distance must be sufficiently large to avoid tidal disruption, i.e.  $\epsilon_0 = 1 - r_p C_L / R_{\text{WD}} \ll \epsilon_1 \sim 1 - C_L q^{-1/3}$  (see Section 5.2 for details).

## 7.2 The assumptions for mass transfer

Equation (51) provides the MT rate when gravitational radiation and MT are in equilibrium. In this subsection, we will show that our MT rate is consistent with the estimates in King (2020, 2022), which use the gravitational radiation losses  $(J/J)_{\text{GW}}$  to drive the MT rate.

We reconsider the condition  $\langle \dot{R}_L / R_L - \dot{R}_{\text{WD}} / R_{\text{WD}} \rangle = 0$  in King (2022) and recalculate the expression using  $\epsilon = (R_{\text{WD}} - R_L) / R_{\text{WD}}$  and  $\epsilon = 1 - C_L r_p / R_{\text{WD}}$ :

$$\begin{aligned} \frac{\dot{R}_L}{R_L} - \frac{\dot{R}_{\text{WD}}}{R_{\text{WD}}} &= -\frac{\dot{\epsilon}}{1-\epsilon} = \frac{\dot{D}}{D} - \left( \frac{\dot{\epsilon}}{1-\epsilon} + \frac{\dot{r}_p}{r_p} \right) \\ &= \frac{\dot{D}}{D} - \frac{\dot{m}_1}{m_1} \left[ \frac{m_1}{R_{\text{WD}}} \frac{\partial R_{\text{WD}}}{\partial m_1} - \frac{q}{C_L} \frac{\partial C_L}{\partial q} (1 + \gamma q) \right]. \end{aligned} \quad (61)$$

Thus, we got the relationship between  $\dot{\epsilon}$  and  $\dot{r}_p$  from  $\dot{J}$ :

$$\frac{\dot{\epsilon}}{1-\epsilon} = \frac{\dot{m}_1}{m_1} \left[ \frac{\partial \ln R_{\text{WD}}}{\partial \ln m_1} - \frac{\partial \ln C_L}{\partial \ln q} (1 + \gamma q) \right] - \frac{\dot{r}_p}{r_p}, \quad (62a)$$

$$\frac{\dot{r}_p}{r_p} = -\frac{\dot{m}_1}{m_1} \frac{2(1-\gamma q^2) + q(1-\gamma)}{1+q} + \left( \frac{2\dot{J}}{J} - \frac{\dot{e}}{1+e} \right). \quad (62b)$$

If taking  $R_{\text{WD}} \propto m_1^{\zeta_1}$  and  $C_L \propto q^{\zeta_2}$ , we obtain  $\partial \ln R_{\text{WD}} / \partial \ln m_1 = \zeta_1$  and  $\partial \ln C_L / \partial \ln q = \zeta_2$ . Under the conditions  $M_{\text{WD}} \ll M_{\text{Ch}}$  and  $q \ll 1$ , we can assume  $\zeta_1 \rightarrow -1/3$  according to Equation (19) and  $\zeta_2 \rightarrow 1/3$  according to Equation (24). Thus, if we further take  $\gamma = 1$ , Equation (62a) reduces to Equation (12) in King (2022), which represents the conservation of mass.

According to King (2022, 2023), the dynamical stability of MT arises from the conservation of orbital angular momentum on a dynamical timescale, which is much shorter than that for gravitational radiation losses. The accretion disk reaches an effectively steady state

after a few orbital periods. After this, the disk passes almost all its angular momentum back to the orbit. This is the reabsorption of the original angular momentum of the mass transferred to the IMBH. As a result, conservation of orbital angular momentum forces the binary separation to increase, i.e.  $\langle \dot{a}_{\text{MT}}^{\text{B}} \rangle_{\text{sec}} > 0$ . Our analysis of orbital evolution builds upon the orbital angular momentum analysis from King (2022) and the eccentric orbital dynamics with MT from Sepinsky et al. (2007b). Finally, we present a new possible scenario for orbital evolution.

For showing the effect of gravitational radiation losses  $\dot{J}/J$  is to drive MT at a rate, the ratio  $R_{\text{WD}}/R_L$  remains unchanged in Equation (14) of King (2022), implying that setting  $\langle \dot{\epsilon}_{\text{MT}} \rangle_{\text{sec}} = 0$  in Equation (61). But this setting is not the only possible choice for orbital expansion (i.e., increases in semi-major axis, period, and eccentricity). Assuming orbital evolution starts from  $\epsilon_0 = 0$  (as shown in Figures 8, 9 and 10). The transferred mass per cycle  $|\delta M_{\text{WD}}|$  always increases, and the orbital period also increases due to MT dominance, the change of the period is faster than the change of  $|\delta M_{\text{WD}}|$  (When the eccentricity approaches 1, the period approaches infinity). The average MT rate  $|\delta M_{\text{WD}}/T|$  may reaches a maximum value and then decreases when the orbit expands. This reduction in average MT rate must require the MT process leading to orbit expansion.

Alternatively, the setting that the pericenter distance  $r_p$  remains unchanged, i.e.  $\langle \dot{r}_{\text{pMT}} \rangle_{\text{sec}} = 0$  in Equation (56), can also allow to orbital expansion. As shown in Section 3.3, the analysis of  $J_{\text{orb}}$  has given an expression for the component  $\mathcal{S}$  (Equation 38). From Equation (14) for  $\dot{p}$  and  $\dot{e}$ , the contribution of  $\mathcal{S}$  is much larger than that of  $\mathcal{R}$  at high eccentricity. Therefore, under different settings for component  $\mathcal{R}$ , the evolution of  $a$ ,  $T$  and  $e$  will not be different. They still evolve as shown in Figure 8.

We set  $\langle \dot{r}_{\text{pMT}} \rangle_{\text{sec}} = 0$  in this paper. For highly eccentric orbits, as discussed in Section 3.3, the acceleration  $f_{\text{MT}}^{\text{B}}$  is primarily significant near pericenter. Equation (39) shows that  $f_{\text{MT}}^{\text{B}}$  has almost no contribution to  $\langle \dot{r}_{\text{pMT}} \rangle_{\text{sec}}$ , taking  $\langle \dot{r}_{\text{pMT}} \rangle_{\text{sec}} = 0$  at high eccentricity more reasonable than  $\langle \dot{\epsilon}_{\text{MT}} \rangle_{\text{sec}} = 0$  in King (2022).

We can explain the orbital difference between the two settings. Setting Equation (62a) to zero corresponds to  $\langle \dot{\epsilon}_{\text{MT}} \rangle_{\text{sec}} = 0$ , while setting Equation (62b) to zero corresponds to  $\langle \dot{r}_{\text{pMT}} \rangle_{\text{sec}} = 0$ . However, only one of Equations (62a) or (62b) can be set to zero, since  $\dot{m}_1 \neq 0$  with MT. If  $\langle \dot{\epsilon}_{\text{MT}} \rangle_{\text{sec}} = 0$ , then  $\langle \dot{r}_{\text{pMT}} \rangle_{\text{sec}} > 0$ ; MT leads to an increase in the pericenter distance, the orbital pericenter decay caused by gravitational radiation will be slowed down significantly. Conversely, if  $\langle \dot{r}_{\text{pMT}} \rangle_{\text{sec}} = 0$ , then  $\langle \dot{\epsilon}_{\text{MT}} \rangle_{\text{sec}} > 0$ , we have discussed the evolution of  $\epsilon$  in this setting in Figure 10.

To drive the MT rate, we average  $\dot{J}_{\text{orb}}/J_{\text{orb}}$  in Equation (35) over one orbital period and apply Equation (48) to include  $\delta M_{\text{WD}}$ , accounting for gravitational radiation losses (Peters 1964):

$$\begin{aligned} \left\langle \frac{\dot{J}_{\text{orb}}}{J_{\text{orb}}} \right\rangle_{\text{MTsec}} &= \left( \frac{\delta M_{\text{WD}}}{M_{\text{WD}}} \right) \sqrt{\frac{GM_{\text{WD}}}{c^2 a_r}} \frac{1}{2\pi} \frac{c}{a_r} (1-q) \sqrt{\frac{1+q}{q}} \tilde{h}, \\ \left\langle \frac{\dot{J}_{\text{orb}}}{J_{\text{orb}}} \right\rangle_{\text{GWsec}} &= - \left( \frac{GM_{\text{WD}}}{c^2 a_r} \right)^3 \frac{32}{5} \frac{c}{a_r} \frac{1+q}{q^2} \frac{1 + \frac{7}{8} e_r^2}{(1 - e_r^2)^{5/2}}. \end{aligned} \quad (63)$$

Assuming  $\langle \dot{J}_{\text{orb}}/J_{\text{orb}} \rangle_{\text{MTsec}} \approx \langle \dot{J}_{\text{orb}}/J_{\text{orb}} \rangle_{\text{GWsec}}$ , we obtain:

$$\left( -\frac{\delta M_{\text{WD}}}{M_{\text{WD}}} \right) \approx \tilde{\lambda}^{-5/2} q \frac{64}{5} \pi \frac{1 + \frac{7}{8} e_r^2}{(1 + e_r)^{5/2}} \frac{\sqrt{1+q}}{(1-q)\tilde{h}}. \quad (64)$$

Here,  $|\delta M_{\text{WD}}/T|$  derived using this equation is the same as  $(-\dot{M}_2)$  in Equation (15) of King (2022). And Equation (64) is identical to Equation (51) for  $|\dot{a}_{\text{MT}}^{\text{B}}/\dot{a}_{\text{GW}}|_{\text{sec}} = 1$ . Therefore, the MT rate from

King (2022) is consistent with our view that gravitational radiation and MT are equilibrium.

### 7.3 Relativistic correction for the transferred mass

In Section 5.1.2, for Keplerian elliptical orbits, Equation (54) gives the transferred mass  $\delta M_{\text{WD}}$  during each orbital period. However, for high eccentricity ( $e_r \sim 0.99$ ) and small pericenter distance ( $\tilde{\lambda} = r_p / (Gm_2/c^2) \sim 8$ ), this result should be corrected to account for the effects due to general relativity.

Using post-Newtonian (PN) orbits, the  $\dot{f}_N$  in Equation (53) should be replaced by  $df/dt$  in Equation (14c). The effect of relativistic corrections is significant. When the companion star ( $q \ll 1$ ) has a high velocity near pericenter, the geodesic equation becomes more applicable. If we use geodesic equations in Schwarzschild spacetime instead, we can adopt  $dt/d\psi$  from Cutler et al. (1994); Martel (2004), to replace  $\dot{f}_N^{-1}$ . The final result for  $\delta M_{\text{WD}}$  is then given by

$$\delta M_{\text{WD}} \simeq \sum_{k=0}^{\infty} \left\{ F_k(\hat{p}) \cdot (1+e)^k \sqrt{1 + \frac{4(1-e^2)}{\hat{p}(\hat{p}-4)}} \times \right. \\ \left. \frac{4 C_{m_1} r_p^{3/2}}{\sqrt{Gm}} \sqrt{\frac{\epsilon}{2e}} \sum_{n=0}^{\infty} \sum_{m=0}^{\infty} C_{\epsilon n} \binom{n}{m} (-1)^m (1-\epsilon)^m \times \right. \\ \left. \text{AF1} \left[ \frac{1}{2}; \frac{1}{2}, m-k+2; \frac{3}{2}; \frac{1+e}{2e} \epsilon, \epsilon \right] \right\}, \quad (65)$$

where the series  $F_k(\hat{p})$  is derived in Appendix C. Here,  $\hat{p}$  satisfies  $p = \hat{p}(Gm/c^2) = r_p(1+e)$ , with  $e = (r_a - r_p)/(r_a + r_p)$ . The detailed derivation of Equation (65) is provided in Appendix C.

The relativistic correction to the Schwarzschild space-time geodesic introduces the coefficients  $F_k(\hat{p})(1+e)^k$  and  $1 + 4(1-e^2)/\hat{p}(\hat{p}-4)$ , which reduce to 1 in the 0PN limit. The coefficient  $F_k(\hat{p})(1+e)^k$  is positive for any  $k$ , and for  $0 < e < 1$ ,  $\hat{p} > 4$ , we have  $4(1-e^2)/\hat{p}(\hat{p}-4) > 0$ . These coefficients collectively enhance  $\delta M_{\text{WD}}$  compared to Equation (54), which is due to the orbital precession effect caused by general relativity. Since the orbital precession due to the Schwarzschild metric is prograde, the precession angle during one orbital period  $\Delta\varphi$  is positive. This positive  $\Delta\varphi$  increases the time interval during which  $R_{\text{WD}} > R_L$ , i.e.  $dt/d\psi > \dot{f}_N^{-1}$ . The expression for  $dt/d\psi$  is provided in Equation (C10). Because  $f_0$  satisfies  $R_{\text{WD}} = C_L D(f_0)$  and we substitute  $D$  with  $p/(1+e \cos \psi)$ , the value of  $f_0$  remains consistent with Equation (C9). The definite integral of  $dt/d\psi$  from  $-f_0$  to  $f_0$  must be greater than that of  $\dot{f}_N^{-1}$ .

As the eccentricity increases,  $dt/d\psi$  in Equation (C10) increases. For the case of  $m_1 = 0.15 M_{\odot}$ ,  $q = 3.75 \times 10^{-7}$ ,  $\epsilon = 5 \times 10^{-3}$  and  $e = 0.985$ , the relative difference in transferred mass is  $(\delta M_{\text{WD}}^{\text{R}} - \delta M_{\text{WD}}^{\text{NR}})/\delta M_{\text{WD}}^{\text{NR}} \simeq 65\%$ , where ‘‘NR’’ and ‘‘R’’ indicate non-relativistic and relativistic cases respectively.

The transferred mass  $\delta M_{\text{WD}}$  per cycle, as calculated from the series results (using Equation 65), is in good agreement with the results from the short-term evolution numerical simulations (Section 4), which directly use  $\dot{f}_{\text{MT}}^{\text{B}}$  from Equation (46) and  $\dot{m}_1$  from Equation (25). The deviation of  $\delta M_{\text{WD}}$  between these results is less than 5%.

### 7.4 Contribution of white dwarf spin angular momentum

Since  $q \ll 1$ , the orbital effects of the WD’s spin, arising from the spin acceleration terms  $\mathbf{a}_{\text{SO}}$ ,  $\mathbf{a}_{\text{SS}}$ , and  $\mathbf{a}_{\text{SOPN}}$ , are negligible. For  $\chi_1 \sim 0.1$  (the low spin parameter of WD is due to their structure being supported by electron degeneracy pressure; excessive rotation can cause centrifugal forces to exceed gravitational forces, leading

to instability or disintegration (Poisson & Will 2014)), the amplitude of the orbital changes is of the order of  $\chi_1 q$ .

In contrast, the MT effect on the variable  $A = \Omega_1^2 D^3 / G (m_1 + m_2)$  mentioned in Section 3.2 is more significant than the PN spin effect. The variable  $A$  is shown in Equation (21) for potential and Equation (32) for the Lagrange point L1. The two equations are used to derive  $\delta M_{\text{WD}}$ , they are both converted into the series of  $\delta M_{\text{WD}}$  in Equations (54) and (65). The effect of  $A$  can be illustrated by the coefficients of these series. We first estimate the size of  $A$  at pericenter:

$$A = \frac{\Omega_1^2 r_p^3}{Gm} = \left( \frac{R_{\text{WD}} \Omega_1}{c} \right)^2 \left( \frac{R_{\text{WD}}}{r_p} \right)^{-2} \left( \frac{Gm}{c^2 r_p} \right)^{-1} \quad (66) \\ = \frac{5}{4896} \frac{q}{1+q} \left( \frac{1-\epsilon}{C_L} \right)^3 \frac{M_{\text{WD}}^{4/3}}{M_{\odot} M_{\text{Ch}}^{1/3}} \left( \frac{\chi_1}{\tilde{\gamma}} \right)^2 = \frac{\varpi}{1+q} (1-\epsilon)^3,$$

where  $\varpi$  and  $\tilde{\gamma}$  are given in Equations (B10) and (B11).

For  $M_{\text{WD}} = 0.15 M_{\odot}$ ,  $q = 3.75 \times 10^{-7}$ ,  $\epsilon = 5 \times 10^{-3}$ ,  $\chi_1 = 0.1$ ,  $\tilde{\gamma} = 0.5$ , we find  $A = 1.86 \times 10^{-5} \gg \chi_1 q$ . For  $D_{\epsilon 1}$  in Equation (B14),  $\varpi C_L \sim 10^{-5} D_{\epsilon 1}$ , i.e.  $\varpi C_L / D_{\epsilon 1} \sim 10^{-5} \gg \chi_1 q \sim 10^{-8}$ . Therefore, we see that the orbital effect induced by the spin of the WD is much weaker than the effect due to MT. However,  $10^{-5} D_{\epsilon 1}$  is still very small compared to  $D_{\epsilon 1}$ , making it negligible.

## 8 CONCLUSION

In this paper, we introduced the orbital dynamics induced by the MT process, to study the orbital evolution of the high-eccentricity WD-IMBH system. The MT-induced acceleration  $\dot{f}_{\text{MT}}$  is given using the analysis of the time derivative of orbital angular momentum  $J_{\text{orb}}$  (Section 3.3). Orbital parameter variations are computed via the perturbed Kepler method, and the Roche lobe model is used to determine the MT rate  $\dot{M}_{\text{WD}}$ .

We relied on two key assumptions: 1. High initial eccentricity  $e_0 > 0.9$ . The relative acceleration due to  $\dot{f}_{\text{MT}}$  is significant only near pericenter, allowing the MT rate to be approximated by a delta function,  $\dot{M}_{\text{WD}} = M_0 \delta(f)$ . This approximation implies that MT does not directly affect the pericenter distance  $r_p$ , as shown in Equation (56). 2. The MT process is governed by the Roche lobe model. MT occurs primarily when the WD radius  $R_{\text{WD}}$  exceeds the Roche radius  $R_L$ , with their difference at pericenter being small ( $\epsilon = 1 - r_p C_L / R_{\text{WD}} \ll 1$ ). This small difference permits an expansion of the functional form of  $\dot{m}_1$ , enabling the transferred mass  $\delta M_{\text{WD}}$  to be derived using the Appell hypergeometric function (Appendix C).

We found that the effects of MT on the semi-major axis  $a$ , period  $T$ , and eccentricity  $e$  are counteracted by gravitational radiation. When MT and gravitational radiation on the semi-major axis  $a$  reach equilibrium, (i.e., the average change rate of  $a$  due to the two processes can cancel each other out), the transferred mass  $\delta M_{\text{WD}}$  per cycle in Equation (51) is very small, due to the high eccentricity of the orbit. The orbital parameters  $a$ ,  $T$  and  $e$  reach minimum values during evolution, as shown in Figure 8. When considering only MT and gravitational radiation, and the initial pericenter distance  $r_{p0}$  is far from the tidal radius  $R_t$ , the WD will escape the gravitational potential of the IMBH. Our findings on long-term evolution differ from those predicted in other models (Zalamea et al. 2010; King 2020, 2022; Wang et al. 2022).

The MT process may cause the WD to escape the gravitational influence of the IMBH, potentially explaining the disappearance of the QPE signal (Miniutti, G. et al. 2023b). Higher transferred mass  $\delta M_{\text{WD}}$  could lead to the WD leaving the system on a shorter

timescale. The transferred mass is highly sensitive to the differences between WD radius  $R_{\text{WD}}$  and Roche radius  $R_{\text{L}}$ . This may also influence estimates of the astronomical events rate involve MT.

For a 5-year GW observation, we compute the phase shift due to MT (Table 2), and the time at which  $a$  reaches its minimum (Table 3). When the initial orbital eccentricity is sufficiently small and the pericenter distance is large, there is a detectable phase shift.

Incorporating MT into GW signal parameter estimation enhances our understanding of the formation, evolution, and fate of EMRI systems. The MT model clarifies the interplay between orbital evolution driven by gravitational radiation and MT, provides more accurate physical input for binary systems, and improves the precision of GW parameter estimates. We can gain a clearer understanding of how orbital evolution caused by gravitational radiation and MT contribute to each other. To maximize scientific returns, WD-IMBH systems should be observed via both electromagnetic and gravitational channels. Timely alerts from LISA and other space-based GW detectors to electromagnetic observatories are essential for this purpose (Sesana et al. 2008; Holley-Bockelmann et al. 2020; Torres-Orjuela et al. 2024; Li et al. 2024).

## ACKNOWLEDGEMENTS

We appreciate Yucheng Yin and Han Yan for many useful discussions. J.Y. is supported by the National Key Research and Development Program of China (grant No. 2021YFC2203003), the National Natural Science Foundation of China (grant No. 12247101), and the “111 Center” under grant No. B20063. X.C. is supported by the Natural Science Foundation of China (grant No. 12473037).

## DATA AVAILABILITY

The data underlying this article will be shared on reasonable request to the corresponding author.

## REFERENCES

- Amaro-Seoane P., 2018, *Living Reviews in Relativity*, 21, 4  
 Amaro-Seoane P., Gair J. R., Freitag M., Miller M. C., Mandel I., Cutler C. J., Babak S., 2007, *Classical and Quantum Gravity*, 24, R113  
 Amaro-Seoane P., et al., 2017, *Laser Interferometer Space Antenna* (arXiv:1702.00786), <https://arxiv.org/abs/1702.00786>  
 Arcodia, R. et al., 2022, *A&A*, 662, A49  
 Arcodia, R. et al., 2024, *A&A*, 690, A80  
 Arcodia R., et al., 2021, *Nature*, 592, 704  
 Barack L., Cutler C., 2004, *Phys. Rev. D*, 69, 082005  
 Barsanti S., et al., 2024  
 Berry C. P. L., Gair J. R., 2012, *Extreme-mass-ratio bursts from the Galactic Centre* (arXiv:1209.5731), <https://arxiv.org/abs/1209.5731>  
 Blanchet L., 2014, *Living Reviews in Relativity*, 17, 2  
 Blanchet L., 2024, *Living Reviews in Relativity*, 27, 4  
 Blanchet L., Faye G., Ponsot B., 1998, *Phys. Rev. D*, 58, 124002  
 Bogdanović T., Cheng R. M., Amaro-Seoane P., 2014, *The Astrophysical Journal*, 788, 99  
 Cehula J., Pejcha O., 2023b, *MNRAS*, 524, 471  
 Cehula J., Pejcha O., 2023a, *Monthly Notices of the Royal Astronomical Society*, 524, 471  
 Chakraborty J., Kara E., Masterson M., Giustini M., Miniutti G., Saxton R., 2021, *The Astrophysical Journal Letters*, 921, L40  
 Chakraborty J., et al., 2024, *The Astrophysical Journal*, 965, 12  
 Chen X., Qiu Y., Li S., Liu F. K., 2022, *The Astrophysical Journal*, 930, 122  
 Cutler C., Kennefick D., Poisson E., 1994, *Phys. Rev. D*, 50, 3816

- Danby J., 1962, *Fundamentals of Celestial Mechanics*. Macmillan, <https://books.google.com.hk/books?id=N5h-AAAAIAAJ>  
 Derdzinski A. M., D’Orazio D., Duffell P., Haiman Z., MacFadyen A., 2019, *Monthly Notices of the Royal Astronomical Society*, 486, 2754  
 Dosopoulou F., Kalogera V., 2016, *The Astrophysical Journal*, 825, 70  
 Efroimsky M., 2002, *Equations for the Keplerian Elements: Hidden Symmetry*, Preprint No 1844 of the IMA (Institute of Applied Mathematics and its Applications), University of Minnesota  
 Efroimsky M., 2005, *Annals of the New York Academy of Sciences*, 1065, 346  
 Efroimsky M., Goldreich P., 2003, *Journal of Mathematical Physics*, 44, 5958  
 Efroimsky, M. Goldreich, P. 2004, *A&A*, 415, 1187  
 Fitzpatrick P., 1970, *Principles of Celestial Mechanics*. Academic Press, <https://books.google.com.hk/books?id=GJd-AAAAIAAJ>  
 Fitzpatrick R., 2012, *An Introduction to Celestial Mechanics*. Cambridge University Press, <https://books.google.com.hk/books?id=zwcxgyYCG5QC>  
 Franchini, Alessia et al., 2023, *A&A*, 675, A100  
 Freitag M., 2001, *Classical and Quantum Gravity*, 18, 4033  
 Fujita R., Hikida W., 2009, *Classical and Quantum Gravity*, 26, 135002  
 Gair J. R., 2009, *Classical and Quantum Gravity*, 26, 094034  
 Gair J. R., Babak S., Sesana A., Amaro-Seoane P., Barausse E., Berry C. P. L., Berti E., Sopuerta C., 2017, *Journal of Physics: Conference Series*, 840, 012021  
 Garain D., Sarkar T., 2024, *Partial tidal disruptions of spinning eccentric white dwarfs by spinning intermediate mass black holes* (arXiv:2401.17031), <https://arxiv.org/abs/2401.17031>  
 Giustini, Margherita Miniutti, Giovanni Saxton, Richard D. 2020, *A&A*, 636, L2  
 Giustini, Margherita et al., 2024, *A&A*, 692, A15  
 Hils D., Bender P. L., 1995, *ApJ*, 445, L7  
 Holley-Bockelmann K., et al., 2020, *Getting Ready for LISA: The Data, Support and Preparation Needed to Maximize US Participation in Space-Based Gravitational Wave Science* (arXiv:2012.02650), <https://arxiv.org/abs/2012.02650>  
 Hughes S. A., Warburton N., Khanna G., Chua A. J. K., Katz M. L., 2021, *Phys. Rev. D*, 103, 104014  
 Ivanov, P. B. Papaloizou, J. C. B. 2007, *A&A*, 476, 121  
 Jackson B., Arras P., Penev K., Peacock S., Marchant P., 2017, *The Astrophysical Journal*, 835, 145  
 King A., 2020, *Monthly Notices of the Royal Astronomical Society: Letters*, 493, L120  
 King A., 2022, *Monthly Notices of the Royal Astronomical Society*, 515, 4344  
 King A., 2023, *Monthly Notices of the Royal Astronomical Society: Letters*, 520, L63  
 Kocsis B., Yunes N., Loeb A., 2011, *Phys. Rev. D*, 84, 024032  
 Kolb U., Ritter H., 1990, *A&A*, 236, 385  
 Krolik J. H., Linial I., 2022, *The Astrophysical Journal*, 941, 24  
 Landau L., 2013, *The Classical Theory of Fields. COURSE OF THEORETICAL PHYSICS*, Elsevier Science, <https://books.google.com.hk/books?id=HudbAWAAQBAJ>  
 Li E.-K., et al., 2024, *Gravitational Wave Astronomy With TianQin* (arXiv:2409.19665), <https://arxiv.org/abs/2409.19665>  
 Linial I., Sari R., 2023, *The Astrophysical Journal*, 945, 86  
 Lu W., Quataert E., 2023, *Monthly Notices of the Royal Astronomical Society*, 524, 6247  
 Lubow S. H., Shu F. H., 1975a, *ApJ*, 198, 383  
 Lubow S. H., Shu F. H., 1975b, *ApJ*, 198, 383  
 Luminet J. P., Pichon B., 1989, *A&A*, 209, 103  
 Marchant, Pablo Pappas, Kaliroë M. W. Gallegos-Garcia, Monica Berry, Christopher P. L. Taam, Ronald E. Kalogera, Vicky Podsiadlowski, Philipp 2021, *A&A*, 650, A107  
 Martel K., 2004, *Phys. Rev. D*, 69, 044025  
 McCart J., Osburn T., Burton J. Y. J., 2021, *Phys. Rev. D*, 104, 084050  
 Menou K., Haiman Z., Kocsis B., 2008, *New Astronomy Reviews*, 51, 884  
 Miniutti, G. Giustini, M. Arcodia, R. Saxton, R. D. Read, A. M. Bianchi, S. Alexander, K. D. 2023a, *A&A*, 670, A93

- Miniutti, G. Giustini, M. Arcodia, R. Saxton, R. D. Chakraborty, J. Read, A. M. Kara, E. 2023b, *A&A*, 674, L1
- Miniutti, G. et al., 2025, *A&A*, 693, A179
- Miniutti G., et al., 2019, *Nature*, 573, 381
- Murray C., Dermott S., 1999, *Solar System Dynamics*. Cambridge University Press, <https://books.google.com.hk/books?id=aU6vcy5L8GAC>
- Olver F., Lozier D., Boisvert R., Clark C., 2010, *The NIST Handbook of Mathematical Functions*. Cambridge University Press, New York, NY
- Pavlovskii K., Ivanova N., 2015, *Monthly Notices of the Royal Astronomical Society*, 449, 4415
- Peters P. C., 1964, *Phys. Rev.*, 136, B1224
- Poisson E., Will C., 2014, *Gravity: Newtonian, Post-Newtonian, Relativistic*. Cambridge University Press, <https://books.google.com.hk/books?id=PZ5cAwAAQBAJ>
- Rees M. J., 1988, *Nature*, 333, 523
- Ritter H., 1988, *A&A*, 202, 93
- Schmidt W., 2002, *Classical and Quantum Gravity*, 19, 2743
- Sepinsky J. F., Willems B., Kalogera V., 2007a, *The Astrophysical Journal*, 660, 1624
- Sepinsky J. F., Kalogera B., Willems V., Rasio F. A., 2007b, *The Astrophysical Journal*, 667, 1170
- Sesana A., Vecchio A., Eracleous M., Sigurdsson S., 2008, *Monthly Notices of the Royal Astronomical Society*, 391, 718
- Seymour P. A. H., 1984, *Physics Bulletin*, 35, 73
- Speri L., 2024, PhD thesis, Humboldt University of Berlin, Mathematisch-Naturwissenschaftliche Fakultät, [doi:http://dx.doi.org/10.18452/29058](http://dx.doi.org/10.18452/29058)
- Sterne T., 1960, *An Introduction to Celestial Mechanics*. Interscience tracts on physics and astronomy, Interscience Publishers, <https://books.google.com.hk/books?id=MXLvAAAAAAAJ>
- Tagoshi H., Ohashi A., Owen B. J., 2001, *Phys. Rev. D*, 63, 044006
- Torres-Orjuela A., et al., 2024, GWnext 2024: Meeting Summary ([arXiv:2406.03498](https://arxiv.org/abs/2406.03498)), <https://arxiv.org/abs/2406.03498>
- Ulmer A., 1999, *The Astrophysical Journal*, 514, 180
- Wang Y. Y., Wang F. Y., Zou Y. C., Dai Z. G., 2019, *The Astrophysical Journal Letters*, 886, L22
- Wang M., Yin J., Ma Y., Wu Q., 2022, *The Astrophysical Journal*, 933, 225
- Xian J., Zhang F., Dou L., He J., Shu X., 2021, *The Astrophysical Journal Letters*, 921, L32
- Zalamea I., Menou K., Beloborodov A. M., 2010, *Monthly Notices of the Royal Astronomical Society: Letters*, 409, L25
- Zhang Z.-H., Liu T., Yu S., Guo Z.-K., 2024a, Gravitational wave signatures and detectability of the mass transfer effect in compact binaries ([arXiv:2409.04020](https://arxiv.org/abs/2409.04020)), <https://arxiv.org/abs/2409.04020>
- Zhang Z.-h., Liu B., Yu S.-h., Yang J., 2024b, *Phys. Rev. D*, 109, 123013
- Zhao, Z. Y. Wang, Y. Y. Zou, Y. C. Wang, F. Y. Dai, Z. G. 2022, *A&A*, 661, A55
- Zhou C., Huang L., Guo K., Li Y.-P., Pan Z., 2024a, *Phys. Rev. D*, 109, 103031
- Zhou C., Huang L., Guo K., Li Y.-P., Pan Z., 2024b, *Phys. Rev. D*, 109, 103031
- Zhou C., Zhong B., Zeng Y., Huang L., Pan Z., 2024c, *Phys. Rev. D*, 110, 083019
- Zwick L., Derdzinski A., Garg M., Capelo P. R., Mayer L., 2022, *Monthly Notices of the Royal Astronomical Society*, 511, 6143

## APPENDIX A: A SHORT REVIEW OF THE PERTURBED KEPLER METHOD

The literature on the Perturbed Kepler Method is extensive (Sterne 1960; Danby 1962; Fitzpatrick 1970; Efroimsky 2002; Efroimsky & Goldreich 2003; Efroimsky, M. & Goldreich, P. 2004; Fitzpatrick 2012; Poisson & Will 2014; Dosopoulou & Kalogera 2016). Here, we provide a brief overview of the formalism (Poisson & Will 2014), focusing on approaches that do not employ Lagrangian or Hamiltonian mechanics.

Returning to Equation (13), the first time derivative of  $\mathbf{r}$  and  $\mathbf{v}$  are:

$$\frac{d\mathbf{r}}{dt} = \frac{\partial \mathbf{r}_{\text{Kepler}}}{\partial f} \frac{df}{dt} + \sum_a \frac{\partial \mathbf{r}_{\text{Kepler}}}{\partial \mu^a} \frac{d\mu^a}{dt} = \mathbf{v}_{\text{Kepler}}(f(t), \mu^a(t)),$$

$$\frac{d\mathbf{v}}{dt} = \frac{\partial \mathbf{v}_{\text{Kepler}}}{\partial f} \frac{df}{dt} + \sum_a \frac{\partial \mathbf{v}_{\text{Kepler}}}{\partial \mu^a} \frac{d\mu^a}{dt} = \mathbf{a}.$$

From the Equation (12), we further obtain:

$$\frac{\partial \mathbf{r}_{\text{Kepler}}}{\partial f} \left( \frac{df}{dt} - \dot{f}_N \right) + \sum_a \frac{\partial \mathbf{r}_{\text{Kepler}}}{\partial \mu^a} \frac{d\mu^a}{dt} = \mathbf{0},$$

$$\frac{\partial \mathbf{v}_{\text{Kepler}}}{\partial f} \left( \frac{df}{dt} - \dot{f}_N \right) + \sum_a \frac{\partial \mathbf{v}_{\text{Kepler}}}{\partial \mu^a} \frac{d\mu^a}{dt} = \mathbf{f},$$

where  $\dot{f}_N$  is defined as in Equation (17). The six equations describe the time evolution of six unknown functions ( $f, p, e, \omega, \Omega, i$ ). From a mathematical perspective, each of these functions has solution. However, solving the equations directly is complex and challenging (Dosopoulou & Kalogera 2016). This complexity is due to the fact that these equations are not expressed in a convenient form, and must require Equation (9).

The vectors  $\mathbf{r}_{\text{Kepler}}$  and  $\mathbf{v}_{\text{Kepler}}$  are not conserved quantities in a classical Kepler orbit. However, they can be combined by various conserved quantities, such as orbital energy  $E$  and orbital angular momentum  $\mathbf{J}_{\text{orb}}$ . They can yield additional conserved quantities, the orbital period  $T$  and the Laplace–Runge–Lenz (LRL) vector  $\mathbf{A}$ . By defining an orthogonal frame  $(x, y, z)$  with basis vectors  $\mathbf{e}_x, \mathbf{e}_y, \mathbf{e}_z$ , where the origin is at  $m_2$ , we align the  $\mathbf{e}_x$  with the pericenter and set  $\mathbf{e}_z$  perpendicular to the  $xy$ -plane. In this frame,  $\dot{\mathbf{e}}_x = \dot{\mathbf{e}}_y = \dot{\mathbf{e}}_z = \mathbf{0}$  in a classical Kepler orbit. These conserved quantities allow us to readily derive the  $df/dt$  and  $d\mu^a/dt$ .

We define the energy per unit reduced mass  $\mathcal{E}$ , the orbital angular momentum per unit reduced mass  $\mathbf{h}$  and the LRL vector  $\mathbf{A}$  as follows:

$$\mathcal{E} = \frac{E}{\mu} = \frac{v^2}{2} - \frac{Gm}{r}, \quad \mathbf{h} = \frac{\mathbf{J}_{\text{orb}}}{\mu} = \mathbf{r} \times \mathbf{v}, \quad \mathbf{A} = \frac{\mathbf{v} \times \mathbf{h}}{Gm} - \frac{\mathbf{r}}{r}. \quad (\text{A1})$$

For Newtonian gravity, we have the following orbital representation:

$$r = \frac{h^2/Gm}{1 + \sqrt{1 + \frac{2\mathcal{E}h^2}{G^2m^2}} \cos f}, \quad (\text{A2})$$

where we can define semi-latus rectum  $p$  and eccentricity  $e$ ,

$$p = \frac{h^2}{Gm}, \quad e = \sqrt{1 + \frac{2\mathcal{E}h^2}{G^2m^2}}, \quad r = \frac{p}{1 + e \cos f}. \quad (\text{A3})$$

We get  $\mathcal{E}$  using the velocity expression  $v^2 = \dot{r}^2 + (h/r)^2$ :

$$\mathcal{E} = \frac{\dot{r}^2}{2} + \frac{h^2}{2r^2} - \frac{Gm}{r}. \quad (\text{A4})$$

Therefore, we obtain  $dr/dt$  using Equations (A3) and (A4):

$$\dot{r} = \sqrt{\frac{Gm}{p}} e \sin f. \quad (\text{A5})$$

According to the perturbation theory, the expression of velocity  $\mathbf{v}$  remains consistent with Kepler's original form  $\mathbf{v}_{\text{Kepler}}$ :

$$\mathbf{v} = \mathbf{v}_{\text{Kepler}}(f(t), \mu^a(t)) = \frac{d}{dt}(\mathbf{r}\mathbf{n}) = \dot{r}\mathbf{n} + r\dot{f}_N\boldsymbol{\lambda}, \quad (\text{A6})$$

Thus, with  $\mathbf{r} = r\mathbf{n}$ , we give the time derivative  $d\mathbf{n}/dt$ :

$$\frac{d\mathbf{n}}{dt} = \dot{f}_N\boldsymbol{\lambda}. \quad (\text{A7})$$

Substituting  $\mathbf{v}$  into  $\mathbf{h}$  in Equation (A1), and using Equation (A3), we obtain

$$\mathbf{h} = r^2 \dot{f}_N \boldsymbol{\ell}, \quad \dot{f}_N = \frac{\mathbf{h} \cdot \boldsymbol{\ell}}{r^2} = \sqrt{\frac{Gm}{p^3}} (1 + e \cos f)^2. \quad (\text{A8})$$

This is consistent with Equation (17). In addition, the vectors  $\mathbf{n}$ ,  $\boldsymbol{\lambda}$ ,  $\boldsymbol{\ell}$  can be expressed in terms of the vectors  $\mathbf{e}_x$ ,  $\mathbf{e}_y$ ,  $\mathbf{e}_z$ ,

$$\begin{bmatrix} \mathbf{n} \\ \boldsymbol{\lambda} \\ \boldsymbol{\ell} \end{bmatrix} = \begin{bmatrix} \cos f & \sin f & 0 \\ -\sin f & \cos f & 0 \\ 0 & 0 & 1 \end{bmatrix} \begin{bmatrix} \mathbf{e}_x \\ \mathbf{e}_y \\ \mathbf{e}_z \end{bmatrix}. \quad (\text{A9})$$

Due to the orthogonality of  $(\mathbf{n}, \boldsymbol{\lambda}, \boldsymbol{\ell})$  and  $(\mathbf{e}_x, \mathbf{e}_y, \mathbf{e}_z)$ , we can get

$$\langle \mathbf{n}, \dot{\mathbf{n}} \rangle = \langle \boldsymbol{\lambda}, \dot{\boldsymbol{\lambda}} \rangle = \langle \boldsymbol{\ell}, \dot{\boldsymbol{\ell}} \rangle \equiv 0, \quad (\text{A10a})$$

$$\langle \mathbf{e}_x, \dot{\mathbf{e}}_x \rangle = \langle \mathbf{e}_y, \dot{\mathbf{e}}_y \rangle = \langle \mathbf{e}_z, \dot{\mathbf{e}}_z \rangle \equiv 0. \quad (\text{A10b})$$

The LRL vector  $\mathbf{A}$  is a eccentricity vector defined by  $\mathbf{r}$  and  $\mathbf{v}$ :

$$\begin{aligned} \mathbf{A} &= \frac{\mathbf{v} \times \mathbf{h}}{Gm} - \frac{\mathbf{r}}{r} = \left( \frac{v^2}{Gm} - \frac{1}{r} \right) \mathbf{r} - \frac{\mathbf{r} \cdot \mathbf{v}}{Gm} \mathbf{v} \\ &= \left( \frac{r^3 \dot{f}_N^2}{Gm} - 1 \right) \mathbf{n} - \frac{r^2 \dot{f}_N}{Gm} \boldsymbol{\lambda} = e (\cos f \mathbf{n} - \sin f \boldsymbol{\lambda}) = e \mathbf{e}_x. \end{aligned} \quad (\text{A11})$$

Therefore, we can establish the relationship between orbital parameters  $f$ ,  $p$ ,  $e$ ,  $\omega$ ,  $\Omega$ ,  $\iota$ , and the conserved quantities  $\mathbf{h}$ ,  $\mathbf{A}$ ,  $\mathbf{e}_x$ ,  $\mathbf{e}_y$ ,  $\mathbf{e}_z$  as follows:

$$\begin{aligned} p &:= \frac{h^2}{Gm}, \quad \cos f := \mathbf{n} \cdot \mathbf{e}_x, \quad \sin \iota \sin \Omega := \mathbf{e}_z \cdot \mathbf{e}_x, \\ e &:= A, \quad \cos \iota := \mathbf{e}_z \cdot \mathbf{e}_z, \quad \sin \iota \sin \omega := \mathbf{e}_x \cdot \mathbf{e}_z. \end{aligned} \quad (\text{A12})$$

Taking the time derivative on both sides of the equations, we get

$$\begin{aligned} \dot{e} &= \dot{A}, \quad \dot{f} = -\frac{\dot{\mathbf{n}} \cdot \mathbf{e}_x + \mathbf{n} \cdot \dot{\mathbf{e}}_x}{\sin f}, \quad \dot{\omega} = \frac{(\dot{\mathbf{e}}_x + \cot \iota \sin \omega \dot{\mathbf{e}}_z) \cdot \mathbf{e}_z}{\sin \iota \cos \omega}, \\ \dot{p} &= \frac{2h}{Gm} \dot{h}, \quad \dot{i} = -\frac{\dot{\mathbf{e}}_z \cdot \mathbf{e}_z}{\sin \iota}, \quad \dot{\Omega} = \frac{\dot{\mathbf{e}}_z \cdot (\mathbf{e}_x + \cot \iota \sin \Omega \mathbf{e}_z)}{\sin \iota \cos \Omega}. \end{aligned} \quad (\text{A13})$$

Therefore, we now need to relate the external force  $\mathbf{f}$  to  $\dot{\mathbf{h}}$ ,  $\dot{A}$ ,  $\dot{h}$ ,  $\dot{A}$ ,  $\dot{\mathbf{e}}_z$ ,  $\dot{\mathbf{e}}_x$ . The form of  $\mathbf{f}$  is given in Equation (6). We can calculate  $\dot{\mathbf{h}}$  and  $\dot{A}$  using Equation (A1):

$$\frac{d\mathbf{h}}{dt} = \frac{d\mathbf{r}}{dt} \times \mathbf{v} + \mathbf{r} \times \frac{d\mathbf{v}}{dt} = \mathbf{r} \times \mathbf{a} = \mathbf{r} \times \mathbf{f} = -r (\mathcal{S}\boldsymbol{\ell} - \mathcal{W}\boldsymbol{\lambda}), \quad (\text{A14a})$$

$$\begin{aligned} \frac{d\mathbf{A}}{dt} &= \frac{\mathbf{a} \times (\mathbf{r} \times \mathbf{v}) + \mathbf{v} \times (\mathbf{r} \times \mathbf{a})}{Gm} - \left( \frac{\mathbf{v}}{r} - \frac{\dot{r}}{r^2} \mathbf{r} \right) \\ &= \frac{\mathbf{f} \times \mathbf{h} + \mathbf{v} \times (\mathbf{r} \times \mathbf{f})}{Gm} \\ &= \frac{1}{Gm} [2h\mathcal{S}\mathbf{n} - (h\mathcal{R} + r\dot{r}\mathcal{S})\boldsymbol{\lambda} - r\dot{r}\mathcal{W}\boldsymbol{\ell}] \\ &= \frac{1}{Gm} \{ [2h\mathcal{S} \cos f + (h\mathcal{R} + r\dot{r}\mathcal{S}) \sin f] \mathbf{e}_x \\ &\quad + [2h\mathcal{S} \sin f - (h\mathcal{R} + r\dot{r}\mathcal{S}) \cos f] \mathbf{e}_y - r\dot{r}\mathcal{W}\mathbf{e}_z \}. \end{aligned} \quad (\text{A14b})$$

We then calculate  $\dot{h}$  and  $\dot{A}$  using Equations (A8), (A11) and (A14), along with the orthogonality condition (A10):

$$\frac{dh}{dt} = \frac{d\mathbf{h}}{dt} \cdot \boldsymbol{\ell} + \mathbf{h} \cdot \frac{d\boldsymbol{\ell}}{dt} = \frac{d\mathbf{h}}{dt} \cdot \boldsymbol{\ell} = r\mathcal{S}, \quad (\text{A15a})$$

$$\begin{aligned} \frac{dA}{dt} &= \frac{d\mathbf{A}}{dt} \cdot \mathbf{e}_x + \mathbf{A} \cdot \frac{d\mathbf{e}_x}{dt} = \frac{d\mathbf{A}}{dt} \cdot \mathbf{e}_x \\ &= \frac{1}{Gm} [2h\mathcal{S} \cos f + (h\mathcal{R} + r\dot{r}\mathcal{S}) \sin f]. \end{aligned} \quad (\text{A15b})$$

And calculate  $\dot{e}_z = d\ell/dt$  (Equation A9) and  $\dot{e}_x$  using Equations (A14) and (A15):

$$\frac{de_z}{dt} = \frac{1}{h} \left( \frac{dh}{dt} - \frac{dh}{dt} \mathbf{e}_z \right) = -\frac{r\mathcal{W}}{h} \boldsymbol{\lambda}, \quad (\text{A16a})$$

$$\begin{aligned} \frac{de_x}{dt} &= \frac{1}{A} \left( \frac{d\mathbf{A}}{dt} - \frac{d\mathbf{A}}{dt} \mathbf{e}_x \right) = \frac{1}{GmA} \times \\ &\quad \{ [2h\mathcal{S} \sin f - (h\mathcal{R} + r\dot{r}\mathcal{S}) \cos f] \mathbf{e}_y - r\dot{r}\mathcal{W}\mathbf{e}_z \}. \end{aligned} \quad (\text{A16b})$$

Therefore, the Equation (A13) change to

$$\dot{p} = \frac{2h}{Gm} r\mathcal{S}, \quad (\text{A17a})$$

$$\dot{e} = \frac{h}{Gm} \left[ \sin f \mathcal{R} + \left( 2 \cos f + \frac{r\dot{r}}{h} \sin f \right) \mathcal{S} \right], \quad (\text{A17b})$$

$$\dot{f} = \frac{h}{r^2} + \frac{h}{GmA} \left[ \cos f \mathcal{R} - \left( 2 \sin f - \frac{r\dot{r}}{h} \cos f \right) \mathcal{S} \right], \quad (\text{A17c})$$

$$\dot{i} = \frac{r}{h} \cos(\omega + f) \mathcal{W}, \quad (\text{A17d})$$

$$\dot{\Omega} = \frac{r}{h} \sin(\omega + f) \csc \iota \mathcal{W}, \quad (\text{A17e})$$

$$\begin{aligned} \dot{\omega} &= \frac{h}{GmA} \left[ -\cos f \mathcal{R} + \left( 2 \sin f - \frac{r\dot{r}}{h} \cos f \right) \mathcal{S} \right. \\ &\quad \left. - e \cot \iota \frac{Gmr}{h^2} \left( \frac{h\dot{r} \sec \omega}{GmA} + \tan \omega \cos(\omega + f) \right) \mathcal{W} \right]. \end{aligned} \quad (\text{A17f})$$

From Equations (A7) and (A16), we obtain  $d\mathbf{n}/dt$  and  $d\boldsymbol{\ell}/dt$ . We can also get  $d\boldsymbol{\lambda}/dt$  in terms of  $\mathbf{e}_x = \cos f \mathbf{n} - \sin f \boldsymbol{\lambda}$  (Equation A9), using  $\dot{e}_x$  (A16b),  $\dot{\mathbf{n}}$  (A7) and  $\dot{f}$  (A17c):

$$\begin{aligned} \frac{d\boldsymbol{\lambda}}{dt} &= -\frac{\dot{e}_x + \dot{f} (\sin f \mathbf{n} + \cos f \boldsymbol{\lambda}) - \cos f \dot{\mathbf{n}}}{\sin f} \\ &= -\dot{f}_N \mathbf{n} + \frac{r\dot{r}\mathcal{W}}{GmA} \csc f \boldsymbol{\ell}. \end{aligned} \quad (\text{A18})$$

We obtain the final form in Equations (14) and (15) by substituting the following expressions into Equations (A17), (A7), (A18) and (A16):

$$r = \frac{p}{1 + e \cos f}, \quad \dot{r} = \sqrt{\frac{Gm}{p}} e \sin f, \quad (\text{A19})$$

$$\dot{f}_N = \sqrt{\frac{Gm}{p^3}} (1 + e \cos f)^2, \quad h = \sqrt{Gmp}, \quad A = e.$$

## APPENDIX B: SIMPLIFICATION OF THE MASS TRANSFER MODEL

In this appendix, we simplify Equation (25) by considering only the adiabatic process of Roche-lobe overflow. This reduces Equation (25) to Equation (27). We can cancel the first and third terms in Equation (27), because  $\rho_1 \gg \rho_{\text{ph}}$  and  $K^{1/\Gamma} / e \sim F(K, \Gamma)^2$  for  $\Gamma = 5/3$ . We get

$$\dot{m}_1 = -H(\varepsilon) \frac{2\pi}{\sqrt{BC}} F(K, \Gamma) K^{\frac{3\Gamma-1}{2\Gamma}} \rho_1^{\frac{3\Gamma-1}{2}}, \quad (\text{B1})$$

where  $\rho_1$  can be given in Equation (21), and  $2\pi/\sqrt{BC}$  can be written in series form:

$$\begin{aligned} \frac{2\pi}{\sqrt{BC}} &= \frac{2\pi D^3}{Gm_2} \frac{1}{\sqrt{\mathcal{R} [\mathcal{R} - A(1+q)]}}, \\ &= \frac{1}{\sqrt{\mathcal{R} [\mathcal{R} - A(1+q)]}} := \frac{1}{\sqrt{\mathcal{R}_0}} \left( \sum_{m=0}^{\infty} S_m \varepsilon^m \right). \end{aligned} \quad (\text{B2})$$

Equation (21) can be organized into the following form:

$$\rho_1^{\frac{3\Gamma-1}{2}} = \left( \frac{\Gamma-1}{K\Gamma} \frac{Gm_2}{D} C_L \right)^{\frac{3\Gamma-1}{2(\Gamma-1)}} \left( \hat{\rho}_{\text{ph}}^{\Gamma-1} + \lambda \right)^{\frac{3\Gamma-1}{2(\Gamma-1)}}, \quad (\text{B3})$$

where  $\lambda := \lambda_1 + \lambda_O := \sum_{n=1}^{\infty} D_{\varepsilon n} \varepsilon^n$ , specifically  $\lambda_1 = D_{\varepsilon 1} \varepsilon$ . From Equation (22), the  $\hat{\rho}_{\text{ph}}^{\Gamma-1}$  can be defined as

$$\hat{\rho}_{\text{ph}}^{\Gamma-1} := \left( \frac{\Gamma-1}{K\Gamma} \frac{Gm_2}{D} C_L \right)^{-1} \rho_{\text{ph}}^{\Gamma-1} = \frac{q}{C_L^2} \frac{\xi_0}{1-\xi_0} (1-\varepsilon). \quad (\text{B4})$$

Define  $\alpha$  to re-express the variable  $\hat{\rho}_{\text{ph}}^{\Gamma-1}$ ,

$$\frac{q}{C_L^2} \frac{\xi_0}{1-\xi_0} := \frac{D_{\varepsilon 1}}{1-\alpha}, \quad \text{where } \alpha := 1 - \left( \frac{q}{C_L^2} \frac{\xi_0}{1-\xi_0} \right)^{-1} D_{\varepsilon 1}. \quad (\text{B5})$$

We can assume that  $\lambda_1 + \hat{\rho}_{\text{ph}}^{\Gamma-1} \gg \lambda_O$  near pericenter. Let us define a new series to represent  $\hat{\rho}_{\text{ph}}^{\Gamma-1} + \lambda$ ,

$$\left( \lambda_1 + \hat{\rho}_{\text{ph}}^{\Gamma-1} + \lambda_O \right)^{\frac{3\Gamma-1}{2(\Gamma-1)}} := \left( \sum_{n=0}^{\infty} \mathcal{U}_{\varepsilon n} \varepsilon^n \right). \quad (\text{B6})$$

We can take a first-order expand with respect to  $\lambda_O$ :

$$\left( \sum_{n=1}^{\infty} \mathcal{U}_{\varepsilon n} \varepsilon^n \right) \simeq \left( D_{\varepsilon 1} \frac{1-\alpha\varepsilon}{1-\alpha} \right)^{\frac{3\Gamma-1}{2(\Gamma-1)}} \left( 1 + \frac{3\Gamma-1}{2(\Gamma-1)} \frac{\lambda_O}{\lambda_1 + \hat{\rho}_{\text{ph}}^{\Gamma-1}} \right),$$

$$\frac{\lambda_O}{\lambda_1 + \hat{\rho}_{\text{ph}}^{\Gamma-1}} = \left( D_{\varepsilon 1} \frac{1-\alpha\varepsilon}{1-\alpha} \right)^{-1} \left( \sum_{n=2}^{\infty} D_{\varepsilon n} \varepsilon^n \right). \quad (\text{B7})$$

Therefore, the coefficient  $\mathcal{U}_{\varepsilon n}$  are given analytically.

We define  $\mathcal{S}_0 \equiv 1$ , so that  $\mathcal{R}_0$  is the zeroth-order approximation of  $\mathfrak{R}[\mathfrak{R} - A(1+q)]$  with respect to  $\varepsilon$ . When  $q \ll 1$ , the simplest solution to Equation (32) for  $\tilde{X}_1$  is

$$\tilde{X}_1 \simeq \left( \frac{q}{2+A(1+q)} \right)^{1/3} = \left( \frac{q}{2+\varpi(1-\varepsilon)^3} \right)^{1/3}. \quad (\text{B8})$$

Substitute  $\tilde{X}_1$  into Equation (31), we obtain  $\mathcal{R}_0$ :

$$\mathcal{R}_0 \simeq \left[ 2 + \left( 1 - \left( \frac{q}{2+\varpi} \right)^{1/3} \right)^{-3} \right] \left[ 2 + \varpi + \left( 1 - \left( \frac{q}{2+\varpi} \right)^{1/3} \right)^{-3} \right]. \quad (\text{B9})$$

Here, dimensionless  $\varpi$  is

$$\varpi = C_L^{-3} \left( \frac{R_{\text{WD}} \Omega_1}{c} \right)^2 \left( \frac{GM_{\text{IMBH}}}{c^2 R_{\text{WD}}} \right)^{-1} \simeq \frac{5}{4896} \frac{q}{C_L^3} \frac{M_{\text{WD}}^{4/3}}{M_{\odot} M_{\text{Ch}}^{1/3}} \left( \frac{\chi_1}{\tilde{\gamma}} \right)^2, \quad (\text{B10})$$

where  $\tilde{\gamma}$  the difference between the WD's moment of inertia and that of a uniform-density sphere. It can be related to  $\mathcal{S}_1$ :

$$|\mathcal{S}_1| := \frac{GM_{\text{WD}}^2}{c} \chi_1 := \frac{2}{5} \tilde{\gamma} M_{\text{WD}} R_{\text{WD}}^2 \Omega_1. \quad (\text{B11})$$

With  $\mathcal{R}_0$  in Equation (B9), we can calculate  $S_m$  from Equation (B2). Taking the first-order expand of  $S_m$  about  $\varpi$  gives a simple expression:

$$\mathcal{S}_0 \simeq 1, \quad \mathcal{S}_1 \simeq \frac{3}{4} \varpi Q, \quad \mathcal{S}_2 \simeq -\frac{3}{4} \varpi Q, \quad \mathcal{S}_3 \simeq \frac{1}{4} \varpi Q, \quad \mathcal{S}_4 \simeq O(\varpi^2),$$

where

$$Q = \frac{4 - 10 \times 2^{2/3} q^{1/3} + 12 \times 2^{1/3} q^{2/3} - 8q + 2^{2/3} q^{4/3}}{6 - 9 \times 2^{2/3} q^{1/3} + 12 \times 2^{1/3} q^{2/3} - 8q + 2^{2/3} q^{4/3}} \simeq \frac{2}{3}.$$

Thus,  $S_m$  are entirely influenced by the spin of the WD.

Next, we only need to calculate the  $\sum_{n=1}^{\infty} D_{\varepsilon n} \varepsilon^n$ . Since  $\lambda$  is given by Equation (21), we have

$$\lambda = \left( \frac{Gm_2}{D} C_L \right)^{-1} \left\{ \frac{Gm_1}{R_{\text{WD}}} \left( \frac{R_{\text{WD}}}{R_{\text{WD}} - \tilde{Z}} - 1 \right) - \frac{1}{2} \Omega_1^2 (2R_{\text{WD}} - \tilde{Z}) \tilde{Z} + \frac{Gm_2}{D} \left[ \frac{\tilde{Z}}{D} + \frac{D}{D - R_{\text{WD}} + \tilde{Z}} - \frac{D}{D - R_{\text{WD}}} \right] \right\}. \quad (\text{B12})$$

where  $\tilde{Z} = R_{\text{WD}} - C_L D = R_{\text{WD}} \varepsilon$ . Thus,  $\lambda$  can be expressed as

$$\lambda = \sum_{n=1}^{\infty} D_{\varepsilon n} \varepsilon^n = \frac{q}{C_L} \varepsilon - \frac{\varpi C_L}{2} (2-\varepsilon)(1-\varepsilon)\varepsilon + \frac{\varepsilon}{1-\varepsilon} \left[ 1 - \frac{1-\varepsilon}{(1-\varepsilon-C_L)(1-C_L)} \right]. \quad (\text{B13})$$

Therefore,  $D_{\varepsilon n}$  is given by

$$D_{\varepsilon n} = 1 - \frac{1}{(1-C_L)^{n+1}} + \frac{q}{C_L^2} \delta_{n1} - \frac{\varpi C_L}{2} (2\delta_{n1} - 3\delta_{n2} + \delta_{n3}). \quad (\text{B14})$$

## APPENDIX C: TRANSFERRED MASS FOR EVERY ORBITAL PERIOD

Following Appendix B, we adopt a simplified form for  $\dot{m}_1$ :

$$\dot{m}_1 := C_{\dot{m}_1} \sum_{n=0}^{\infty} C_{\varepsilon n} \varepsilon^n, \quad (\text{C1})$$

where  $C_{\dot{m}_1}$  and  $C_{\varepsilon n}$  are defined as

$$C_{\dot{m}_1} = -2\pi W(K, \Gamma) \cdot (GM_{\text{IMBH}})^2 C_L^3 / \sqrt{\mathcal{R}_0}, \quad (\text{C2a})$$

$$\sum_{n=0}^{\infty} C_{\varepsilon n} \varepsilon^n = \left( \sum_{m=0}^{\infty} S_m \varepsilon^m \right) \left( \sum_{n=0}^{\infty} \mathcal{U}_{\varepsilon n} \varepsilon^n \right). \quad (\text{C2b})$$

We can express the integral of  $\dot{m}_1$  for a Keplerian elliptical orbit

$$\int_{-\pi}^{\pi} \dot{m}_1 f_N^{-1} df = C_{\dot{m}_1} \sqrt{\frac{p^3}{Gm}} \sum_{n=0}^{\infty} C_{\varepsilon n} \int_{-f_0}^{f_0} \frac{\varepsilon^n df}{(1+e \cos f)^2}. \quad (\text{C3})$$

Here,  $\varepsilon^n$  can be rewritten as a function of the angle  $f$ :

$$\varepsilon^n = \left( 1 - \frac{p C_L}{R_{\text{WD}}} \frac{1}{1+e \cos f} \right)^n = \sum_{m=0}^n \binom{n}{m} \left( -\frac{p C_L}{R_{\text{WD}}} \right)^m \frac{1}{(1+e \cos f)^m}. \quad (\text{C4})$$

Therefore,  $\delta M_{\text{WD}}$  can be written as

$$\delta M_{\text{WD}} = C_{\dot{m}_1} \sqrt{\frac{p^3}{Gm}} \sum_{n=0}^{\infty} C_{\varepsilon n} \times \quad (\text{C5})$$

$$\left[ \sum_{m=0}^n \binom{n}{m} \left( -\frac{p C_L}{R_{\text{WD}}} \right)^m \int_{-f_0}^{f_0} \frac{df}{(1+e \cos f)^{m+2}} \right].$$

The integration result is the Appell Hypergeometric Function  $\text{AF1}(\alpha; \beta, \beta'; \gamma; x, y)$  of two variables, with a series definition (Olver et al. 2010):

$$\text{AF1}(\alpha; \beta, \beta'; \gamma; x, y) = \sum_{m=0}^{\infty} \sum_{n=0}^{\infty} \frac{(\alpha)_{m+n} (\beta)_{m+n} (\beta')_{m+n}}{(\gamma)_{m+n} m! n!} x^m y^n, \quad (\text{C6})$$

where  $(q)_n$  denotes the Pochhammer symbol. The integral evaluates to

$$\int_{-f_0}^{f_0} \frac{df}{(1+e \cos f)^{m+2}} = \frac{4}{(1+e)^{m+2}} \sin\left(\frac{f_0}{2}\right) \times \quad (C7)$$

$$\text{AF1} \left[ \frac{1}{2}; \frac{1}{2}, m+2; \frac{3}{2}; \sin^2\left(\frac{f_0}{2}\right), \frac{2e}{1+e} \sin^2\left(\frac{f_0}{2}\right) \right].$$

Thus, we require the value of  $\sin(f_0/2)$ . Since we substitute  $D$  with  $p/(1+e \cos f)$ ,  $f_0$  satisfies  $R_{\text{WD}} = C_{\text{L}} D(f_0)$ . To relate  $p$  and  $R_{\text{WD}}$ , we use  $\epsilon$  as defined in Section 5.1.1:

$$r_{\text{p}} = \frac{p}{1+e} := (1-\epsilon) \frac{R_{\text{WD}}}{C_{\text{L}}}. \quad (C8)$$

Therefore,  $f_0$  and  $\sin(f_0/2)$  can be written as

$$f_0 = \sin^{-1} \left[ \sqrt{1 - \left(1 - \frac{1+e}{e} \epsilon\right)^2} \right], \quad (C9)$$

$$\sin\left(\frac{f_0}{2}\right) = \sin \left\{ \frac{1}{2} \sin^{-1} \left[ \sqrt{1 - \left(1 - \frac{1+e}{e} \epsilon\right)^2} \right] \right\} \equiv \sqrt{\frac{1+e}{2e} \epsilon}.$$

Substituting  $\sin(f_0/2)$  into Equation (C7) yields Equation (54).

In Schwarzschild spacetime,  $dt/d\psi$  can be used to substitute  $\dot{t}_{\text{N}}^{-1}$  (Cutler et al. 1994; Martel 2004). The primary geodesic equation is:

$$\frac{dt}{d\psi} = \frac{Gm}{c^3} \frac{\hat{p}^{3/2}}{\hat{x}^2} \frac{\hat{p}\sqrt{\hat{p}-4}}{(\hat{p}-2\hat{x})\sqrt{\hat{p}-4}-2\hat{x}} \sqrt{1 + \frac{4(1-e^2)}{\hat{p}(\hat{p}-4)}}, \quad (C10)$$

where  $\hat{p} := p/(Gm/c^2)$  and  $\hat{x} := 1+e \cos \psi$  are dimensionless quantities. The pericenter  $r_{\text{p}}$ , apocenter  $r_{\text{a}}$ , eccentricity  $e$  are defined as:

$$r_{\text{p}} = \frac{Gm}{c^2} \frac{\hat{p}}{1+e}, \quad r_{\text{a}} = \frac{Gm}{c^2} \frac{\hat{p}}{1-e}, \quad e = \frac{r_{\text{a}} - r_{\text{p}}}{r_{\text{a}} + r_{\text{p}}}. \quad (C11)$$

Equation (C8) remains valid. The integral variable in Equation (C3) is changed from  $f$  to  $\psi$ , with  $\psi_0$  satisfying Equation (C9). For  $\hat{x} \rightarrow 0$ , a Taylor expansion of Equation (C10) is:

$$\frac{\hat{p}\sqrt{\hat{p}-4}}{(\hat{p}-2\hat{x})\sqrt{\hat{p}-4}-2\hat{x}} := \sum_{k=0}^{\infty} F_k(\hat{p}) \hat{x}^k, \quad \text{where } F_0 = 1. \quad (C12)$$

Equation (C5) then becomes

$$\delta M_{\text{WD}} = \sum_{k=0}^{\infty} \left[ F_k(\hat{p}) C_{m_1} \frac{Gm}{c^3} \hat{p} \sqrt{\frac{(\hat{p}-2)^2 - 4e^2}{\hat{p}-4}} \times \quad (C13)$$

$$\sum_{n=0}^{\infty} C_{\epsilon n} \sum_{m=0}^n \binom{n}{m} \left( -\frac{Gm}{c^2} \frac{\hat{p} C_{\text{L}}}{R_{\text{WD}}} \right)^m \int_{-\psi_0}^{\psi_0} \frac{d\psi}{\hat{x}^{(m-k)+2}} \right].$$

We continue using Equation (C7) for the integral, so Equation (C13) reduces to Equation (65).

#### APPENDIX D: EQUIVALENCE OF PHASE AND PERIOD EVOLUTION IN THE ADIABATIC APPROXIMATION

As described in Section 6, our goal is to detect the phase shift  $\Delta u$  between systems with and without MT over an observation period  $t_{\text{obs}}$ . However, a precise calculation of orbital phase is not required; we only need to estimate the period of each cycle to address the problem under investigation.

We use the calculation result of elliptical orbit. To compute  $\Delta u$ , we express the true anomaly  $f(t)$  as a function of the eccentric anomaly  $u$ , which satisfies  $r = a(1 - e \cos u)$ , and Kepler's equation

$2\pi(t - t_{\text{p}})/T = u - e \sin u$ , where  $t_{\text{p}} \leq t$  is the time of the last pericenter passage. The GW waveform  $h(f(t))$ , described by true anomaly  $f$ , can be written as the function of  $u$  by transforming  $f$  to  $u$ . Therefore, calculating the phase difference  $\Delta f(t)$  is equivalent to calculating  $\Delta u(t)$ . The relationship between  $u$  and  $t$  is given by the Bessel function of the first kind  $J_n(x)$  (Murray & Dermott 1999):

$$u(t, N) \simeq 2\pi(N-1) + l_{\text{N}} + \mathcal{J}(l_{\text{N}}, e_{\text{N}}), \quad (D1)$$

where

$$l_{\text{N}} := 2\pi \left( t - t_{\text{pN-1}} \right) / T_{\text{N}}, \quad t_{\text{pN-1}} := \sum_{k=1}^{N-1} T_{\text{k}}, \quad (D2)$$

$$\mathcal{J}(l_{\text{N}}, e_{\text{N}}) := \sum_{n=1}^{\infty} \frac{2}{n} J_n(ne_{\text{N}}) \sin nl_{\text{N}}. \quad (D3)$$

Here,  $e_{\text{N}}, T_{\text{N}}$  represent the eccentricity and period of the N-th cycle. Assuming the  $e_{\text{k}}, T_{\text{k}}$  are approximately constant within the k-th cycle. The Bessel functions show the difference between elliptical and circular orbits.

However, the phase difference  $\Delta u(t)$  is not increase monotonically according to the Bessel function. It suddenly increases near pericenter and decreases slowly near apocenter, but  $u(t_{\text{pN}}) - u(t_{\text{pN-1}}) = 2\pi$ . This does not capture the overall effect of the phase change. When  $[u(t, N) - u(t_{\text{pN}}, N)] / u(t_{\text{pN}}, N) \ll 1$ , we disregard the series of Bessel functions, yielding:

$$\frac{u(t, N)}{2\pi} \simeq N - 1 + \left( t - t_{\text{pN-1}} \right) / T_{\text{N}}. \quad (D4)$$

The phase difference with and without the MT process is

$$\frac{\Delta u}{2\pi} \simeq t \left( \frac{1}{T_{\text{N}}} - \frac{1}{T_{\text{N}}^*} \right) - \left( \frac{t_{\text{pN-1}}}{T_{\text{N}}} - \frac{t_{\text{pN-1}}^*}{T_{\text{N}}^*} \right) < 0, \quad (D5)$$

where the superscript asterisk indicates that MT process is not considered. Due to the  $\langle \dot{t}_{\text{MT}}^{\mathcal{B}} \rangle_{\text{sec}}$  in Equation (57),  $T_{\text{N}} \geq T_{\text{N}}^*$  and  $t_{\text{pN}} \geq t_{\text{pN}}^*$  always holds.

Therefore, the inequality and equation about the phase difference  $\Delta u_{\text{g}} < 0$  and required time  $t_{\text{g}}$  for our goal (i.e.  $\Delta u(t_{\text{g}}) = \Delta u_{\text{g}}$ ) are

$$\frac{t_{\text{pN-1}} - t_{\text{pN-1}}^*}{T_{\text{N}}^*} \leq \frac{|\Delta u_{\text{g}}|}{2\pi} \leq \frac{t_{\text{pN}} - t_{\text{pN}}^*}{T_{\text{N}+1}^*}, \quad (D6a)$$

$$t_{\text{g}} \left( \frac{1}{T_{\text{N}}} - \frac{1}{T_{\text{N}}^*} \right) - \left( \frac{t_{\text{pN-1}}}{T_{\text{N}}} - \frac{t_{\text{pN-1}}^*}{T_{\text{N}}^*} \right) = -\frac{|\Delta u_{\text{g}}|}{2\pi}. \quad (D6b)$$

For the orbits discussed in Section 5.2, Inequality (D6a) yields a unique integer value for N. Substituting this into Equation (D6b) gives the required time  $t_{\text{g}}$ . For  $N \gg 1$ ,  $t_{\text{g}} \simeq t_{\text{pN-1}} \simeq t_{\text{pN-1}}^*$ . This is the equivalence of phase and periodic changes that we want.

In order to better clarify the meaning of Equation (D6), we define  $T_{\text{k}}^* := T_{\text{k}}(1 - \varsigma_{\text{k}}) < T_{\text{k}}$  and  $t_{\text{pN-1}} \leq t_{\text{g}} := (1 + \lambda_{\text{g}})t_{\text{pN-1}} \leq t_{\text{pN}}$ . Here,  $\lambda_{\text{g}}$  represents the difference between  $t_{\text{pN-1}}$  and  $t_{\text{g}}$ . From Equation (D6b) and the condition  $t_{\text{pN-1}} \leq t_{\text{g}} \leq t_{\text{pN}}$ , we obtain an inequality for  $\lambda_{\text{g}}$ :

$$0 \leq \lambda_{\text{g}} = \left( \frac{|\Delta u_{\text{g}}|}{2\pi} \frac{1 - \varsigma_{\text{N}}}{\varsigma_{\text{N}}} - \frac{\sum_{k=1}^{N-1} T_{\text{k}} \varsigma_{\text{k}}}{T_{\text{N}} \varsigma_{\text{N}}} \right) \frac{T_{\text{N}}}{t_{\text{pN-1}}} < \frac{T_{\text{N}}}{t_{\text{pN-1}}}. \quad (D7)$$

From Inequality (D7), a unique integer N can be determined, which corresponds to the closest value satisfying  $\sum_{k=1}^{N-1} T_{\text{k}} \varsigma_{\text{k}} / [T_{\text{N}}(1 - \varsigma_{\text{N}})] \simeq |\Delta u_{\text{g}}| / 2\pi$ . If  $T_{\text{N}} \ll t_{\text{pN-1}}$ , the factor  $\lambda_{\text{g}}$  can be neglected, and  $t_{\text{g}}$  can be replaced with  $t_{\text{pN-1}}$  for the calculation. Solving for N then reduces to finding the unique value of N in Inequality (59).

This paper has been typeset from a  $\text{\TeX}/\text{\LaTeX}$  file prepared by the author.